NORTHWESTERN UNIVERSITY

Transition-Edge Sensors for X-Ray Science Applications

A DISSERTATION

SUBMITTED TO THE GRADUATE SCHOOL

IN PARTIAL FULFILLMENT OF THE REQUIREMENTS

for the degree

DOCTOR OF PHILOSOPHY

Field of Applied Physics

By

Daikang Yan

EVANSTON, ILLINOIS

June 2019

ABSTRACT

Transition-Edge Sensors for X-Ray Science Applications

Daikang Yan

This thesis focuses on the development of the transition-edge sensor (TES) for various X-ray science applications, especially for synchrotron beamline experiments. The ultimate aim is to build a detector that has a higher energy resolution than semiconductor detectors, and a higher operation speed than crystal spectrometers.

The possible applications include X-ray spectroscopy, Compton profile measurement and energy-dispersive X-ray diffraction. The latter two are discussed in detail, and we designed a prototype TES to meet the requirements of these applications.

In order to better address the nonlinear signal response function of the TES and therefore improve the energy resolution of the TES, we studied the temperature and current dependence of the TES resistance. It is found that adding normal metal bars on the TES superconducting film will change not only the current flow pattern, but also the resistance dependence on temperature and current, at the low bias state. We also studied X-ray absorber materials, and found that bismuth is a good absorber material, and should be fabricated using electrodeposition methods so that the grain size is large

enough that there is no energy loss during the photon energy down-conversion process, so that there is no undesired low-energy tail.

In order to improve the operation speed, we adopted a frequency-division multiplexing scheme with microwave resonators and superconducting quantum interference devices (SQUIDs). This thesis has shown how to set up the experiment stage, and showed how to characterize the noise and signal response of the multiplexing electronics. The TESs have been characterized under this multiplexing readout scheme, and have demonstrated an energy resolution better than silicon detectors.

Acknowledgements

It has been a great pleasure to have Prof. Chris Jacobsen as my primary advisor. He offers me the opportunity of exploring X-ray science, which has been my area of interest. He is a very supportive professor, willing to hear from students, and has given me enormous help and suggestions. When started the graduate school, I felt like an illiterate in scientific research. Chris has shown great patience in my learning path.

I am grateful working under Dr. Antonino Miceli's supervision at the Advanced Photon Source (APS) at Argonne National Lab, where my thesis work was primarily conducted. Without him I would never have the chance to study the low-temperature detector, which is interesting and exciting. He is a very easy-going advisor, and has given me enough flexibility. My research life could be a lot tougher if were not at his lab.

I appreciate the time working with Tom Cecil, who is now working in the High Energy Physics Department at Argonne, and Tim Madden, who developed the first ROACH system for our device readout and now is working on the APS upgrade. I am also thankful working with Lisa Gades, Umesh Patel, Orlando Quaranta, and Tejas Guruswamy in our group. Lisa, Umesh, and Orlando have fabricated some of the TESs and absorbers used in this study, and offered me lots of suggestions on being a better researcher. I enjoyed discussing questions with Orlando going into great details, as well as chatting over other interesting topics. During my last year, I have asked lots of advices from Tejas, and he is always willing to share his experience. I feel very lucky having met all our group members.

These years as a graduate student are a treasure to cherish because of the memory with all of you.

I thank my parents' support over these years. My father never hesitates supporting any of my dreams, from spending the last of his two dollars buying me a bubblegum when I was five, to encouraging me chasing a career in science when I graduated from college. My mother has put lots of efforts in my early education. And although reluctant to see her daughter going far abroad, she respected and supported my decision. Without their backup, I would not have the opportunity doing exciting research.

I would also like to thank my boyfriend Xinhua Sun, who did not hesitate to wait for me when distance set us apart, and never stopped being a great life companion over these years. Maintaining a remote relationship requires more than love, and you have all the good character it needs. Your company has helped me went through dark times.

Table of Contents

List of Tables

List of Figures

CHAPTER 1

Introduction

1.1. X-ray spectroscopy

Our understanding of the physical world relies on the development of scientific tools. With proper X-ray detectors, our eyesight is extended from the visible light regime to very short wavelengths, so we can "observe" phenomena down to the atomic level.

Atoms consists of a nucleus and one or several bound electrons that stay in discrete energy levels. When a photon hits an atom, an electron that has a binding energy equal to or smaller than the photon can absorb its energy and become a free electron, leaving a vacancy in its original level. An electron at a higher energy level can then transit into this vacancy. The energy emission during this process sometimes takes the form of a photon. The energy structures of different elements are unique, and can be influenced by the chemical state, so photon absorption and emission measurements can be used to determine the chemical constitution of a material. The energy change involved in such process falls between 100 eV $\sim$ 100 keV, which is the X-ray regime. To acquire such information, X-ray detectors are needed.

Figure 1.1a shows the X-ray emission spectra of several sulfur compounds' $K\alpha_1$ and $K\alpha_2$ lines [**1**]. It can be seen that sulfur with different valances has different emission energy peaks. A detector with 1 eV energy resolution will be able to distinguish between

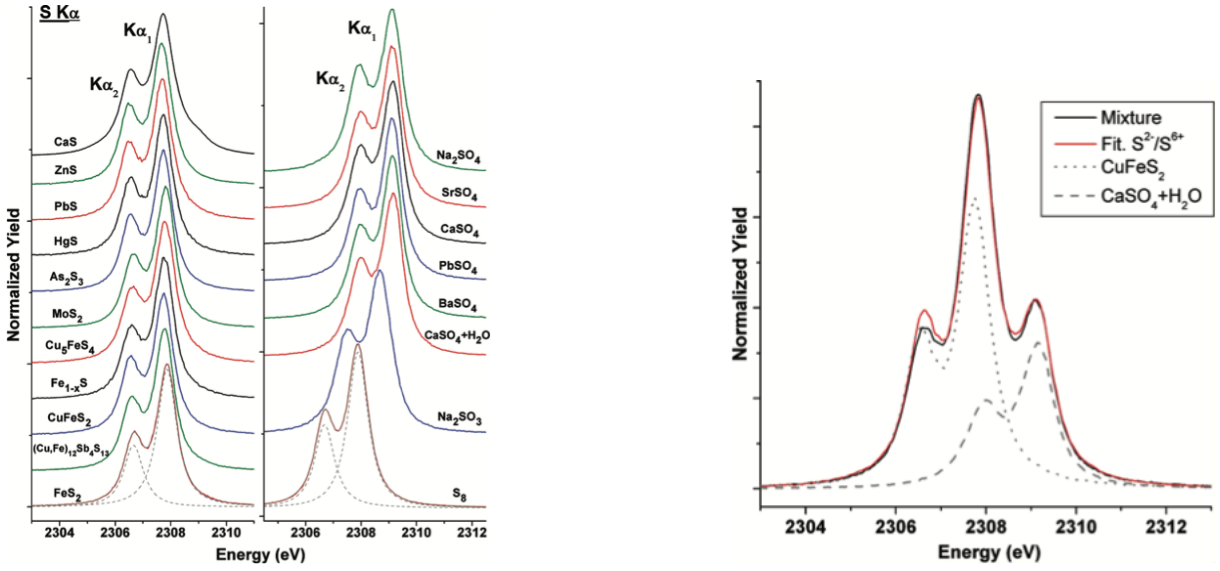

(a) (b)

Figure 1.1. (a)This X-ray emission spectrum shows $K\alpha_1$ and $K\alpha_2$ fluorescence lines from several sulfur compounds. X-ray emission energies shift by $\sim$ 1 eV due to the chemical bond of the S atoms. (b)The spectra of the mixture of $CuFeS_2$ and $CaSO_4 + H_2O$. These figures are from Figure 4 and 8 in [**1**].

several sulfides such as $CuFeS_2$ and $CaSO_4 + H_2O$. Given a mixture of these two compounds with a spectrum as shown in Figure 1.1b, the ratio of each component can be determined by fitting to reference spectra. Besides distinguishing component materials, the fine energy resolution spectra can tell us additional information. The CaS spectrum in Figure 1.1a shows an extra shoulder at 2309 eV while the spectral shapes of other compounds are similar. This indicates a change in sulfur oxidation state that is caused by X-ray radiation damage. Generally, X-ray emission lines shift by a few eV due to the core-level electrons' energy state change at different valances. In order to resolve such features, the detector's resolution should be $\sim$ 1 eV.

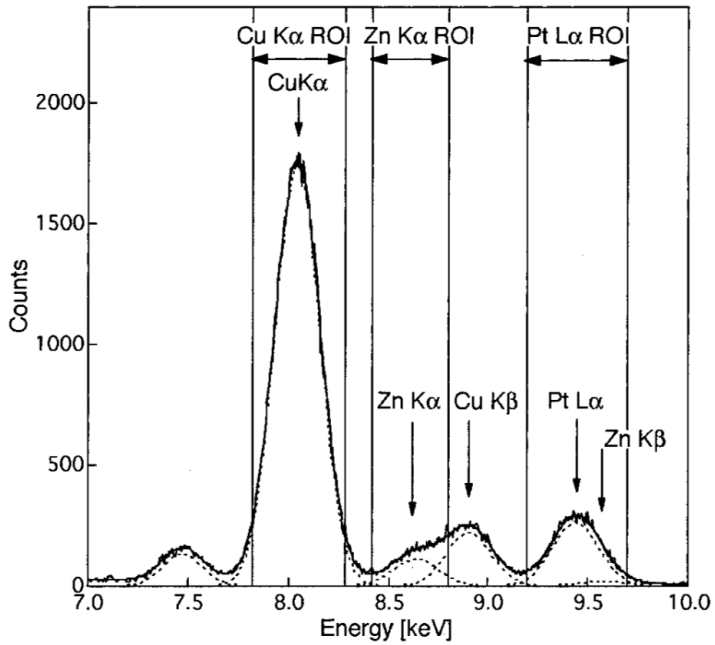

Figure 1.2. The X-ray fluorescence spectrum from a cancer cell measured by a germanium detector (ROI = region of interest). This figure is from Figure 2 in [**2**].

In addition to chemical shift information, having a good energy resolution is helpful in distinguishing adjacent emission lines. Figure 1.2 shows the X-ray emission spectrum from a cancer cell measured by an energy-dispersive germanium detector [**2**]. With the detector's energy resolution of hundreds of electronvolts, the Cu $K\alpha$ in this mixture can be recognized. However, the Cu $K\beta$, Zn $K\alpha$, Zn $K\beta$ and Pt $L\alpha$ lines are not distinguishable, and they can only be resolved if the detector's resolution is below 100 eV. Emission spectra similar to this example are shown in Figure 7.16. The TES made in our lab was able to distinguish some emission peaks that cannot be resolved by a silicon detector as will be shown in Section 7.6.

There are other X-ray techniques that require an energy-resolving detector with good resolution. Compton scattering, for example, is used to obtain the electron momentum distribution in a material. It uses monochromatic hard X-ray beam with known energy to interact with the sample, and measures the outcome angle and energy of the scattered photon, from which the momentum of the interacting electrons can be calculated. To achieve an electron momentum resolution of 1 a.u. (atomic unit), the detector resolution should be below 80 eV [**3**]. In another example, *energy-dispersive X-ray diffraction (EDXRD)* also needs detectors with energy resolution. As traditional X-ray diffraction uses a monochromatic light source and therefore requires that one rotates the sample to get the information from different diffraction crystal orientations, EDXRD uses polychromatic light, and takes the measurement at one shot. X-ray absorption spectroscopy is another core level X-ray technique. Having a high energy resolution detector to measure the fluorescence yield at the same time can greatly improve the analysis of an absorption spectrum [**4, 5**].

1.2. Spectrometers

For energy-resolving X-ray measurements, there are two types of X-ray detectors: *wavelength-dispersive spectrometers (WDS)*, and *energy-dispersive spectrometers (EDS)*. The experiment shown in Figure 1.1 was conducted with a WDS with Si crystal (111) face, and achieved an experimental energy resolution of 0.44 eV.

Wavelength-dispersive spectrometers rely on the photon's "wave" nature. The photon wavelength λ is calculated with Bragg's law $\lambda = 2d \sin\theta$, given the diffraction crystal's reflection angle θ and the lattice spacing d. The energy resolution of a WDS is limited

by the Darwin width of the reflective crystal, which is set by the number of crystal layers that contribute to the net crystal reflectivity. The achievable energy resolution is usually better than 1 eV [**6**]. This makes the WDS a commonly used detector for experiments that need high energy resolution.

Despite the high energy resolution, several shortcomings limit the popularity of WDS detectors. First, in order to have a single incident angle θ, one needs collecting optics between the sample and the Bragg crystal which limits the angle of acceptance. Second, the achievable Bragg angle θ is limited to $0 < \theta < \pi/2$. To cover a larger wavelength span, different crystal lattice spacings are needed. So a wide energy span will need a set of different crystals. Most importantly, the mechanism of the WDS requires a mechanical rotation of the the crystal for energy scanning. This becomes very time consuming especially for large energy span measurements.

An alternative to WDS is the *energy-dispersive spectrometer (EDS)*, for which the incident photon is absorbed and its energy is measured. Most EDSs use semiconductor sensors. The incident photon energy is measured by counting the number of photon-induced electron-hole (e-h) pairs. Unlike a WDS, an EDS can detect a broad range of photon energies simultaneously, so the EDS can operate faster than the WDS. However, it does not have comparable energy resolution.

For a silicon detector [**7**], the average energy required for creating an e-h pair is $\varepsilon = 3.6$ eV. A photon of $E = 6$ keV will therefore create $N = E/\varepsilon \approx 1667$ e-h pairs. The Poisson fluctuation is $\sqrt{N}$. Taking into account the Fano factor [**8**] ($F = 0.115$ for Si [**9**]), which comes from the Poisson fluctuation of large numbers of phonons, the final energy resolution is $\Delta E = 2.35\varepsilon\sqrt{FN} \approx 117$ eV. This resolution is sufficient for certain applications, but

insufficient for chemical shift detection as mentioned above. Furthermore, semiconductive EDSs are insufficient to discriminate between K-shell fluoresence lines of low-Z elements and L-shell lines of medium-Z elements below 2 keV. Besides, silicon detectors usually have charge loss problems, causing low energy tails in the measured spectra [**10**]. In dilute ingredient detection, the target energy peaks may be buried under the background noise or adjacent strong peaks. Therefore, there is a need for energy dispersive detectors with better energy resolution than the semiconductor detectors, which are addressed in the next section.

1.3. Low-temperature detectors

While WDS and semiconductor EDS show the advantages and disadvantages described above, there are a few types of low-temperature superconducting detectors that can be used as EDSs. Superconducting materials have electromagnetic features that change radically at the finite transition temperature of the onset of superconductivity due to the forming and decoupling of Cooper-pairs. Based on this phenomenon, they can be used to measure photon energy. Since the energy-gap for Cooper-pair generation is almost 1/1000 of that of photo-electrons in semiconductors, the theoretical statistical noise of the superconducting detectors can be $\sim$ 30 times smaller. Briefly introduced below are the commonly studied superconducting detectors, including the subject of this thesis – the transition-edge sensor (TES).

The *Superconducting Tunnel Junction (STJ)* consists of two superconducting layers separated by an insulating layer, operating below the critical tempearature T_c. The quasi-particles created by a photon event can tunnel across the insulating barrier and

their number will be measured to calculate the photon energy. For this type of device, a resolution of 12 eV at 5.9 keV has been achieved [**11**]. However, it is challenging to multiplex STJs to large numbers.

Microwave Kinetic Inductance Detectors (MKIDs) measure photon energy through kinetic inductance changes. A MKID pixel is formed by a unique superconducting inductor and a coupling capacitor, giving this LC circuit a certain resonant frequency. Pixels of different resonant frequencies can be coupled through a microwave feedline, and their signals can be read out at the same time at different frequency tones. This easy-multiplexing feature gives MKIDs the potential for a large collection area and fast readout speed. Prior work on MKIDs has demonstrated an energy resolution of about 50 eV at 5.9 keV [**12**], whereas earlier in this chapter it was argued that an energy resolution of ~ 1 eV is desirable for observing chemical shifts in X-ray emission lines from materials.

Another approach called *Metallic Magnetic Calorimeter (MMC)* uses a metallic paramagnetic sensor to transduce the photon energy into a magnetic flux change, which is in turn detected using a *Superconducting QUantum Interference Device (SQUID)*. MMC detectors can have large dynamic range and near 100% quantum efficiency [**13**]. To date, an energy resolution of 1.58 eV at 5.9 keV has been achieved [**13**], and the multiplexing of this type of device is under development [**14**].

In this thesis, the *Transition-Edge Sensor (TES)* is studied. It utilizes the sharp resistance-temperature dependence of a superconducting material, and works as a thermistor to measure the heat generated by a photon. This operation principle is introduced in Chapter 2. The energy resolutions of TESs have reached 0.9 eV at 1.58 keV [**15**], 1.58 eV at 5.9 keV [**16**], and 22 eV at 97 keV [**17**]. Given this resolution in the hard

X-ray regime, as mentioned in Section 1.1, the TES can be used in Compton scattering and EDXRD experiments, which is studied in detail in Section 3.1. In order to better understand the signal response of the TES so that its energy resolution can be further improved, in Section 3.2 we study the resistance transition shape of TESs with different geometric layouts. For high-energy, high-quantum-efficiency applications, separate photon absorbers are used. This is discussed in Chapter 4. Similar to other low-temperature detectors, improving the collecting efficiency of the TES usually requires multiplexing readout, and this is discussed in Chapter 5. Chapter 6 discusses the experimental setup and characterization of the multiplexing electronics. Chapter 7 shows the characterization of our TES detector, and Chapter 8 shows the X-ray signal processing methods used in our study.

CHAPTER 2

Transition-edge sensors (TES)

In superconductors, in the ground state, electrons exist in the form of Cooper pairs due to electron-phonon interaction, with displacements of atomic nuclei from their crystal lattice positions. These Cooper pairs move with zero resistance. Energy inputs such as thermal excitations can break Cooper pairs and increase the resistance of the material. Based on this mechanism, superconducting materials can be made into calorimeters as shown in Figure 2.1.

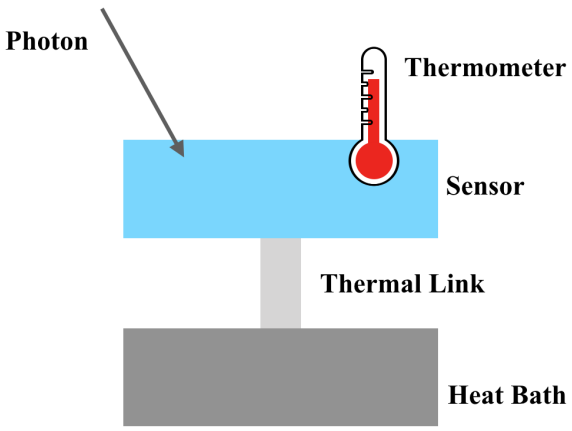

Figure 2.1. A calorimeter measures the temperature change when a photon or other energetic particle hits the sensor. The thermal energy is then drained through a weak thermal link to the heat bath at a constant temperature after which the system returns to the equilibrium state.

Figure 2.2 shows the sharp resistance-temperature dependence of an iridium superconducting film. When properly biased at the superconducting-to-normal transition temperature, it can measure temperature changes up to $\sim$ 1 mK. Such a device is called a "transition-edge sensor (TES)". When a photon hits the TES, it causes a temperature rise in the sensor and therefore the resistance undergoes a sharp change, which can be read out in an electrical circuit. For applications that require the absorption of high energy photons, the sensor is usually connected with an extra absorber. This chapter introduces the operation circuit for a single TES, and the property of TES absorbers will be discussed in Chapters 3 and 4.

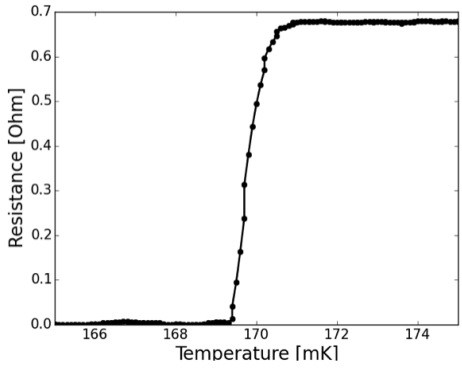

Figure 2.2. The resistance-temperature dependence measured from an iridium (Ir) superconducting film. The transition width of this film is $\sim$ 1 mK.

2.1. Bias circuit for simple TES

Figure 2.2 shows that for large energy input, the resistance change of a TES is nonlinear. A simulation approach for the TES nonlinear transition shape is discussed in Section 3.2. However, in the small signal limit, the TES response can be treated linearly. Denoting the TES resistance as R, its values depends on both current I and temperature

T. Its transition sensitivity can be defined by two unitless coefficients

$$\alpha_I \equiv \frac{\partial \log R}{\partial \log T}|_{(I_0,T_0)} = \frac{T_0}{R_0}\frac{\partial R}{\partial T}|_{(I_0,T_0)}, \tag{2.1}$$

$$\beta_I \equiv \frac{\partial \log R}{\partial \log I}|_{(I_0,T_0)} = \frac{I_0}{R_0}\frac{\partial R}{\partial I}|_{(I_0,T_0)}. \tag{2.2}$$

Here, the subscript I is used to indicate that the TES is voltage-biased so that the output signal is current. For voltage output configurations, usually the subscript is V is used [**18**]. The subscript 0 denotes values at the initial state. Defining the variation of the bias voltage, the TES current, the TES temperature, and the signal input power as

$$\delta V \equiv V - V_0, \qquad \delta I \equiv I - I_0, \qquad \delta T \equiv T - T_0, \qquad \text{and } \delta P \equiv P - P_0, \tag{2.3}$$

respectively, the TES resistance can be approximated as

$$R \approx R_0 + \frac{\partial R}{\partial T}|_{(I_0,T_0)}\delta T + \frac{\partial R}{\partial I}|_{(I_0,T_0)}\delta I = R_0 + \alpha_I \frac{R_0}{T_0}\delta T + \beta_I \frac{R_0}{I_0}\delta I. \tag{2.4}$$

The TES is thermally biased by a heat sink in order to stay at the critical temperature, and is electrically biased in order to turn the termperature change into an electric signal. Its signal response can be described by electro-thermal differential equaitons [**19**], and can be solved analytically in the linear small signal limit.

2.1.1. Electrical bias

Figure 2.3a and 2.3b show the electrical bias and the Thevenin-equivalent circuit of the TES, respectively. This voltage bias configuration was first discussed by Irwin *et al.*[**20**]. In this scheme, the TES Joule heating power $P_J = V^2 R/(R+R_L)^2$ drops as the resistance

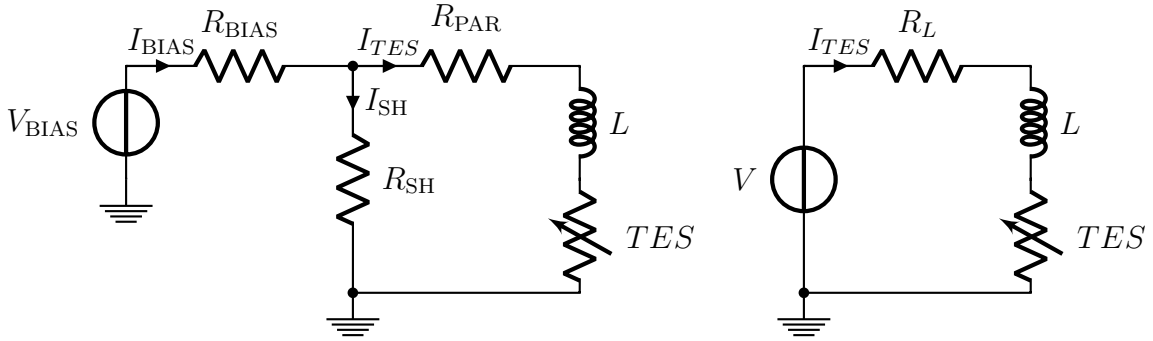

Figure 2.3. The electrical bias, and Thevenin-equivalent circuit of a TES. (a) A voltage source $V_{\rm BIAS}$ and a large resistance $R_{\rm BIAS}$ are used in the room temperature stage to provide a bias current $I_{\rm BIAS}$. The TES with its variable resistance R is connected in series with an inductance L, which includes the stray inductance from the wires, the TES-SQUID coupling inductance, and the extra inductance that tunes the TES response time. A parasitic resistance $R_{\rm PAR}$ is in series with the TES, accounting for the stray resistance from the wire bound contacts. A shunt resistance $R_{\rm SH}$ is in parallel with this branch. (b) The Thevenin-equivalent representation of the bias circuit. The bias current $I_{\rm BIAS}$ and the parallel resistance $R_{\rm SH}$ provide an equivalent voltage bias $V = I_{\rm BIAS}R_{\rm SH}$ to the TES, the inductance L, and the equivalent load resistance $R_L = R_{\rm SH} + R_{\rm PAR}$.

increases with temperature; this negtive feedback makes the device self-stablized. If the TES is current-biased, in contrast, it cannot come back to equilibrium quickly. Therefore we use the voltage-bias configuration, and measure the current signal of the TES.

The circuit in Figure 2.3 can be decribed by the electrical differential equation

$$L\frac{dI}{dt} = V - I \cdot R_L - I \cdot R(T, I). \tag{2.5}$$

Expanding this using Equation (2.3), we obtain

$$L\frac{d(I_0 + \delta I)}{dt} = (V_0 + \delta V) - (I_0 + \delta I)R_L - (I_0 + \delta I)(R_0 + \alpha_I \frac{R_0}{T_0}\delta T + \beta_I \frac{R_0}{I_0}\delta I), \tag{2.6}$$

which can be reorganized to give

$$L\frac{dI_0}{dt} + L\frac{d\delta I}{dt} = -[R_L + R_0(1+\beta_I)]\delta I - \frac{\alpha_I I_0 R_0}{T_0}\delta T + (V_0 - I_0 R_L - I_0 R_0) - (\alpha_I \frac{R_0}{T_0}\delta T \delta I + \beta_I \frac{R_0}{I_0}\delta I^2) + \delta V. \tag{2.7}$$

Because I_0 is a constant, V_0 is the equilibrium voltage, and the second-order terms become zero with small perturbations, we have

$$\frac{dI_0}{dt} = 0, \quad V_0 = I_0 R_L + I_0 R_0, \quad \delta T \delta I = 0, \text{and } \delta I^2 = 0. \tag{2.8}$$

Therefore Equation 2.7 can be rewritten as

$$L\frac{d\delta I}{dt} = -[R_L + R_0(1+\beta_I)]\delta I - \frac{\alpha_I I_0 R_0}{T_0}\delta T + \delta V. \tag{2.9}$$

We define the low-frequency loop gain under constant current as [**19**]

$$\mathcal{L}_I = \frac{P_{J_0}\alpha_I}{GT_0}, \tag{2.10}$$

where P_{J_0} is Joule heating power at the equilibrium state, and G is the thermal conductance between the TES and the heat bath.

When $\mathcal{L}_I = 0$, the current response is independent of δT, and can be characterized by an electrical decay time of

$$\tau_{el} = \frac{L}{R_L + R_0(1+\beta_I)}. \tag{2.11}$$

As a result, we can simplify Equation 2.9 to a final form as

$$\frac{d\delta I}{dt} = -\frac{1}{\tau_{el}}\delta I - \frac{\mathcal{L}_I G}{I_0 L}\delta T + \frac{1}{L}\delta V. \tag{2.12}$$

2.1.2. Thermal bias

Figure 2.4 shows the thermal bias for a simple TES. It can be described by

$$C\frac{dT}{dt} = P + P_J - P_b. \tag{2.13}$$

Here P is the external input power, P_J is the Joule heating power, and P_b is the cooling power of the heat bath. In some applications, the TES is used together with photon absorbers, which will add one or multiple thermal bodies to Figure 2.4, and there will be multiple thermal differential equations in the same form of Equation (2.13). Those are discussed in Appendix A.2. Here we discuss the simplest version of a one-body TES.

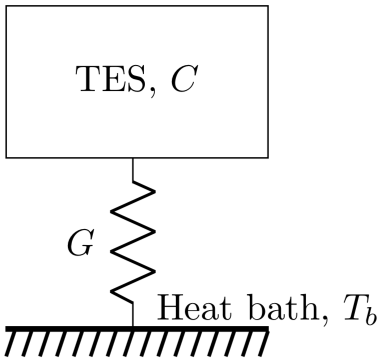

Figure 2.4. TES thermal bias. The TES has a heat capacity of C, and is cooled by the heat bath of temperature T_b. The thermal link that connects the TES to the bath has a thermal conductivity of G.

We assume a power-law dependence for the heat bath's cooling power of [**19**]

$$P_b = K(T^n - T_b^n), \tag{2.14}$$

from which the thermal conductance between the TES and the heat bath is defined as

$$G \equiv \frac{dP_b}{dT} = nKT^{n-1}. \tag{2.15}$$

The value of the exponential index n depends on the phonon transfer nature via the thermal link, and is 3–4 for electron-lattice coupling [**18**]. Within the small signal limit, we have

$$\begin{aligned} P_b &\approx P_{b_0} + \frac{dP_b}{dT}\delta T \\ &= P_{b_0} + G\delta T. \end{aligned} \tag{2.16}$$

Expanding Equation (2.13), we get

$$C\frac{d(T_0+\delta T)}{dt} = (P_0+\delta P) + (I_0+\delta I)^2(R_0 + \alpha_I\frac{R_0}{T_0}\delta T + \beta_I\frac{R_0}{I_0}\delta I) - (P_{b_0} + G\delta T), \tag{2.17}$$

which can be reorganized to give

$$C\frac{dT_0}{dt} + C\frac{d\delta T}{dt} = [I_0R_0(2+\beta_I)]\delta I + (\frac{\alpha I_0^2R_0}{T_0} - G)\delta T + \delta P + (P_0 + I_0^2R_0 - P_{b_0}) + \mathcal{O}(\delta T^2, \delta I^2). \tag{2.18}$$

Similar to condition (2.8), we have

$$\frac{dT_0}{dt} = 0, \quad P_{b_0} = P_0 + I_0^2R_0, \quad \text{and } \mathcal{O}(\delta T^2, \delta I^2) = 0, \tag{2.19}$$

because of the constant T_0, the equilibrium condition of cooling power P_{b_0}, and since the higher-order terms become zero with small signals. Therefore we can rewrite Equation 2.18

as

$$\frac{d\delta T}{dt} = \frac{I_0 R_0}{C}(2+\beta_I)\delta I + (\mathcal{L}_I - 1)\frac{G}{C}\delta T + \frac{1}{C}\delta P. \tag{2.20}$$

We then define a natural thermal time constant of

$$\tau = \frac{C}{G}, \tag{2.21}$$

which addresses purely the thermal effect, and the constant-current thermal constant of

$$\tau_I = \frac{\tau}{1-\mathcal{L}_I}, \tag{2.22}$$

that gives the temperature decay for $\delta I = 0$. As a result, we can simplify Equation (2.20) to the final form

$$\frac{d\delta T}{dt} = \frac{I_0 R_0}{C}(2+\beta_I)\delta I - \frac{1}{\tau_I}\delta T + \frac{1}{C}\delta P. \tag{2.23}$$

2.1.3. TES signal response

Now we have a set of first-order ordinary differential equations of

$$\begin{aligned}
\frac{d\delta I}{dt} &= -\frac{1}{\tau_{el}}\delta I - \frac{\mathcal{L}_I G}{I_0 L}\delta T + \frac{1}{L}\delta V, \\
\frac{d\delta T}{dt} &= \frac{I_0 R_0}{C}(2+\beta_I)\delta I - \frac{1}{\tau_I}\delta T + \frac{1}{C}\delta P.
\end{aligned} \tag{2.24}$$

By assuming an instantaneous photon energy deposition process and full energy conversion into TES temperature changes, the initial conditions to this set of equation are

$$\delta I(0) = 0, \qquad \delta T(0) = E/C. \tag{2.25}$$

This set of equation can be written as a matrix differential equation

$$\begin{bmatrix} \dfrac{d\delta I}{dt} \\ \dfrac{d\delta T}{dt} \end{bmatrix} = \begin{bmatrix} -\dfrac{1}{\tau_{el}} & -\dfrac{\mathcal{L}_I G}{I_0 L} \\ \dfrac{I_0 R_0}{C}(2+\beta_I) & -\dfrac{1}{\tau_I} \end{bmatrix} \begin{bmatrix} \delta I \\ \delta T \end{bmatrix} + \begin{bmatrix} \dfrac{\delta V}{L} \\ \dfrac{\delta P}{C} \end{bmatrix}, \tag{2.26}$$

with initial condition

$$\begin{bmatrix} \delta I \\ \delta T \end{bmatrix} = \begin{bmatrix} 0 \\ \dfrac{E}{C} \end{bmatrix}. \tag{2.27}$$

By taking δV and δP to be zero, which means the absence of noise, the differential equations take on homogeneous form. The analytical solution to this set of rank-2 linear differential equation can be found by calculating the eigenvectors and eigenvalues of the corresponding coefficient matrix, and is expressed as

$$\delta I = \frac{\Delta T_0 C(\tau_I\lambda_1+1)(\tau_I\lambda_2+1)}{\tau_I^2(\lambda_1-\lambda_2)I_0R_0(2+\beta_I)}(e^{\lambda_2 t}-e^{\lambda_1 t}) \tag{2.28}$$

$$\delta T = \frac{\Delta T_0}{\tau_I(\lambda_1-\lambda_2)}[(\tau_I\lambda_1+1)e^{\lambda_2 t}-(\tau_I\lambda_2+1)e^{\lambda_1 t}]. \tag{2.29}$$

Here λ_1 and λ_2 are the eigenvalues of the coefficient matrix, and are the inverse of the characteristic signal decay times. They have the form

$$\lambda_{1,2} = -\frac{1}{2}(\frac{1}{\tau_{el}}+\frac{1}{\tau_I}) \pm \frac{1}{2}\sqrt{(\frac{1}{\tau_{el}}-\frac{1}{\tau_I})^2 - 4\frac{R_0\mathcal{L}_I}{\tau L}(2+\beta_I)}. \tag{2.30}$$

The mathematical procedure is described in Appendix A.1.

Figure 2.5 shows the simulated current and temperature response of a TES following the calculation introduced in this section.

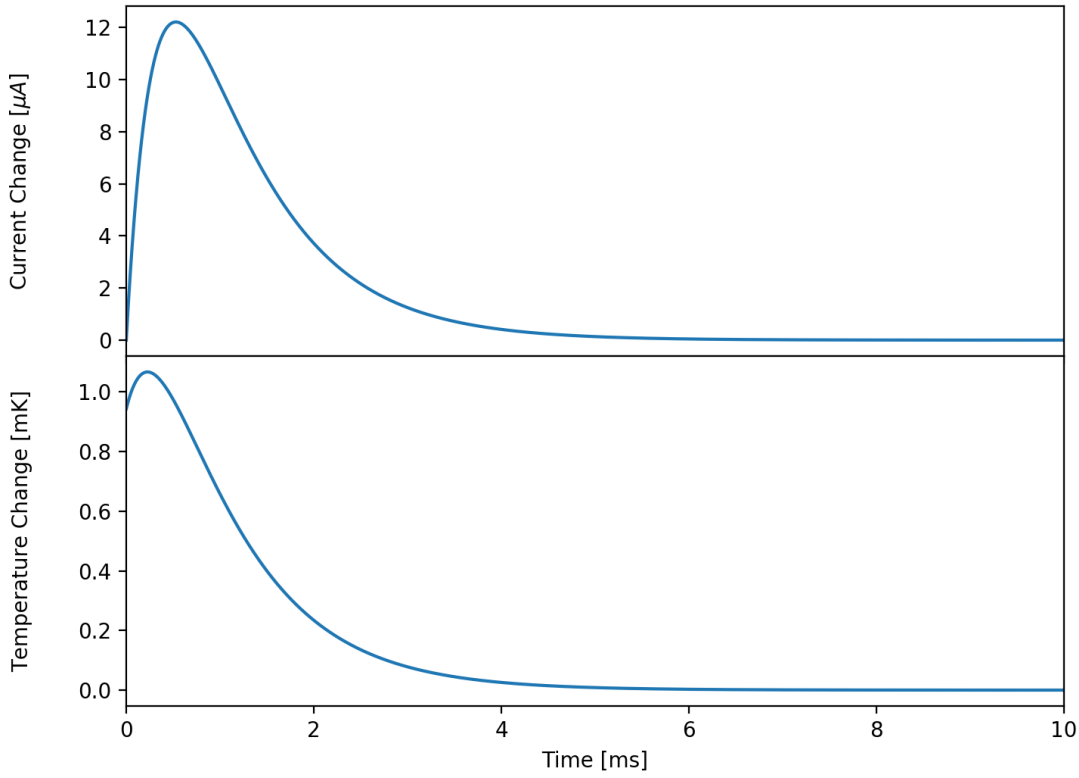

Figure 2.5. Simulated TES current and temperature response. The parameters used are $T_b = 75$ mK, $T_0 = 100$ mK, $I_0 = 29.7$ µA, $R_0 = 1.72$ mΩ, $R_L = 300$ µΩ, $\alpha_I = 70$, $\beta_I = 1$, $C = 1$ pJ/K, $G = 70$ pW/K, and the incident photon energy is 5.9 keV (the Mn $K\alpha_1$ energy).

2.2. Heat capacity

While the TES is a sensitive calorimeter, its energy resolution is limited by thermal noise, which is essentially the fluctuation of the number of phonons. For a TES that has a heat capacity of C and temperature sensitive α, operating at temperature T, its energy

resolution can be roughly calculated from [**18**]

$$\Delta E = 2.35\sqrt{4k_B T^2 C/\alpha}, \tag{2.31}$$

where k_B is the Boltzmann constant, and the factor of 2.35 is the Full-Width-at-Half-Maximum (FWHM) Gaussian distribution factor.

Based on Equation (2.31), getting good energy resolution requires that the TES have low heat capacity and low critical temperature. However, the temperature rise of a TES as stated in Equation (2.27) is inversely proportional to the heat capacity. The heat capacity should not be too small in the sense that the TES may saturate easily. Its value should be carefully designed based on the TES dynamic range, and the target energy.

In some applications, the sensor should be massive enougth to effectively stop X-rays, and be large enough to have large photon collection area. Therefore, a bulk material is usually connected with the TES sensor as a photon absorber. A design of a TES array with large absorbers for Energy Dispersive X-Ray Diffraction and Compton scattering measurements is presented in Section 3.1.

In addition, the material for the absorber needs to be carefully selected. Its heat capacity should not be too large that the energy resolution degrades, nor too small that the TES temperature saturates easily. It also needs to have good heat transfer capability, so that photon energy deposited in the absorber quickly transfers to the TES with little loss. The material being used for TES absorbers can be classified into three categories: superconductors, semi-metals and normal metals. The most commonly used materials are summarized in Table. 2.1.

Table 2.1. Properties of the most used absorber materials for 100 keV photons in 100 mK TES sensors.

material (Z)		$c_v[J \cdot K^{-1} \cdot m^{-3}]$	$\mu\ [m^{-1}]$	thickness $[\mu m]$ for 18% absorption
superconductor	Ta (73)	0.01	7162	27
	Sn (50)	0.01	1226	162
	Pb (82)	0.09	6298	32
semi-metal	Bi (83)	0.39	5592	35
normal metal	Au (79)	7.14	9965	20
	Cu (29)	9.80	411	483

In superconductors, electrons couple into Cooper pairs and do not carry heat, so the specific heat capacity and thermal conductance are both low. This is opposite to normal metals. For the semi-metal Bi, due to the lack of heat carriers, the specific heat capacity is low. In particular, Bi (bismuth) is a compelling material compared to gold (Au) because it has comparable X-ray detection quantum efficiency but an order of magnitude smaller specific heat capacity [**21**]. Both evaporated [**22**] and electroplated [**23**] Bi have been extensively used for X-ray TESs. In addition, bulk, single-crystal Bi glued to silicon microcalorimeters [**24**] has also been examined. A spectra analysis and microstructure characterization of Bi absorbers are presented in Chapter 4.

CHAPTER 3

TES design and simulations

This chapter presents two theoretical studies of TESs. Section 3.1 shows details on a TES designed for energy dispersive X-ray diffraction (EDXRD) and Compton scattering measurements. Section 3.2 models the resistive transition feature of TESs with different geometric designs. The text and figures in this chapter draw heavily from my papers [**25**] and [**26**].

3.1. TES design for EDXRD and Compton profile experiments

3.1.1. Application

The TES is a promising tool for spectroscopy applications in the very hard X-ray regime ($\sim$ 100 keV). It has exhibited close to unit quantum efficiency and energy resolution of $\Delta E = 22$ eV at 97 keV [**17**]. This work presents a design for a linear array of TES where the spatial resolution is utilized. Two potential uses are EDXRD and Compton scattering measurement in the very hard X-ray regime (>30 keV). EDXRD measures the sample's diffraction pattern at a fixed angle by using polychromatic photons and an energy dispersive detector. The detector's energy resolution limits the d-spacing (distance between planes of atoms) that can be resolved in the sample. Compared to the conventional angle dispersive X-ray diffraction that uses a monochromatic source and needs to rotate the sample, EDXRD is especially useful for situations in which the angles cannot be scanned and has the advantage that all scattering takes place into a small solid angle. This is a

very attractive feature for studies in extreme environments where the need for large X-ray windows can compromise the environmental chamber (e.g., diamond anvil cell) [**27**]. If an EDXRD detector has spatial resolution as well, then multiple parts of the sample could be measured at the same time, thus providing simultaneous imaging and diffraction information [**28**].

Compton scattering is the inelastic scattering of a photon by an electron. By detecting the energy and angle of the scattered photon, the electron momentum distribution can be obtained. In the past, experiments of this type were done with crystal analyzers [**3**], which offer good energy resolution but low counting efficiency. In this paper we present a design for a TES linear array detector for $\sim$ 100 keV X-rays that is suitable for EDXRD and Compton scattering experiments. This TES detector improves the energy resolution by an order of magnitude compared to the traditional Ge detector used in EDXRD, and can measure the full energy spectra without time-consuming crystal rotation, which is required in the crystal analyzers.

3.1.2. Absorber geometry and energy resolution

For energy dispersive X-ray diffraction (EDXRD) experiments, segmented Ge detectors have been used to achieve the desired spatial resolution and an energy resolution of $\sim$ 770 eV at 112 keV [**29, 30**]. A layout similar to these segmented Ge detectors could be used in a TES linear array for the same level of spatial resolution achieved in the bulk sample. To be specific, the proposed absorber width is 0.150 mm with 0.1 mm interval trenches. A 128-pixel array has a total width of 32 mm. To reach a d-spacing resolution

comparable to angle dispersive diffraction ($\sim$ 0.04 Å[**31**]), the detector energy resolution has to be improved the by an order of magnitude.

For high-energy Compton scattering measurements carried out in synchrotron facilities, given the typical monochromatic source bandwidth and the scattering angle spread, to achieve a momentum resolution of 0.1 a.u. (atomic unit), a detector energy resolution of 80 eV is needed [**3**]. This energy resolution requirement is similar to that of EDXRD.

Given the geometry and energy resolution limit above, we next find the proper absorber length, thickness and material. When dealing with high-energy photons, the choice of absorber material becomes crucial. It needs to be thick and composed of large Z elements to absorb photons. In order to achieve low thermal noise, the heat capacity should be low, but cannot be too low to avoid TES saturation. Besides, the material should have good thermal conductance to achieve fast thermalization. Under such criteria, in the hard X-ray regime, Ta (tantalum), Sn (tin), Pb (lead), Bi (bismuth), Au (gold), and Cu (copper) have been used as TES absorber materials [**32, 33, 34, 35**]. Their volume-specific heat capacity C_v at 100 mK (a typical operation temperature for this kind of detector), absorption coefficient μ at 100 keV, and the thickness needed to achieve $\sim$20% quantum efficiency (QE) are listed in Table I in Section 2.2.

Ta, Sn, and Pb are superconducting below 100 mK, where their thermal transfer is greatly reduced because the electrons are bound into Cooper pairs that do not carry heat. Au and Cu as normal metals have high thermal conductivity, and their values have been well studied. However, the high heat capacities of Au and Cu limit the quantity that can be used in an absorber without degrading the energy resolution of the TES. To increase the QE without losing energy resolution a combination of Au and Bi can be used [**18**].

However, due to the lack of information on the thermal conduction properties of Bi, in this work we consider an absorber made only of Au, with a thickness that will guarantee QE ∼20%. Given the energy resolution formula (2.31), assuming $\alpha = 100$, and the operation temperature is T = 100 mK, for C = 96.4 pJ/K, an energy resolution of 10.7 eV can be achieved.

Based on these conditions, the absorber is designed to be 4.5 mm long, with 20 µm Au to achieve 18% quantum efficiency at 100 keV. The absorbers have an elongated shape in order to increase the collecting area, and this can lead to position dependence in the TES response, which is discussed in Section 3.1.4.

3.1.3. Other parameters

We follow the common design for the TES sensor as described in Ref. [**36**]. The TES has a normal resistance of $R_n = 9$ mΩ, and is biased at 15% R_n. Its critical temperature is 100 mK, and the heat bath has a temperature of 70 mK. The shunt resistor in parallel with the TES is 0.3 mΩ. For a 150 µm ×150 µm TES, its heat capacity (C_{TES}) is negligible compared to that of the absorber, and can be estimated from Ref. [**36**] to be 0.2 pJ/K at the TES critical temperature of 100 mK. The thermal conductance between the TES and the absorber should be as large as possible to avoid heat loss during the thermalization process caused by a photon event, and to minimize internal thermal fluctuation noise. A Cu patch between the TES and the absorber can be used as a thermal link [**36**]. Given its thermal conductivity at 300 K to be $\kappa_{300} = 398$ W/(mK) [**37**], with residual resistance ratio (RRR) of 5 (typical for our Cu films), its thermal conductivity at 4.2 K can be

calculated as [**38**]:

$$\frac{\kappa_{4.2}}{\kappa_{300}} = \frac{\text{RRR}}{71}, \tag{3.1}$$

and $\kappa_{4.2} = 28$ W/(mK). For a typical fabrication geometry, with thickness $d = 100$ nm, width $w = 10$ µm, and length $l = 10$ µm, the thermal conductance of

$$G_{ta} = \kappa_{4.2} \cdot \frac{d \cdot w}{l} \tag{3.2}$$

is calculated to be $2.8{\times}10^6$ pW/K.

Figures 3.1 and 3.2 show the physical layout and thermal model of the device. Perforations are made evenly along the edges of the TES sensor and the absorber, in order to change the thermal conductance to the thermal bath. The ratio between the size of the TES and that of the absorber gives a ratio between the respective thermal conductances (G_{th} and G_{ab}) of $G_{tb}/G_{ab} = 3/61$. Based on the experimental data in Ref. [**36**], reasonable assumptions for these quantities are $G_{tb} = 90$ pW/K and $G_{ab} = 1830$ pW/K.

When a photon hits a TES, the TES temperature and current change quickly, then relax back to the equilibrium state. Typically, an inductor is used in series with the TES to slow down the pulse response. For a microwave SQUID (superconducting quantum interference device) readout scheme, a reasonable bandwidth is around 100 kHz [**39**]. In order to have enough sampling points within the pulse rise time, the inductance L needs be larger than 100 nH. Furthermore, L cannot be so large that the electro-thermal system loses stability, which leads to an upper limit of 1000 nH. In this study, we choose $L = 700$ nH, a value typically used in our experiments.

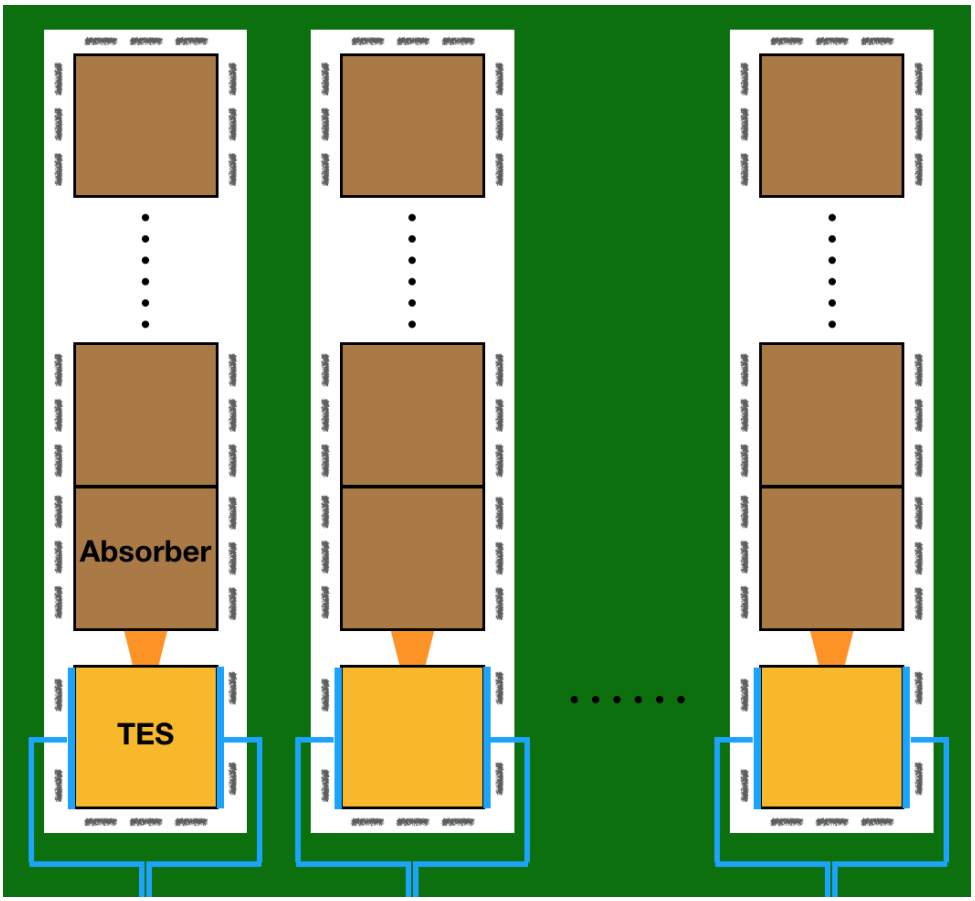

Figure 3.1. The physical layout of the TES array. The TES (yellow) is 150 µm × 150 µm, and the absorber (brown) is 150 µm × 4.5 mm. These two are thermally connected via a Cu stub (orange). The spacing between each pixel is 100 µm. This configuration offers one-dimensional spatial resolution in the horizontal direction. In order to simulate the position response, the absorber is divided to 30 squares. The devices are fabricated on a SiN membrane with 1 µm thickness (white areas), and the green area is the silicon base that connects to the cryogenic stage. Perforations are etched into the membrane evenly around the TES and absorber, so that the thermal conductance to the 70 mK heat bath is evenly distributed along the edges.

Given the strip layout of absorber, signal position dependence must be taken into account. Here we simulate the device signal response by dividing the absorber into 30 squared units longitudinally (Fig. 3.1), each having a heat capacity of $C_{\text{unit}} = 3.2$ pJ/K.

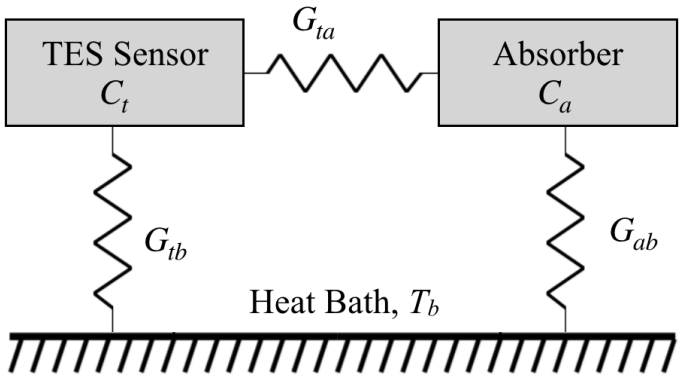

Figure 3.2. The device can be treated as having two thermal bodies that are the TES sensor with a heat capacity C_t and the absorber with a heat capacity C_a. They are thermally connected through a link of thermal conductance G_{ta}, and are in thermal contact with the heat bath at temperature T_b through links of G_{tb} and G_{ab}, respectively.

The signal response can be expressed by 32 electro-thermal differential equations, taking a form similar to that in Ref. [**40**]. Given that our experimental Au film has RRR = 2.8, $\kappa_{300} = 315$ W/(mK) [**37**], we can use Equations (3.1) and (3.2) to show that the thermal conductance between the Au absorber units $G_{\mathrm{abs-inter}}$ is 0.25 mW/K. When a photon with energy E_0 hits an absorber unit, it gives an initial temperature rise $\delta T(0) = E_0/C_{\mathrm{unit}}$ in that unit, while in other absorber units and the TES, the temperature and current changes are zero. With this initial condition, integrating the differential equations in time series, the signal response can be calculated numerically.

3.1.4. Simulation and results

We simulated the response of each absorber unit to a 100 keV photon. The current responses and deviations from the average are shown in Figure 3.3. The position dependence can be seen clearly. Due to the differences in the pulse shapes, the calculated pulse

energy will also be different, as will be shown later in this section. The pulse of the first unit deviates from the average more significantly compared with other pulses, especially after ∼1 ms. In this discrete simulation, the first absorber unit is qualitatively different to the others because of its connection to the TES. This difference is more obvious when the thermal conductance between the absorber and the TES is larger.

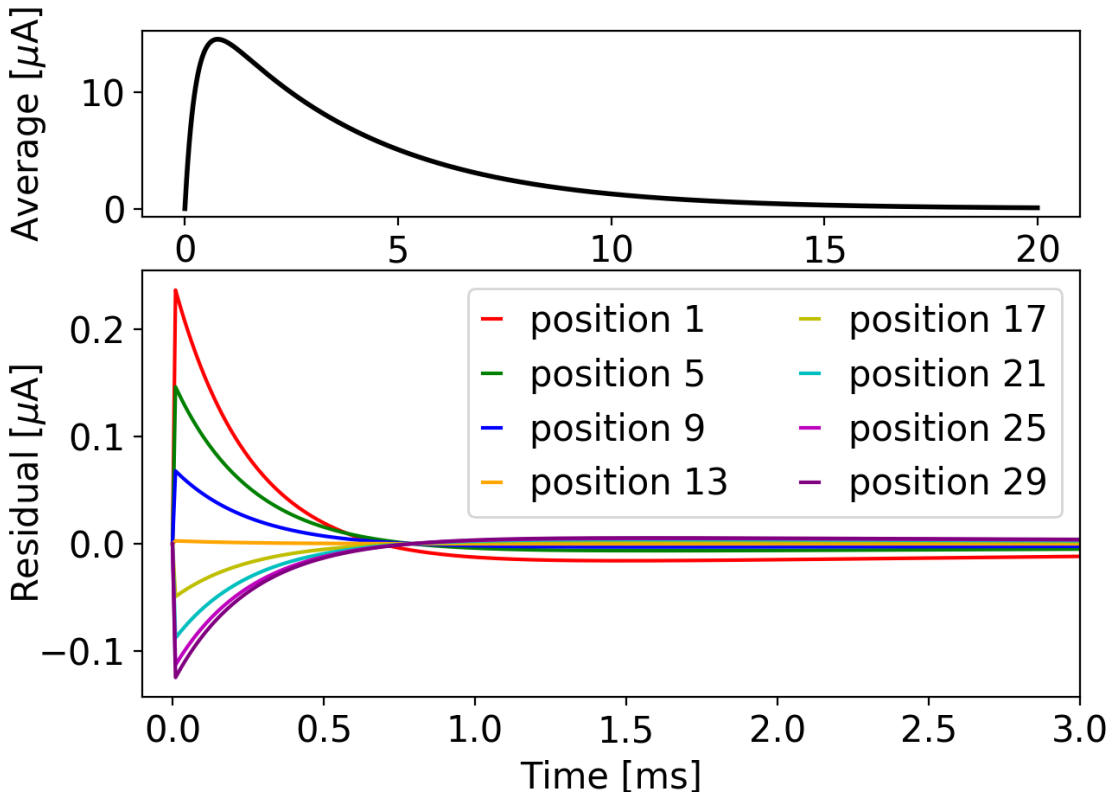

Figure 3.3. The average of the TES current pulse responses (upper) and the pulse deviations from the average (lower). Plots are showing signals from 8 representative incident positions that are every 4 units away from the TES. Each unit is 150 μm.

With the device parameter settings introduced in the previous section, within the simple two-body approximation (Figure 3.2), the theoretical noise [**41**] of the TES is

calculated and shown in Figure 3.4. Given the pulse sampling rate of 100 kHz as mentioned in Section 3.1.3, and the pulse duration time of $\sim$ 20 ms as shown in Figure 3.3, we choose the noise spectra frequency range to be 0 Hz - 50 kHz with a bin size of 5 Hz. In practical experiments, X-ray pulses are processed with the optimal filter method [**18**] (Section 8.1), and the average pulse shape of the 30 absorber units is usually used as the filter template. Following this routine, the device theoretical energy resolution is calculated to be 29.4 eV.

In order to evaluate the resolution degradation caused by position dependence, the 30 pulses for 100 keV photons hitting different regions are processed with the optimal filter, and the calculated energies are shown in Figure 3.5. The photon hitting the unit that is closest to the TES shows a significant deviation due to its skewed pulse response, which reduces the estimated photon energy when the optimal filter is applied to it. The FWHM (full width at half maximum) of this distribution is 21.6 eV, and this gives an overall resolution of

$$\Delta E_{\text{total}} = \sqrt{29.4^2 + 21.6^2} = 36.5 \text{ eV}. \tag{3.3}$$

This value satisfies the requirements of the target experiments. Furthermore, the degradation caused by the position dependence along the absorber can be improved by using more sophisticated pulse processing methods [**42, 43**] or the position dependence can be used to provide spatial resolution along the strip direction [**44**].

In summary, this work has designed a TES linear array with strip absorbers to measure Compton profiles and EDXRD up to 100 keV. Simulations has been conducted to assess the position dependence due to the large longitudinal dimension of the absorber. We

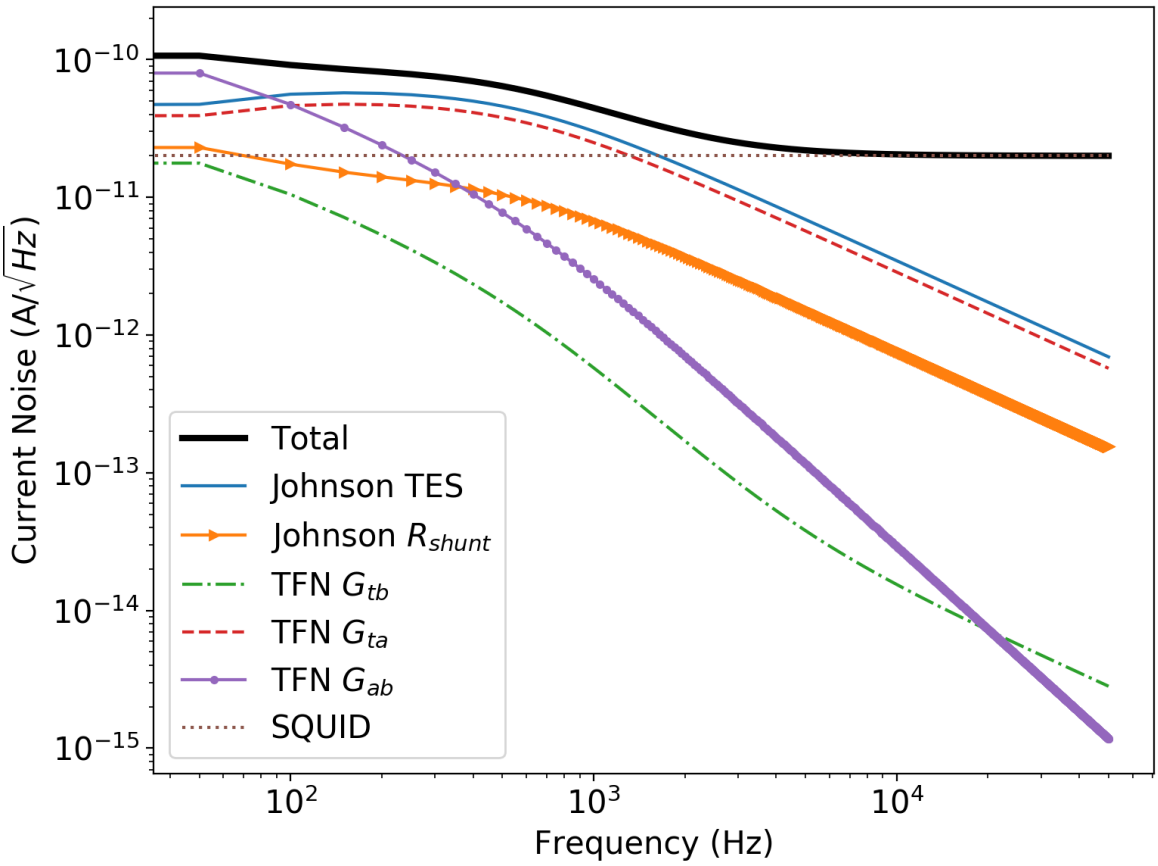

Figure 3.4. TES noise spectra. The noise sources taken into account are Johnson noise of the TES and the shunt resistor, thermal fluctuation noise (TFN) across the three thermal links from the two-body model, and noise from the SQUID. The TFN G_{ta} noise appears to have the same shape as the TES Johnson noise because the value of G_{ta} is much larger than G_{tb}. An example of TES noise that is measured from a real device can be found in Figure 7.6.

have achieved an overall energy resolution of 36.5 eV, which meets the requirements of the experiments. Preliminary fabrication tests are currently taking place to produce prototype detectors.

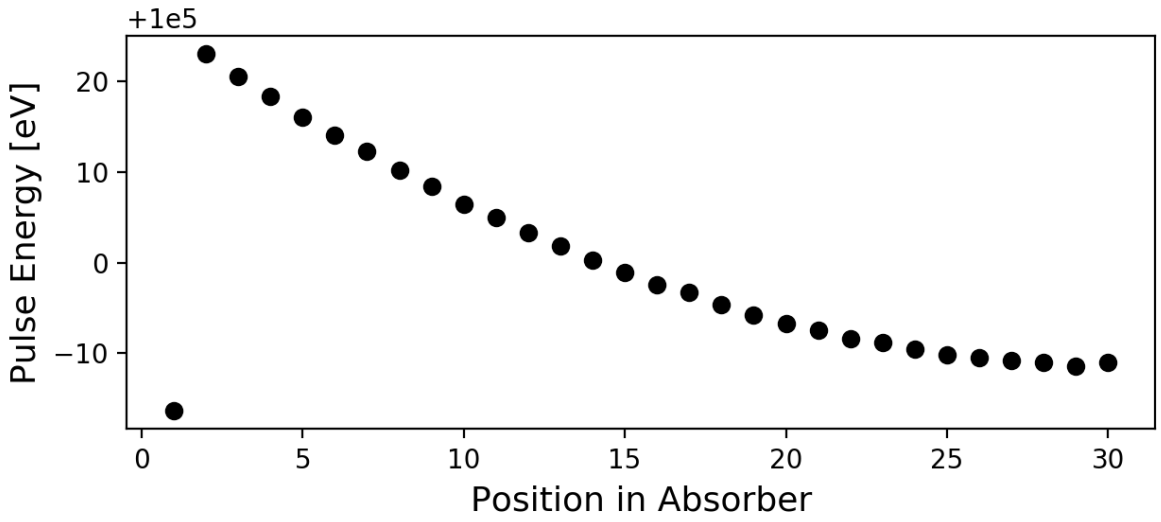

Figure 3.5. The energy of the photons hitting the 30 positions in the absorber calculated from the optimal filtering. The results show deviation from 100 keV. Position 1 is closest to the TES.

3.2. TES resistor network model

It was mentioned in Section 2.1 that in the small signal limit, the signal response of a TES can be expressed as electrothermal differential equations, and solved analytically. However, the TES response and specifically resistance as a function of current and temperature $R(I,T)$ is usually nonlinear over the full superconducting transition width [**45, 46**]. Knowledge of the full nonlinear $R(I,T)$ function is necessary to correctly describe the device response to large signals as well as its saturation and dynamic range. Multiple models have been used to describe the nonlinear transition shape of TESs [**46, 47**], including the resistively and capacitively shunted junction (RCSJ) model [**48**] for small dimension devices, that treats the TES as a weak link between superconducting leads; and the two-fluid model [**49, 50**] that describes the TES current as a superposition of a superconducting

(Cooper pair) and a normal (quasiparticle) current. The latter has shown good quantitative agreement with the current-voltage (I-V) curves measured from a 350 µm × 350 µm Mo-Cu bilayer TES [**50**]. However, it is also known that the geometry of noise-mitigating normal metal bars/banks patterned on the superconducting film influences the $R(I,T)$ transition shape [**51, 52**]. This is not accounted for in the simple two-fluid model. The effect of normal metal bars has been studied in a one-dimensional (1-D) scheme utilizing the Usadel equation [**51**], but has not been addressed in two dimensions (2-D). In this section, we present a resistor network model to calculate the TES transition shape given 2-D normal metal features of arbitrary geometry. The current distributions and $R(I,T)$ surfaces for some example TESs are obtained, and the dependence on the normal metal features is shown.

3.2.1. Two-dimensional resistor network model

In this model, the TES is represented as a 2-D "film" divided into small square units. Each unit is a square containing four identical resistors, one per side (Fig.1). In this way, currents can flow in both the longitudinal and the transverse direction. The neighboring units join at the resistor nodes. In the case of a unit representing a part of the TES where a normal metal feature is present (bars or banks - in orange in Figure 3.6, labeled "normal metal"), the resistance is fixed to be R_{metal}, as we assume these units are completely in the normal state due to the proximity effect. In the case of a unit where no normal metal features are present (in blue in Figure 3.6, labelled "transition region"), the resistance R depends on both the total current I flowing through the unit, and its temperature T. The net current flowing through a unit is calculated as $I = (I_x^2 + I_y^2)^{1/2}$ where I_x and I_y are the

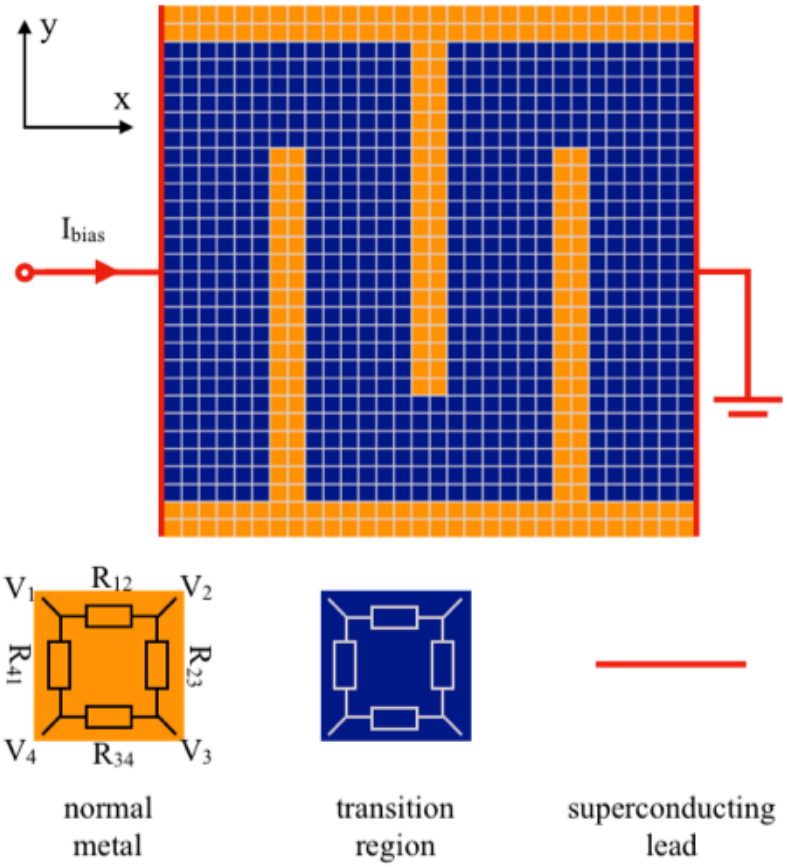

Figure 3.6. The TES is divided into small units that are connected in a 2-D network. The basic unit is a 4-terminal resistor. Adjacent voltage nodes V_1, V_2, V_3, V_4 are electrically connected via resistances R_{12}, R_{23}, R_{34}, and R_{41}, respectively. $R_{12} = R_{23} = R_{34} = R_{41} = \mathrm{R}$, and the total current is defined by $I = (I_x^2 + I_y^2)^{1/2}$, where x and y are longitudinal and transverse directions. The 2-D resistor network model of a 150 µm × 150 µm TES has normal metal banks (orange) on the edge along the current flow direction, three normal metal bars (orange) perpendicular to the current flow, superconducting leads (red), and the transition region (blue) where the resistances are a function of current and temperature. Each unit is a 5 µm × 5 µm square.

current components in the respective directions, while the temperature is assumed to be the same across the TES, ignoring the Joule heating effect and any potential non-uniform

cooling in the film. The $R(I,T)$ relation for each transition region unit is defined by the two-fluid model and will be introduced below.

The resistor network must obey a matrix equation representing Ohm's Law

$$[\mathbf{S}] \cdot \vec{V}_{\text{node}} = \vec{I}_{\text{node}}. \tag{3.4}$$

For an m×n 2-D network, $\vec{V}_{\text{node}}$ is an (m+1)(n+1) column vector that consists of the node voltages, while $\vec{I}_{\text{node}}$ is an (m+1)(n+1) column vector that consists of the net node currents. [**S**] is an (m+1)(n+1)×(m+1)(n+1) matrix consisting of the electrical conductances between each node and is constructed based on the values of the resistors in the network. By Kirchhoff's current law, the net current at each node must be zero, except for the two nodes representing the contacts with the bias leads, where the net current is $\pm I_{\text{bias}}$. Here the sign defines whether the current is flowing in to or out of the node (Figure 3.6).

The matrix [**S**] is singular, and is of rank (m+1)(n+1)×(m+1)(n+1)-1. Physically, this is because the node voltages are relative to an arbitrary ground voltage. This is resolved by fixing the voltage of one node. Here we set the voltage of the node connected to the ground to be zero (although it can be any arbitrary value). This changes the ground node Kirchhoff equation from

$$\vec{S} \cdot \vec{V}_{\text{node}} = -\vec{I}_{\text{bias}} \tag{3.5}$$

to

$$[0, 0, \cdots, 1, \cdots 0] \cdot \vec{V}_{\text{node}} = 0, \tag{3.6}$$

where $\vec{S}$ is all zero except the value one at the position that multiplies with V_{ground}. The modified set of Kirchhoff equations is now linearly independent, therefore the node voltages can be solved by

$$\vec{V}_{\text{node}} = [\mathbf{S}^{-1}] \cdot \vec{I}_{\text{node}}. \tag{3.7}$$

The current between any two nodes can then be calculated by dividing the voltage difference by the connecting resistance.

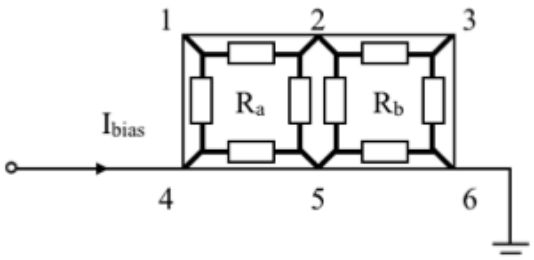

Figure 3.7. A simple 1×2 network has 2×3 = 6 nodes. The resistances in the first unit are denoted by R_a, and those in the second unit are R_b. A bias current I_{bias} is applied to node-4. Node-6 is grounded and its voltage is $V_6 = 0$

Figure 3.7 illustrates a simple network consisting of two four-terminal units. Following the steps introduced above, its node voltages can be calculated via Equation (3.8).

$$\begin{bmatrix} v_1 \\ v_2 \\ v_3 \\ v_4 \\ v_5 \\ v_6 \end{bmatrix} = \begin{bmatrix} \frac{2}{R_a} & \frac{-1}{R_a} & 0 & \frac{-1}{R_a} & 0 & 0 \\ \frac{-1}{R_a} & \frac{2}{R_a}+\frac{2}{R_b} & \frac{-1}{R_b} & 0 & \frac{-1}{R_a}+\frac{-1}{R_b} & 0 \\ 0 & \frac{-1}{R_b} & \frac{2}{R_b} & 0 & 0 & \frac{-1}{R_b} \\ \frac{-1}{R_a} & 0 & 0 & \frac{2}{R_b} & \frac{-1}{R_a} & 0 \\ 0 & \frac{-1}{R_a}+\frac{-1}{R_b} & 0 & \frac{-1}{R_b} & \frac{2}{R_a}+\frac{2}{R_b} & \frac{-1}{R_b} \\ 0 & 0 & 0 & 0 & 0 & 1 \end{bmatrix}^{-1} \begin{bmatrix} 0 \\ 0 \\ 0 \\ I_{\text{bias}} \\ 0 \\ 0 \end{bmatrix}. \tag{3.8}$$

The geometry of the TES determines the 2-D network and the matrix [**S**]. Figure 3.6 shows the network model of a 150 µm × 150 µm TES film with parallel normal metal banks and three perpendicular normal metal bars. The width of the banks and bars is $\sim$ 10 µm, therefore the TES is divided into 5 µm × 5 µm squares, providing sufficient resolution to accurately represent the geometry. The units representing the normal metal region use resistor values of $R_{\text{metal}} = 8.94$ mΩ, and the transition region units use a normal state resistance of $R_n = 23.54$ mΩ in the two-fluid model calculation. These numbers are based on Ref. [**52**], but with the four-terminal unit configuration the resistor values are doubled relative to the measured sheet resistance, to ensure that any square section of the overall network has the correct total resistance. Theoretically, the resistance of the superconducting leads is zero. However, to avoid null values in the simulation, a very small value of 1 nΩ is used instead.

The two-fluid model defines the resistance of a superconductor in the transition region $R(I,T)$ as:

$$R(I,T) = \begin{cases} \left[1 - \frac{c_I I_{c0}}{I}\left(1 - \frac{T}{T_c}\right)^{3/2}\right] c_R R_n, & I > \frac{c_I I_{c0}}{I}\left(1 - \frac{T}{T_c}\right)^{3/2}, \\ 0, & I < \frac{c_I I_{c0}}{I}\left(1 - \frac{T}{T_c}\right)^{3/2}. \end{cases} \tag{3.9}$$

This model has shown good agreement with experimental results when applied to the entire TES [**47, 50**]. In this equation, T_c is the critical temperature, I_{c0} is the critical current at zero temperature, and c_I and c_R are unitless coefficients. T is the temperature, assumed to be the same for all the units, and I is the current passing through a unit. In the case of our 2-D network model, the current I depends on the distribution of R.

Because R and I are mutually dependent, and because this relationship is nonlinear, as suggested by Equation (3.9), the solution to Equation (3.7) can only be obtained by numerical methods. We choose to solve Equation (3.7) iteratively with the Newton-Krylov method, using finite-differences to estimate function derivatives. To avoid non-convergence of the numerical solver in the zero-derivative region when $I < I_{c0}$ in Equation (3.9), $R(I,T)$ is modified to have a constant slope as a function of current below 5% R_n, as shown in Figure 3.8. In order to evaluate the influence of this modification, we simulated the $R(I,T)$ of a TES with no normal metal structures via the 2-D resistor network, and compared it to the prediction of the two-fluid model applied to an equivalent single-body TES. The two results should be effectively identical, with a uniform current distribution through the 2-D network, resulting from a uniformly segmented resistance. The only difference between the two approaches arises from the modification in the 2-D network model of the two-fluid $R(I,T)$ below 5% R_n. The comparison shows that the

difference caused by this modification is below 5% R_n^{total} (R_n^{total} is the total normal resistance of the device), which we deem negligible. With this point verified, we believe this 2-D network model is capable of describing how typical TES geometry parameters, such as number of bars, bar spacing, and overall dimensions, influence device behavior. The results of these simulations for some specific TES designs, chosen to be similar to those of Ref. [**53**], are described in the following section.

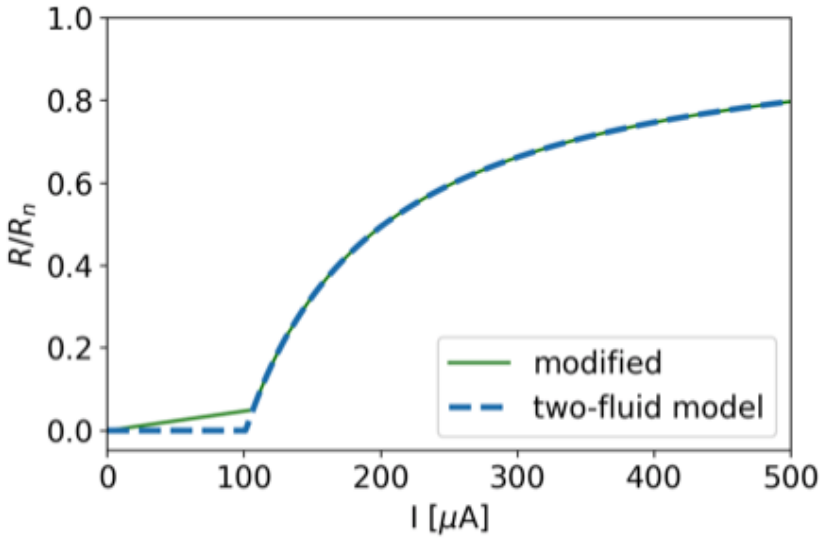

Figure 3.8. The two-fluid model $R - I$ relation (blue dashed line), and the modified $R - I$ relation (green line) that does not have a zero-derivative region below 5% R_n which is suitable for numerical iteration purposes.

3.2.2. Results and discussion

To explore the influence of some common TES design parameters, we decided to focus on a set of seven different designs labeled with the following scheme: x-sq. y-bars, where x represents the aspect ratio (width/height) of the device and y represents the number of bars present. It should be expected that changing the width of the device results in a

different total TES resistance, and therefore a different trajectory on the $R(I,T)$ surface under voltage bias, while changing the number of bars may affect the current distribution in the device, defining a different shape for the $R(I,T)$ surface. The specific designs under examination are based on those described in Ref. [**53**] and illustrated in Figure 3.9. We also used the material and device parameters measured in Ref. [**53**] (see Table I), providing means to validate the model against the experimental measurements presented in that work.

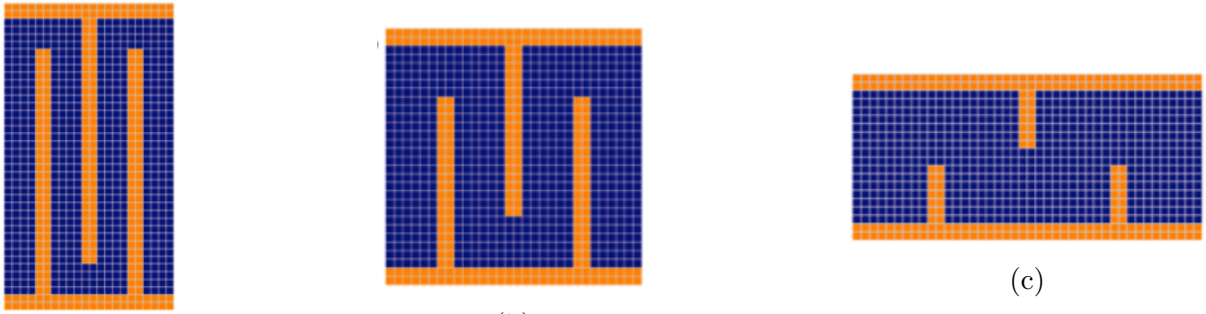

(a) (b) (c)

Figure 3.9. The 2-D layout of the TESs under study: (a) 106 µm × 212 µm (1/2-sq.) TESs are made with 3 bars and 2 bars; (b) 150 µm × 150 µm (1-sq.) TESs are made with 4 bars and 3 bars; (c) 212 µm × 106 µm (2-sq.) TESs are made with 5 bars, 4 bars, and 3 bars.

However, not all the parameters required here have an immediate equivalent in that paper – in particular, the measured two-fluid model parameters of Ref. [**53**] are those appropriate to an entire TES including bilayer and normal metal features, while in the 2-D resistor network both units with and without normal metal features are present at the same time, therefore some assumptions had to be made and are described below.

In Table I, the critical temperature of a unit resistor has been defined as dependent on the overall design. This approximates the lateral proximity effect induced by the

normal metal features, as our model does not directly account for this effect. The critical temperature of each unit is the T_c of the corresponding device measured in [**53**].

The transition unit I_{c0}, on the other hand, is assumed to be the same for all TESs. Experimental data suggest that the critical current at zero temperature for a TES is roughly proportional to the spacing between the normal metal bars [**53**]. This is likely because in the superconducting state, the current meanders around the bars, and the width of the current path is the bar spacing. For devices with the same bar spacing, the I_{c0} variation is small; therefore, we chose one TES design to obtain the unit I_{c0} value: the 1/2-sq. 2-bar device with a total I_{c0} of 7.8 mA and 5 inter-bar units gives a per-unit I_{c0} = 1.48 mA. This value is applied to all other simulated devices.

According to Equation (3.9), the value of c_R should be unity when the TES is in the normal state, to obtain the correct total normal state resistance, and c_I should be unity when $T = 0$. However, they have both been experimentally observed to have a smaller value when the TES is biased at the transition [**50, 53**], and theoretical considerations based on the phase-slip model of the superconducting transition also suggest c_R should vary with temperature [**49, 54**]. However, without any detailed model of the dynamics of phase-slip lines in 2-D films, or experimental measurements of the parameters those models might require, we kept c_R and c_I as fixed parameters in each of our simulations. Instead, we simply carried out separate calculations with manually chosen values of c_I = 0.79 (as measured in [**53**]) and c_R = 0.25, 0.5, and 1, to account for its variation. Any one calculation presented here is only strictly valid, therefore, for the region of the

transition where c_I and c_R are close to these chosen values. Until a model for these two-fluid parameters is developed and we can identify those regions, we present our results over the full transition width.

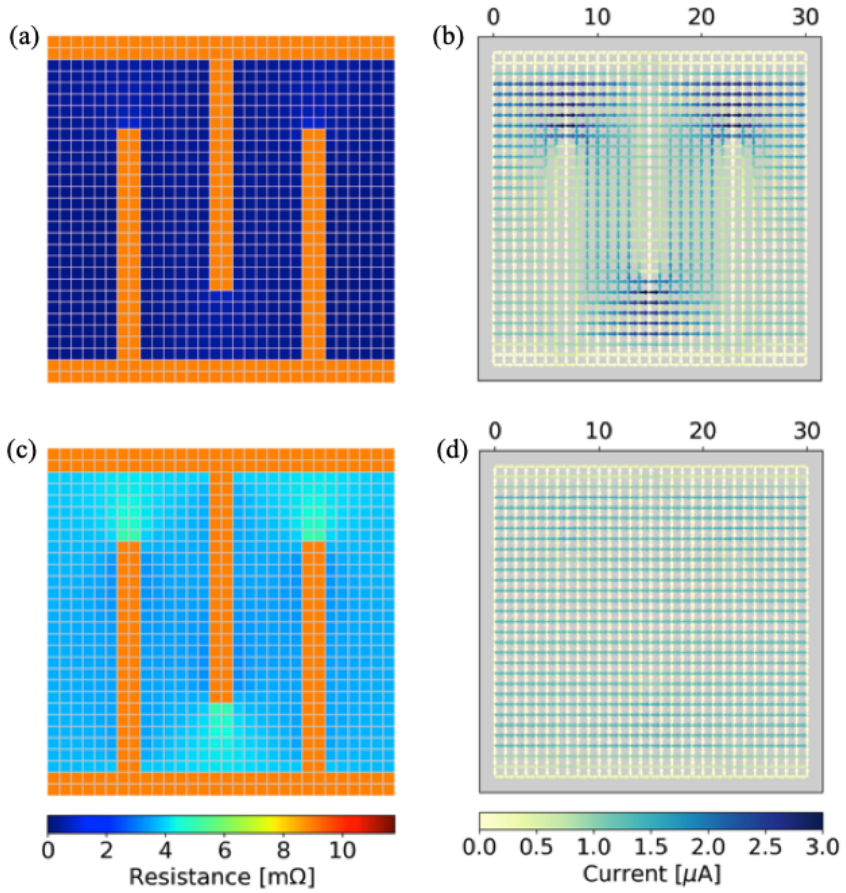

Figure 3.10. The resistance and current distribution of the 1-sq. 3-bar TES under different bias conditions. (a) (b) $I_{\text{bias}} = 35$ µA, T = 72 mK, and the TES at 12% R_n^{total}. (c) (d) $I_{\text{bias}} = 35$ µA, T = 72.8 mK, and the TES at 44% R_n^{total}.

Figure 3.10 shows the simulated resistance and current distribution of the 1-sq. 3-bar devices under different biases. Operating the device at a fixed temperature of $T = 72$ mK, as the TES bias current I_{bias} increases from zero, several phenomena develop in the

simulation. Initially the current flows through the device encountering no resistance (or very little, due to the approximation described previously Figure 3.8). This is because, although there are normal metal (resistive) regions present, a lower resistance path that meanders around the bars is present. Further increasing I_{bias} will cause the current through a unit to increase, along with the total resistance along the meander path. In this scenario, the current will still meander around the bars, because the total resistance of that long path is still below the equivalent resistance that the current would experience if it would go via the shorter, direct path intersecting the bars. Figure 3.10a and Figure 3.10b illustrate this for a device biased at $\sim 12\%$ R_n^{total}. Further increasing I_{bias} will increase the transition unit resistance to a point where the direct path now has lower resistance, and so it is preferred by the current. This is illustrated in Figure 3.10c and Figure 3.10d, at $\sim 44\%$ R_n^{total}. This behavior indicates that the current flow pattern in a TES with bars is dependent on the bias position in the transition. Similar current distribution dependence on bias has been reported in Ref. [**52**], although obtained via a different modelling and measurement technique.

Repeating this calculation at different values of T generates a 3D map of the $R(I,T)$ function for this device, as shown in Figure 3.11a for a 2-sq. 3-bar device, and Figure 3.11b for a 2-sq. 5-bar device. Comparing the two $R(I,T)$ surfaces shows (Figure 3.11) that when biased beyond $\sim 20\%$ R_n^{total}, the transition shapes of the two devices are about the same. Although the two devices have a different number of bars and different bar spacing, at those biases the current is flowing through the TES uniformly, irrespective of the bar layout. Conversely, while biased below $\sim 20\%$ R_n^{total}, the device with the larger bar spacing (2-sq. 3-bar) shows a sharper transition; this is due to the wider

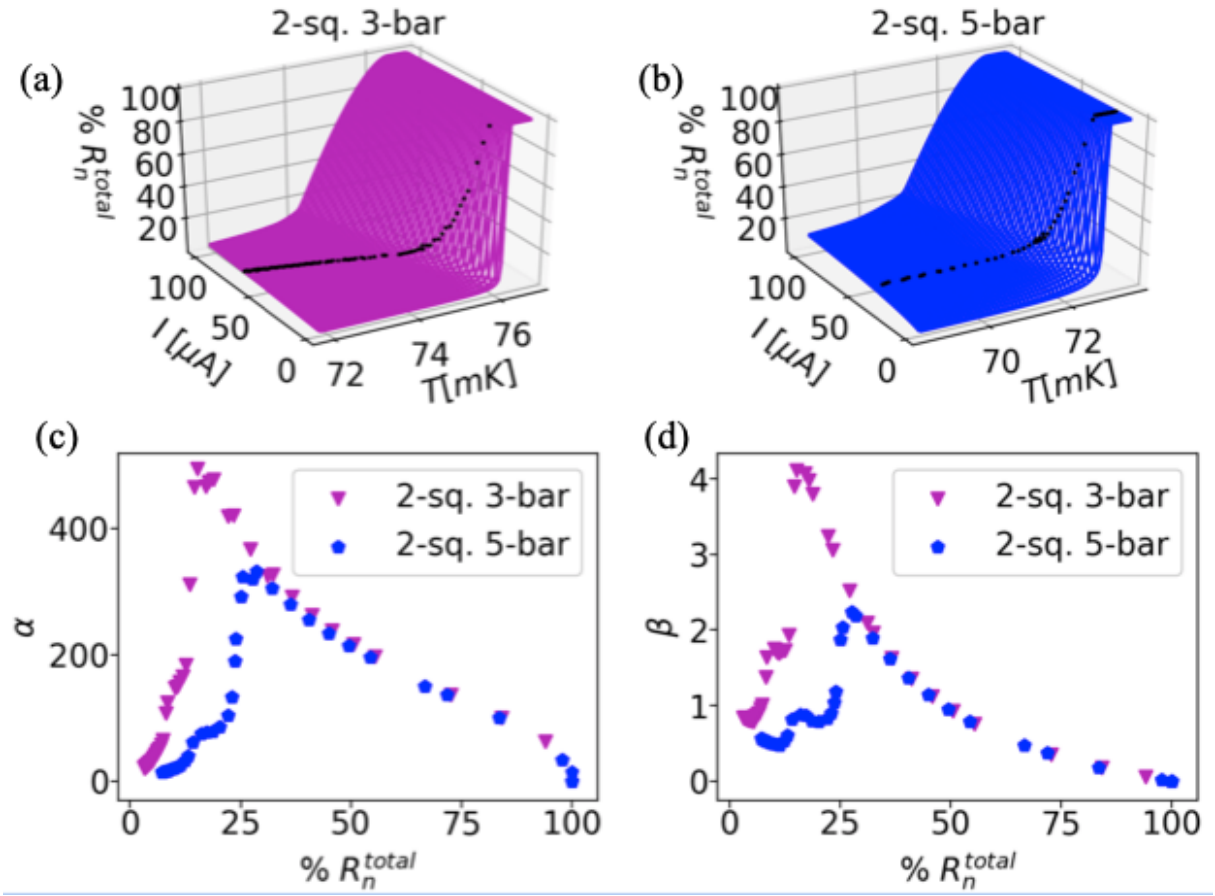

Figure 3.11. TESs with the same shape but different bar spacing: (a) 3-bar, (b) 5-bar. The transition shape changes around 20% R_n^{total} due to the current distribution pattern change. At low bias, the transition of the 3-bar TES is sharper due to its larger bar spacing, which is clearly shown by the α and β values in (c) and (d), respectively.

current path available between bars. It can therefore support a larger critical current, making the transition width narrower. This difference is more evident in the comparison of the thermal sensitivity α, and current sensitivity β, defined in Section 2.1, shown in Figure 3.11c and Figure 3.11d respectively. (I_0, T_0) are the TES bias points represented by the black trajectories on the re-spective $R(I, T)$ surfaces in Figure 3.11a, Figure 3.11b. These trajectories are obtained by combining the simulated $R(I, T)$ with Equation (7.2)

for the Joule power and cooling power balance. The thermal conductance between the TES and the thermal bath is G = 100 pW/K, the exponential index is $n = 3$, and the bath temperature T_{bath} is 55 mK. These curves represent the experimentally measurable I-V relation under voltage bias. Both devices exhibit similar trends for α and β as a function of % R_n^{total}. Initially the values are fairly small, followed by a sudden increase between 10% and 20% R_n^{total}, corresponding to the steep region in the $R(I,T)$ surface. In this region, as the bias increases, more transition units change from the superconducting state to the steep resistive state as represented in Figure 3.8. α and β for the 2-sq. 3-bar device reach values almost double those reached by the 2-sq. 5-bar device, representative of the enhanced steepness of the transition. This is a well-known phenomenon associated with the presence of normal metal bars on TESs – increasing the number of normal metal bars reduces α. Biasing the device higher in the resistive state results in a reduction of both quantities, due to the decrease in steepness of the resistive transition in both I and T. This is also a phenomenon reported in many experimental papers, for example Ref. [**45**]. At even higher bias ($> 40\%$ R_n^{total}) the curves for the two devices collapse onto each other, due to the redistribution of the current in the network. The $R(I,T)$ surface is no longer affected by the presence of the bars, but only by the lateral dimensions of the TES, identical in both devices.

Following the same approach, and maintaining the values of G and T_{bath} fixed, we have run simulations for all the seven types of devices described above. Figure 3.12 compares α for these devices. As in the previous discussion, α scales inversely with the number of bars for otherwise identical devices, independent of the device aspect ratio. Also, devices with an increasing aspect ratio, but the same number of bars, show an increase in α over

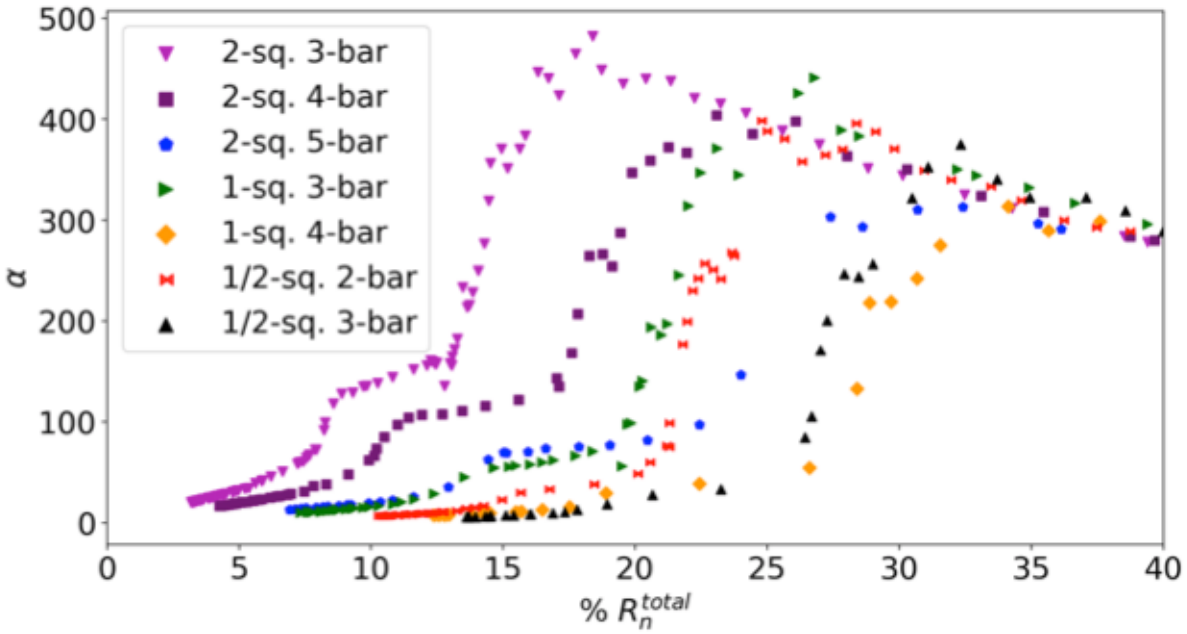

Figure 3.12. The α values throughout the transition for the seven TESs. They show a clear correlation with the device design details, such as number of bars, spacing between bars and number of squares in the low bias regime.

a wide range of % R_n^{total} biases. Both these results agree with what is experimentally seen in [**53**], suggesting this model is correctly showing the changes in TES transition steepness due to either the device dimensions (i.e. R_n^{total} and consequently I_0) and/or the number and spacing of bars (i.e. I_{c0}) [**53**]. These results demonstrate the predictive power of this model.

The previously described simulations all use a fixed value for $c_R = 0.5$, chosen as an average value at low bias among those reported for these kinds of devices in [**53**]. However, c_R varies through the transition, and it is smaller at lower bias points and increases with bias. Equation (3.9) shows that a smaller c_R will result in a lower resistance in the transition region units, and consequently the current will prefer to meander around the

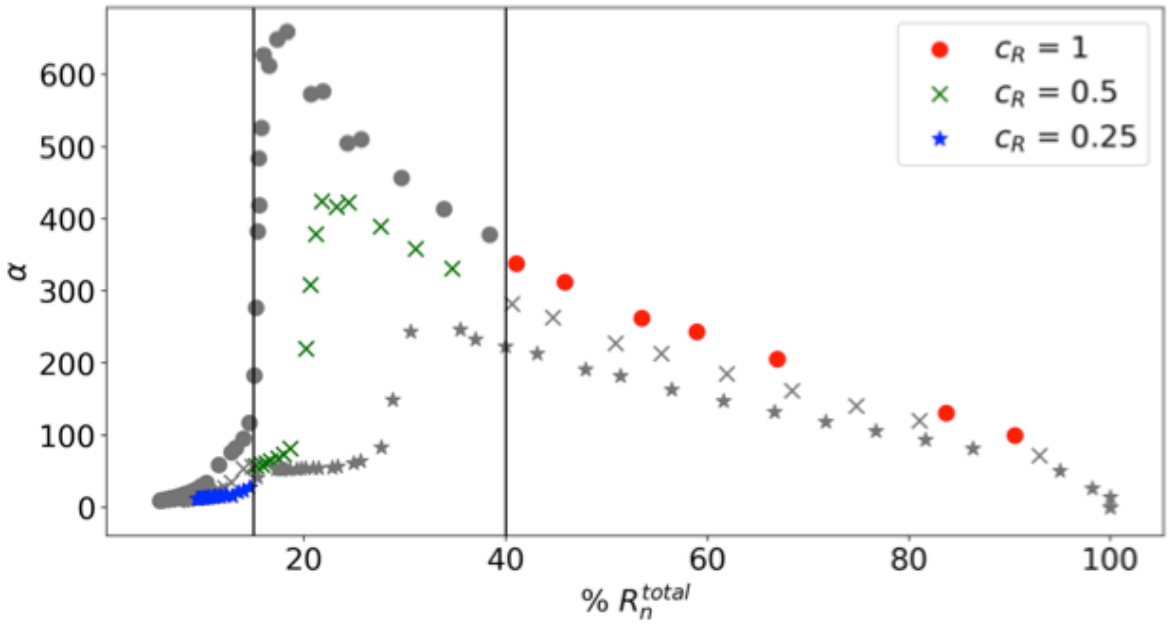

Figure 3.13. The α values of the 1-square 3-bar TES for $c_R = 1$ (round dots), $c_R = 0.5$ (crosses), and $c_R = 0.25$ (stars). The plot is divided into three regions by the 15% and 40% boundaries. The α values that are using c_R values suitable for each region are colored, while others are marked in grey. The actual dependence of α on $\%R_n^{total}$ is a combination of the entire set of curves that can be generated by varying c_R from 0 to 1, of which the three present are a representative example.

normal metal bars until higher biases, and vice versa for higher values of c_R. Varying c_R can consequently generate a family of curves of the kind showed in Figure 3.13 for a given device. Due to the lack of experimental data on the dependence of c_R on the bias and the difficulty in estimating the materials parameters that determine this phenomenological parameter (for example, the charge imbalance relaxation length [**50**]), for now its influence on TES transition shape can only be evaluated qualitatively. Figure 3.13 shows the values of α throughout the transition for the 1-sq. 3-bar device when using $c_R = 1$, 0.5, and 0.25. Based on the c_R values measured in Ref. [**53**], this plot is divided into 3 regions; each

region provides α values with a c_R best estimated at that bias. The actual dependence of α on % R_n^{total}, i.e. the actual shape of the TES transition, can likely be approximated by a combination of these three curves. The model will be fairly straightforwardly improved if a quantitative model for c_R and c_I can be developed.

3.2.3. Summary

While the engineering of TES transition shapes has been performed experimentally through the manipulation of 2-D features, a predictive 2-D model has until now been lacking. In this section, we present a 2-D resistor network model which can calculate the current distribution and overall $R(I,T)$ surface for TES devices with arbitrary geometry including normal metal features. The TES is divided into 4-terminal units, with resistances based on the superconducting two-fluid model and calculated self-consistently based on the temperature and net current, allowing for the calculation of the current distribution and total resistance of the device. The model has been used to simulate the transition shape and the current-voltage characteristics of a series of previously experimentally measured devices of varying dimensions and normal metal features. The simulations show how the normal metal features force the current flowing through the TES to meander around them at lower biases, while at higher biases the current tends to flow more uniformly through the entire width of the device, independently of the specific bar arrangement. The simulations also show how the different bar designs affect the steepness of the TES transition, replicating phenomena experimentally observed, such as the dependence of α on the number of bars. Our model shows qualitative agreement with experimental results, and therefore represents a powerful tool to guide the design of TESs with normal metal

features and other nonuniform geometries. In the future, more complex effects such as localized heating and the lateral proximity effect could be implemented in this 2-D model. It may also be possible to study the noise mitigating mechanisms of the normal metal features.

CHAPTER 4

Bismuth used for TES absorber

As mentioned in Section 2.2, Bi is a competitive material for TES absorbers because it has high X-ray stopping power and low specific heat capacity. However, another important property required in absorber materials is good thermal conductivity. Heat trapped or lost in the absorber will cause the energy measured to be less than its real value. When measuring an emission spectrum, this will produce a non-Gaussian low-energy (LE) tail in the energy peak. This LE tail not only degrades the photon collecting efficiency, but it also blurs the adjacent energy peaks. It has been observed that evaporated Bi absorbers produce this non-Gaussian reponse [**55**]. This chapter presents a study of Bi absorbers deposited with electroplating and evaporating techniques. It is observed that their spectral reponses are different, which we will see is due to their distinct microstructure. The text and figures in this chapter draw heavily from my papers [**36**] and [**56**].

4.1. Detector design

We have designed a TES that is compatible with electroplated (elp) and evaporated (evap) depositions (Figure 4.1). The TES is a molybdenum/copper (Mo/Cu) bilayer with Cu banks and bars on top for transition-parameter control and noise suppression [**57**]. The transition temperature of these TESs is $\sim$ 100 mK. The absorbers are positioned to the side of the TES and attached to the Cu banks via a 0.2 µm thick Au layer. An additional 0.8 µm of Au forms the base of the absorber. The Evap-Bi is deposited via a lift-off

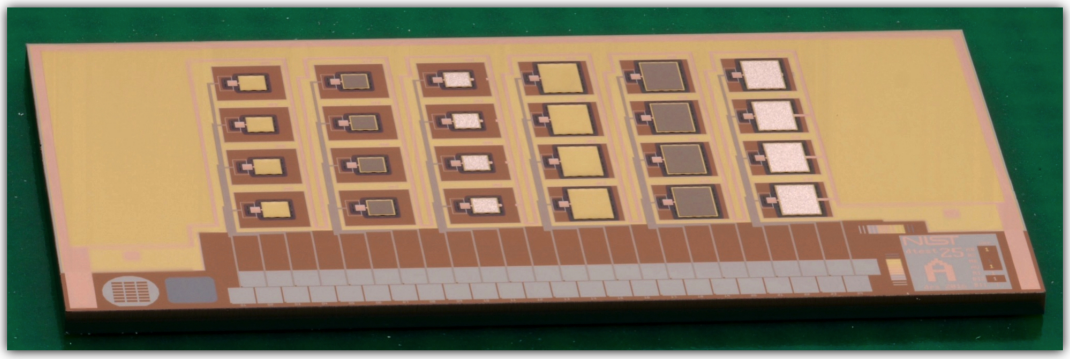

(a)

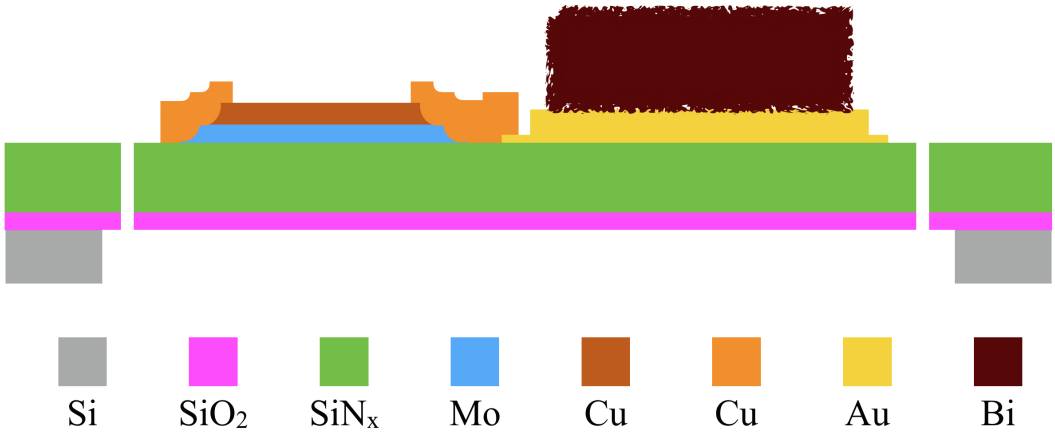

(b)

Figure 4.1. (a): Photograph of the TES die (7 mm × 14 mm). There are two sets of devices with small and large area absorbers designed for X-rays ranging up to ∼ 10 keV and ∼ 30 keV, respectively. For each device size there are three types of absorbers, with differing materials, from left to right: Au, Au/Evap-Bi and Au/Elp-Bi. For all absorbers the Au is 1 µm thick, and the Bi is 3 µm thick. (b): Schematic representation of the cross-sectional view of a device (not to scale).

process, while the Elp-Bi is electrodeposited [**58**] via a patterned Au seed layer with a Cu current path that is subsequently removed. Each type of Bi absorber is 3 µm thick, which has the potential to offer ∼ 76% quantum efficiency at 6 keV and ∼ 8% at 30 keV. The devices are grouped in two sets, designed for small (340 µm × 340 µm) and large (530 µm

Table 4.1. Representative thermal conductances and heat capacities of the different type of pixels.

Size	Small pixel			Large pixel		
Pixel perimeter (µm)	1860			3000		
Absorber material	Au	Au/Evap-Bi	Au/Elp-Bi	Au	Au/Evap-Bi	Au/Elp-Bi
G (pW/K)	254.7	254.3	263.0	384.0	392.3	400.3
C (pJ/K)	1.2	1.2	1.1	3.1	2.9	3.0

$\times$ 720 µm) absorbers, with dynamic range up to $\sim$ 10 keV and $\sim$ 30 keV, respectively. For each set, the thermal conductance G is optimized to maintain electrothermal stability of the TES while biased. G is controlled via a perforated SiN_x membrane that supports the entire device (Figure 4.1(b)). In each set, there are three types of devices, with differing absorbers, from left to right: Au, Au/Evap-Bi and Au/Elp-Bi. Finally, there are four copies of each.

The G from the pixel to the heat bath was measured from the I-V curve as introduced in Section 7.1 at 85% normal resistance. It scaled with the perimeter of the TES plus the absorber (Tab. 4.1), as is expected in the case where the energy transport is dominated by specular reflections of phonons at the SiN_x surfaces. Next, the devices were characterized using an X-ray generator exciting fluorescence from several metallic foils. An aperture confined the X-ray illumination area of each device to the absorber. The device's total heat capacity C was calculated from the relationship $C = G \times \tau_{\mathrm{thermal}}$, where τ_{thermal} was approximated by the pulse-decay time τ at $T_{\mathrm{b}} \approx T_{\mathrm{c}}$, where the TES resistance dependence on temperature and current is small. The measured C values scaled with the absorber volumes only, and did not depend on the type of Bi used. Moreover, the contribution from the Bi was negligible, as shown in Tab. 4.1. This was to be expected

considering that the specific heat capacity of Bi is one order of magnitude smaller than that of Au. Because the energy resolution is proportional to $\sqrt{C}$, the Bi layer is not expected to introduce any energy resolution penalty.

4.2. Fabrication

For the Evap-Bi sample, an 80 nm gold (Au) layer, with a 5 nm titanium (Ti) adhesion underlayer, was e-beam evaporated on a silicon substrate consecutively, and then a 3 µm Bi layer was thermally evaporated in a separate chamber at a rate of 100 Å/s at room temperature. The wafer stage was water cooled in the Bi system and did not show noticeable temperature change during deposition. The 3 µm Elp-Bi layer was electrodeposited on a 1 µm Au seed layer on top of the silicon wafer [**58**]. The Bi plating rate was 283 nm/min with a current density of 6.0 mA/cm^2 DC and a bias voltage of 1.4 V; plating solution was at room temperature and not agitated.

4.3. Microstructure characterization

To characterize the Bi microstructure, we took a series of SEM images of the two types of Bi, examples of which are shown in Figure 4.2. The films present a very different appearance, with the Elp-Bi grains appearing significantly larger than those of the Evap-Bi, which was also reported in Ref. [**35**].

The SEM images show that the Elp-Bi sample has a very rough surface with grain size on the order of $\sim$ 1 µm. On the other hand, Evap-Bi shows a much finer surface, with grains that are on the order of $\sim$ 100 nm in size.

Although the differences in the two materials are quite evident from these images, a more quantitative analysis is needed to evaluate how the difference in microstructure

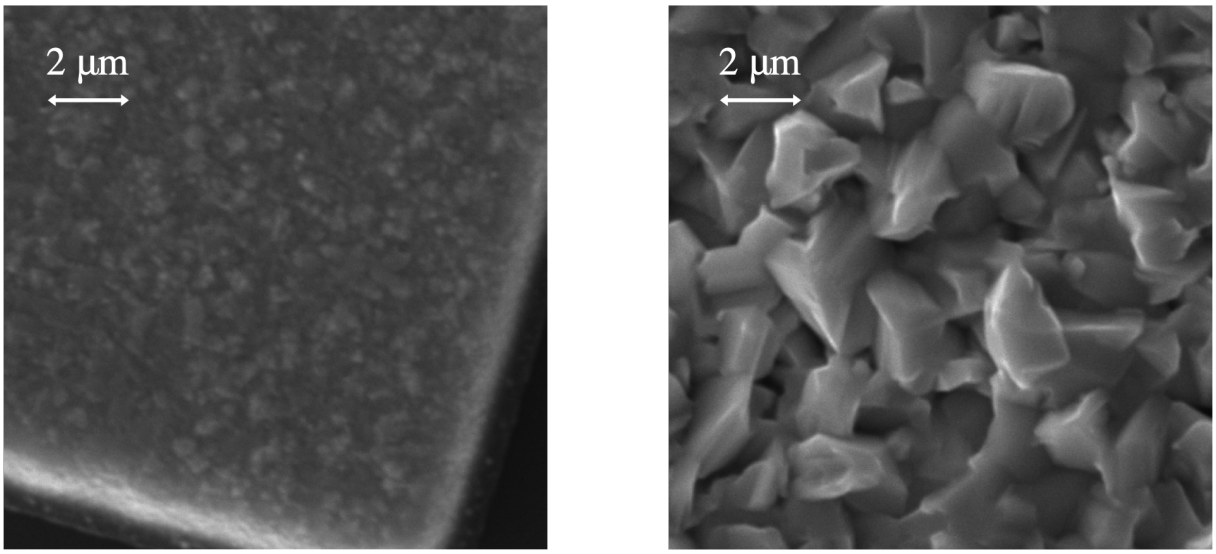

(a) (b)

Figure 4.2. SEM images of (a) thermally evaporated Bi, and (b) electroplated Bi. The images were taken under the same magnification. The electroplated sample clearly shows larger grains than the evaporated sample.

could influence the absorbers performances under X-ray illumination. We therefore characterized the films using high energy X-ray diffraction at the 1-ID-E beamline of the Advanced Photon Source, Argonne National Laboratory. Two measurement techniques were employed, as the two samples have very different microstructure. For the Elp-Bi sample, the far field high energy diffraction microscopy (FF-HEDM) technique was used. FF-HEDM is an extension of the rotating crystal method; diffraction spots from large coherent crystals in a polycrystalline sample like the Elp-Bi sample are recorded on an area detector as the sample is rotated with respect to the incident monochromatic X-ray beam. Based on the number of diffraction spots recorded for a particular family of crystallographic planes and the size of the illuminated volume, the average size of grains can be computed.

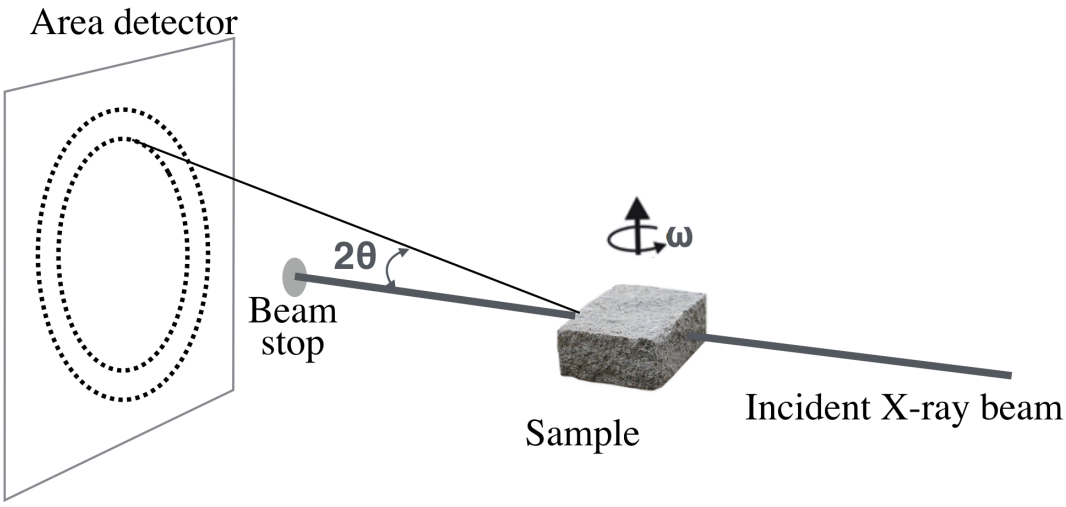

Figure 4.3. Far-field high-energy diffraction microscopy (FF-HEDM) setup. Transmission diffraction patterns were collected at each 0.25° step during the rotation in the plane normal direction $\boldsymbol{\omega}$.

Figure 4.3 illustrates the FF-HEDM setup used in this work. A monochromatic X-ray beam (energy $E = 80$ keV) was used. To minimize scattering from the substrate, the beam was vertically focused to 1 µm using a set of sawtooth lenses [**59**] and horizontally cut to 100 µm using a set of slits. The diffraction patterns were recorded on an amorphous-Si detector [**60**] placed $\sim$ 1 m from the sample. The sample was rotated along its plane normal direction by 360°, and diffraction patterns were recorded at each step of 0.25°.

For the Evap-Bi sample, the wide angle X-ray scattering (WAXS) technique was used. WAXS uses the same setup as the one used for FF-HEDM, and records powder diffraction patterns from small grains like the Evap-Bi sample on an area detector. For both FF-HEDM data (Elp-Bi) and WAXS data (Evap-Bi), the diffraction patterns matched the monoclinic Bi phase (symmetry group C2/m with lattice parameters a = 7.8873 Å, b = 4.5572 Å, c = 6.5836 Å, $\alpha = \gamma = 90°$, $\beta = 143°$) described by Shu *et al.* [**61**].

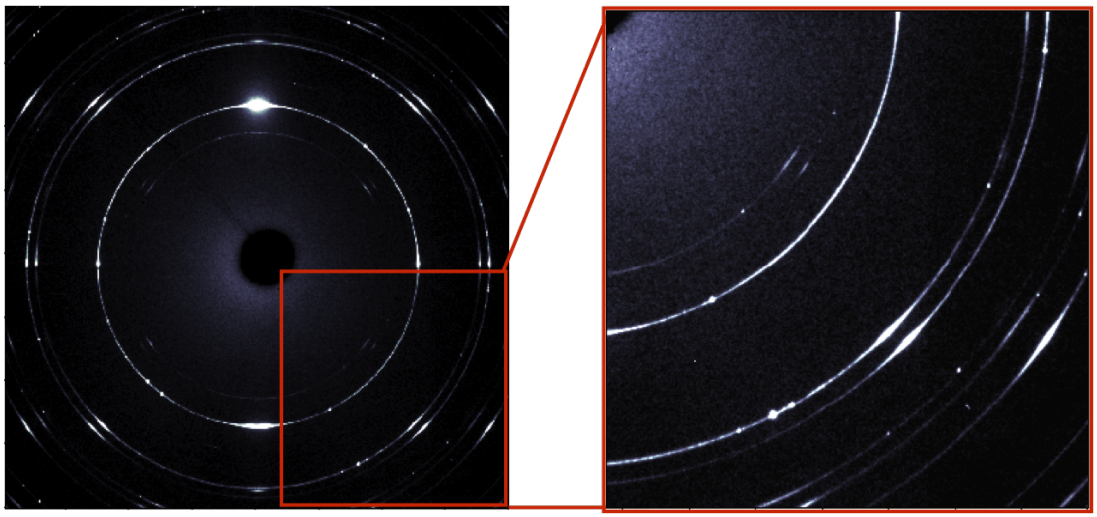

(a)

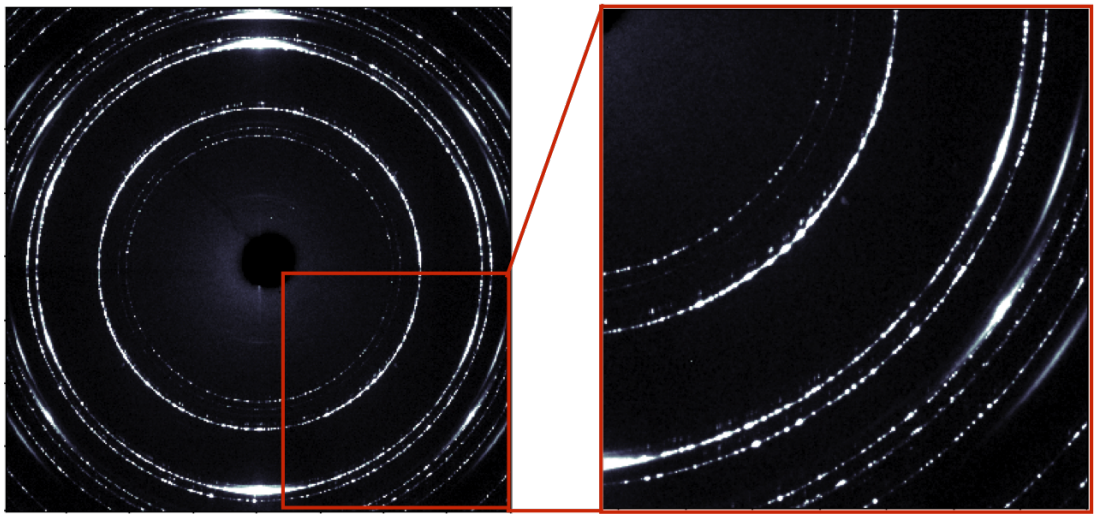

(b)

Figure 4.4. Example WAXS and FF-HEDM diffraction patterns for (a) Evap-Bi, and (b) Elp-Bi, respectively. The monoclinic Bi phase is the major constituent in both samples but the diffraction patterns are significantly different; the diffraction pattern from Evap-Bi is more continuous around the azimuth while that from Elp-Bi is spottier, indicating larger grain sizes for the latter sample.

The diffraction patterns from the Evap-Bi and Elp-Bi samples are shown in Figure 4.4a and Figure 4.4b, respectively. The setup in this study was not optimized for minor composition detection, and quantified impurity measurements would require explicit experiments

in the future. Within this limitation, however, we were able to see that for both samples the monoclinic phase of Bi is the major constituent, and their diffraction patterns show significant differences. The rings are continuous and their intensities are more uniform around the azimuth for the Evap-Bi sample (Figure 4.4a); the rings are spotty and the intensities vary significantly around the azimuth for Elp-Bi sample (Figure 4.4b). We attribute this observation to different grain sizes as indicated by the SEM images.

For the diffraction patterns from the Elp-Bi sample, the total number of diffraction spots for a particular family of crystallographic planes was determined using the appropriate spot searching algorithm [**62**]. Given the crystal plane family multiplicity, the total number of grains in the illuminated volume can be estimated and the average size of the constituent grains can be computed. Here, the diffraction spots associated with the {001} family of crystallographic planes (multiplicity of 2) were used. Assuming that the grains are spherical, the diameter of Bi grains in the Elp-Bi sample was approximately 1.4 µm.

For the diffraction patterns from the Evap-Bi sample, the peak widths and Scherrer equation $B = K\lambda/(L\cos\theta)$ are used to estimate the average size of the grains. In the Scherrer equation, B is the width of the diffraction peak obtained by fitting the diffraction peak with a pseudo-Voigt function, K is the shape factor (0.93), L is the average size of the grains, and θ is the Bragg angle associated with a particular diffraction peak. The average grain size in the Evap-Bi sample based on this approach is approximately 30 nm. In the raw diffraction pattern, the regions with bright diffraction spots emanating from the substrate were avoided.

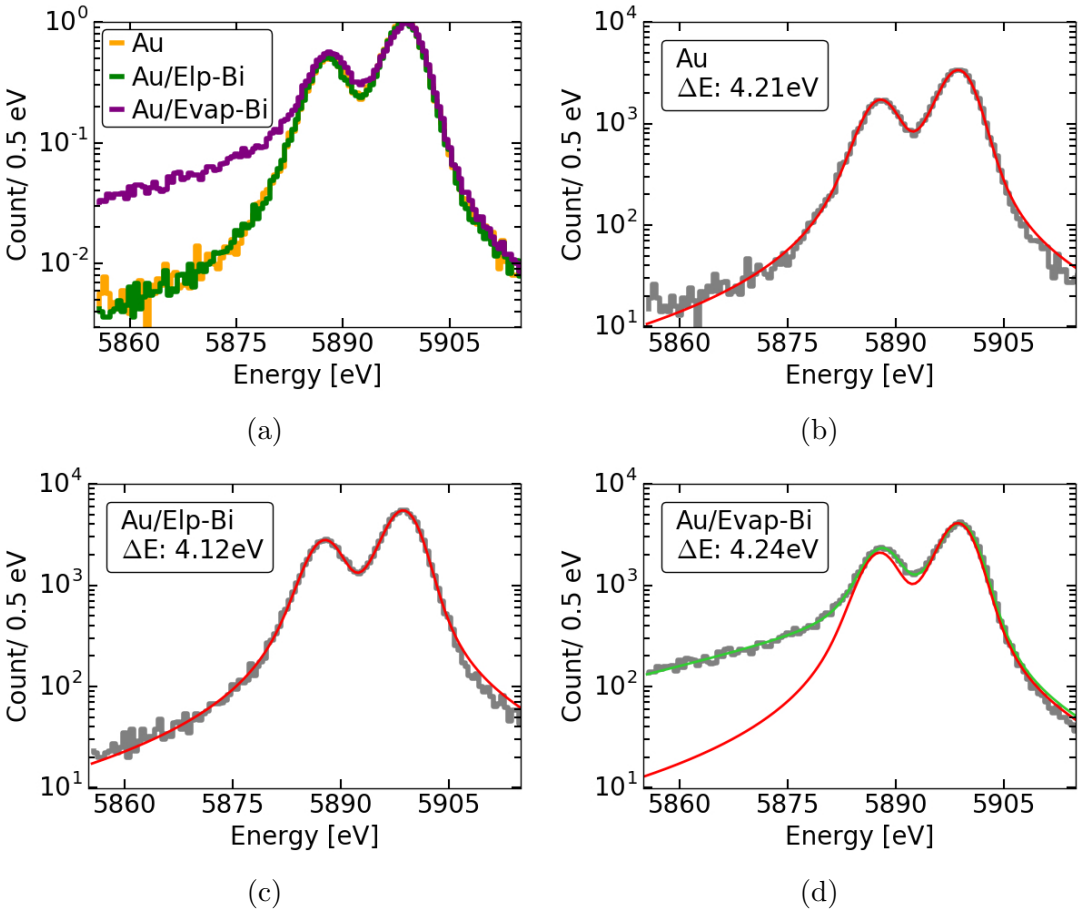

Figure 4.5. (a): Comparison of the Mn Kα spectrum measured by small pixels with the three types of absorbers (normalized at the peak maxima). The Au/Evap-Bi absorber devices show a LE tail compared with the Au and Au/Elp-Bi absorbers. (b) and (c): Measured spectra for Au and Au/Elp-Bi respectively (black) are well-matched to a Gaussian fit (red). (d): Measured spectrum from Au/Evap-Bi (black) is poorly matched by a simple Gaussian fit (red), while a Gaussian with tail fit (green) better approximates it.

4.4. X-ray spectra analysis

X-ray pulse heights (*i.e.*, energies) were estimated via optimal-filter-based techniques [**63**]. The Mn Kα spectra in Figure 4.5(a) measured by small Au and Au/Elp-Bi pixels are nearly identical, while the Au/Evap-Bi spectrum shows a clear LE tail. The spectra

from the three types of pixels show similar energy resolution, which is consistent with the heat capacity measurement. To further examine if a subtle LE tail exists in the Au and Au/Elp-Bi spectra, we fitted our observed spectra to a convolution of a Gaussian detector response function and the natural line shape, as previously measured by Hölzer *et al.* [**64**], represented by the red lines in Figs. 4.5(b)-(d). Both the Au and Au/Elp-Bi data match well with the Gaussian response function, indicating no presence of LE tails. Conversely, the simple Gaussian fit fails when applied to the Au/Evap-Bi spectrum. The LE tail in the Au/Evap-Bi spectrum can be fitted by the additional convolution of an exponential function with a Gaussian distribution (green line in Figure 4.5d), as suggested in Ref. [**55**]. In Figure 4.6, measurements of the LE tail fraction, which denotes the portion of energy deposited in the tail, from a small Au/Evap-Bi absorber for titanium (Ti), chromium (Cr), manganese (Mn), iron (Fe) and Cu Kα emissions are reported (a similar trend is observed in the large absorber). A clear increase in the LE tail fraction with X-ray energy is present; this has also been reported by Tatsuno *et al.* [**55**] and Fowler *et al.* [**65**].

4.5. Low-energy tail

The LE tail is indicative of some mechanism that prevents measurement of the full energy deposited in the absorber, with consequent generation of a current pulse that is smaller than expected. The missing energy either escapes from or is trapped within the Evap-Bi and not transformed into thermal energy over a time scale that is short compared to the TES typical response time ($\sim$ 1 ms). Typical energy-escape mechanisms are either emission of a fluorescence photon by the absorber, which does not get re-absorbed by it,

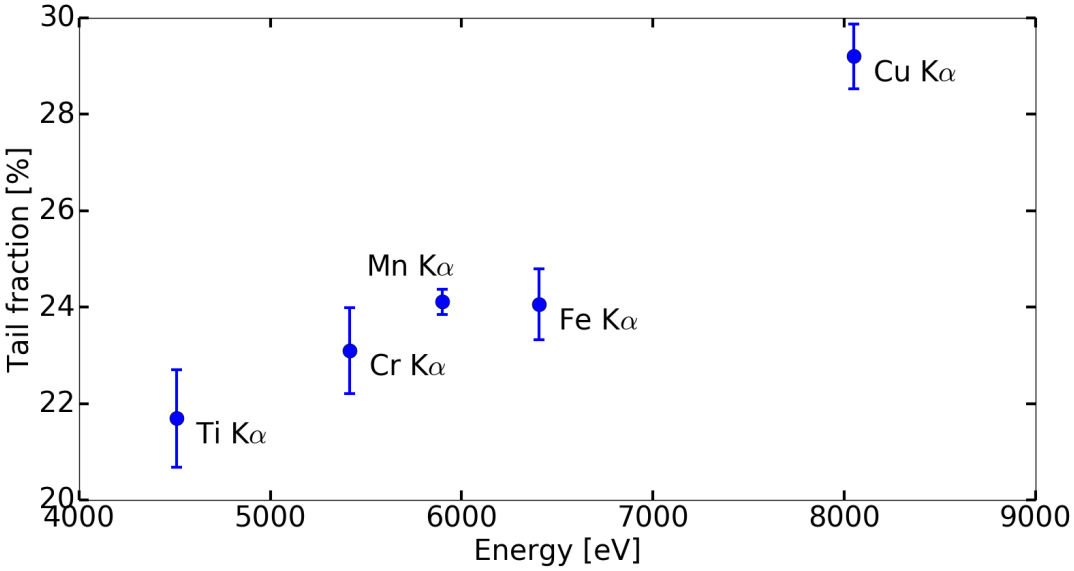

Figure 4.6. The LE-tail fraction of the Ti, Cr, Mn, Fe and Cu Kα lines for a small Au/Evap-Bi device. Error bars denote the fit standard deviation.

or escape of phonons or electrons, generated in the energy relaxation process, through the substrate or the surface to the ambient environment.

From the analysis of the LE-tail characteristic and its dependence on the incident photon energy, we can exclude the hypothesis of escape photons. The fluorescence photons emitted by Bi are at discrete energies (Mα at 2.423 keV and Mβ at 2.525 keV) [**65**], which is incompatible with the continuous distribution of the LE tail seen in the Evap-Bi spectrum. Moreover, the escape fluorescence mechanism would be inherent to Bi, regardless of the deposition technique. The loss of energy through the substrate is also unlikely because 1 µm of Au is sufficient to thermalize energetic phonons [**66**] from either type of absorber. In addition, the use of the SiN_x membrane greatly inhibits the escape of high-energy phonons; those that reach the membrane are likely to reflect off its surface and be reabsorbed by the Au or Au/Bi. Furthermore, Kilbourne *et al.* [**67**] report that

both devices with an evaporated Bi absorber in direct contact with the SiN_x membrane and with the Bi in contact only with the TES show the presence of the LE tail.

The electron photoemission is also unlikely to happen because the photon-absorption event occurs deep in the absorber: the average attenuation length for Bi at these energies is several µm. Moreover, the higher the energy of the incident photon the deeper the absorption is likely to happen, making the electron escape harder, which contradicts the increase of LE tail fraction with energy in Figure 4.6. Finally, the work functions for Au and Bi are comparable (Au $\sim$ 5 eV, Bi $\sim$ 4 eV), which would make the probability of a photoemission event quite similar in the two materials at these X-ray photon energies. Based on these considerations, energy-escape mechanisms are improbable.

In semimetal Bi, the dominant contributions to heat transport from different heat carriers change with temperature, and non-lattice contributions to the total thermal conductivity can be significant at very low temperatures ($\sim$ 100 mK) relevant to TES operation [**68**]. Our data on transport measurements for Evap-Bi show semiconductor-like behavior (*i.e.*, residual resistance ratio of 0.4) due to grain boundary scattering [**69**], in agreement with the measured grain size. This further reduces the non-lattice thermal conductivity due to scattering of heat carriers at the grain boundaries and crystal defects; charge carrier thermal conductivity scales inversely with resistivity. The larger number of grain boundaries in the Evap-Bi is likely to scatter or trap heat carriers, and the columnar structure may constrain the heat from transferring horizontally, causing difficulty in the thermalization of the entire absorber. Moreover, Doriese *et al.* [**22**] report that the LE tail fraction of the spectrum increases with thickness of the evaporated film. This supports the idea that the thermalization mechanism in these columnar films happens mainly in

the vertical direction. Therefore the further an event is from the underlying Au layer, the more probable is the heat trapping mechanism.

The Bi semimetal-to-semiconductor transition occurs when the energy shift due to quantum confinement raises the lowest electron sub-band to an energy higher than the uppermost hole sub-band [**70, 71**]. This transition happens for sizes below 50 nm, and the energy gap has been shown to depend on the grain size [**72, 73**]. If the nature of the grains in Evap-Bi is semiconductive, this could also trap the heat in the form of long-lived electrons excited above the semiconducting energy gap. Given the grain size of the Evap-Bi, we can relate the LE tail to this size-induced phase transition effect. It is also conceivable that bismuth oxide may be present at the grain boundaries. As an insulator, bismuth oxide could result in long-lived electron-hole pairs that behave like lost energy.

The dependence of the LE tail fraction on the incident photon energy seen in Figure 4.6, and other work [**22, 55**] support the hypothesis of a morphology-based energy trapping mechanism in the Evap-Bi. Figure 4.7 shows the size of the secondary electron (SE) cloud in bulk Bi as a function of incident photon energy computed using the formulation presented in Tabat *et al.* [**74**]. The Bi mean excitation energy (823 eV) was found in [**75**]. In particular, the size of the SE cloud generated by the incident photon in the Bi absorber is $\sim$ 60 nm at 6 keV [**76, 74**], which is comparable with the grain size of the Evap-Bi. Moreover, the size of the SE cloud in the absorber is proportional to the energy of the incident photon [**76**]. Consequently, the number of grains (and grain boundaries) affected by the SE cloud depends on the energy of the incident photon, therefore influencing the number of events characterized by an incomplete energy collection. In contrast, the nature of our Elp-Bi absorbers at these thicknesses is more similar to a classical metal

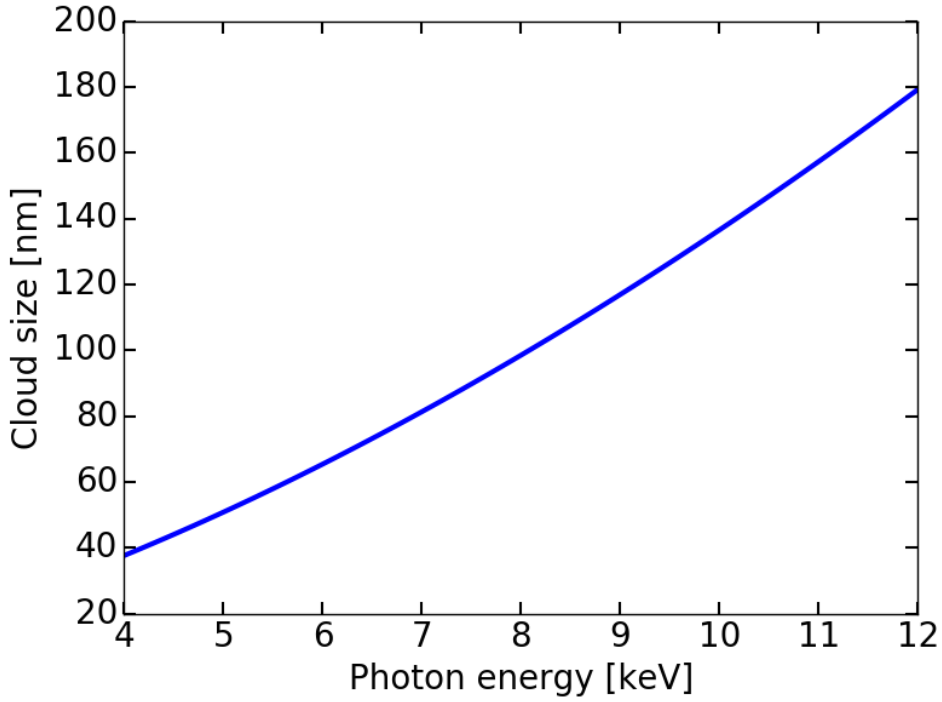

Figure 4.7. Secondary electron cloud size for bulk Bi as a function of incident photon energy. The mean excitation energy used for calculation was 823 eV.

with residual resistance ratio of the order of one [**58**] and thus immune from the LE tail phenomena.

4.6. Summary

In summary, we have fabricated Bi absorbers via thermal evaporation and electroplating, and characterized them with SEM and high energy X-ray diffraction measurements (WAXS and FF-HEDM). The SEM showed distinct grain sizes in the two absorbers. The high energy X-ray diffraction measurements confirmed this observation and allowed us to quantify the average grain size for both films: $\sim$ 30 nm for Evap-Bi and $\sim$ 1.4 µm for Elp-Bi. These results support the hypothesis that the different response under X-ray

illumination when used for TES microcalorimeters could be due to the very different microstructures of the two films. In particular, the average grain size seems to play a crucial role in the thermalization processes and consequent X-ray energy measurement. This study could be useful for future absorber designs in X-ray microcalorimeters including TESs which were used in this study, as well as metallic magnetic calorimeters (MMCs) and kinetic inductance detectors (KIDs).

CHAPTER 5

Microwave multipexing

5.1. Readout and multiplexing

As explained in Chapter 1, the TES exhibits excellent energy resolution. However, due to its small collecting area (usually ~ 0.1 mm^2 per pixel, whereas the silicon drift detector is ~ 40 mm^2 per pixel), and long dead time ($\sim$ ms), multiple sensors are often needed in one detector. In order to limit the number of wiring paths, their corresponding heat load and readout system complexity, the signals from multiple sensors are combined into a smaller number of channels. This scheme, called multiplexing, can be realized in several ways. Based on how the signal channels are assigned, the multiplexing schemes used for TES microcalorimeters include time-division multiplexing (TDM), code-division multiplexing (CDM), and frequency-division multiplexing (FDM) [**46**].

In TDM, the TESs are sampled in time sequences. For a channel that has N TESs, the effective sampling rate for an individual TES is $1/N$ times the measurement frequency. Due to Nyquist aliasing, the noise is increased by $\sqrt{N}$. To date, this multiplexing scheme is the most mature technique, and has achieved 200 kHz sampling rates [**77**]. The CDM samples TESs in a similar way as the TDM. However, the different sequences are not read out in a common time channel. Instead, they are read out in individual code channels. Therefore, in CDM, although the TES sampling frequency is decreased with multiplexing, it is the same as the measurement frequency, and there is no noise aliasing problem.

In FDM, the TESs are read out from different frequency tones, and this can be realized in two ways. One way is to bias the TES with an alternating voltage (AC) which has a distinct frequency, while the other way is to bias the TES with a direct voltage (DC) and mount it to a RF SQUID which is coupled to a microwave resonator that has a signature frequency. In this study, we adopt the microwave multiplexing scheme with RF SQUIDs.

5.2. Microwave frequency-division multiplexer

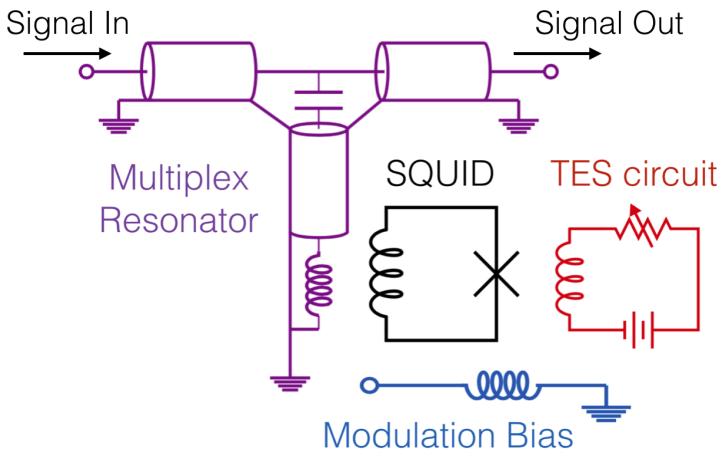

Figure 5.1. The schematic of a single channel from a multiplex TES.

In our system, the frequency coupling is realized by using multi-channel microwave resonators [**78**], and the TESs are connected to the frequency channels via RF SQUIDs as low-temperature amplifiers. Figure 5.1 shows one channel of this multiplexing scheme. The signal generated from photons hitting the TES is amplified by the SQUID, then detected by the resonator, and is read out as a transmission signal change through the microwave feed line. A flux-ramp modulation bias is applied to the SQUID to read out the signal properly, which will be introduced in Section 5.3.

5.2.1. Quarter-wave resonator

The resonator is a transmission line open on one end and shorted on the other end, so that it forms a quarter-wave resonator. The standing waves that can transmit through a quarter-wave resonator of lengh l must meet the condition

$$(2n+1)\frac{\lambda}{4} = l. \tag{5.1}$$

For a phase velocity of $\nu_{\rm p}$, the wave frequency of the first resonant mode is $f_1 = \nu_{\rm p}/4l$. We only use the first resonant mode in the multi-channel reading.

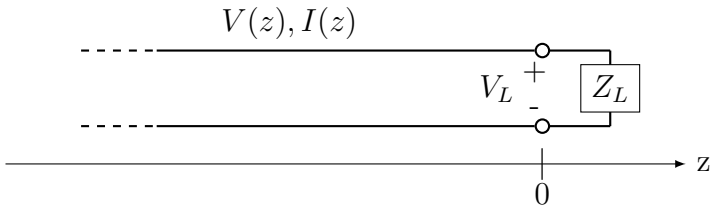

Figure 5.2. A transmission line terminated by a load impedance Z_L

Figure 5.2 shows the transmission lined terminated with a load impedance along the z direcion. The electromagnetic (EM) wave traveling in the line has the phase of

$$\theta = \omega\frac{z}{\nu_p} \equiv \beta z, \tag{5.2}$$

where ω is the EM wave frequency, and z is the position on the transmission line. The signal in the transimission line includes the incident and reflected wave, therefore the

voltage and current in the line can be described as ([**79**]):

$$V(z) = V_0^+ e^{-j\beta z} + V_0^- e^{j\beta z}, \tag{5.3}$$

$$\begin{aligned} I(z) &= I_0^+ e^{-j\beta z} + I_0^- e^{j\beta z} \\ &= \frac{V_0^+}{Z_0} e^{-j\beta z} - \frac{V_0^-}{Z_0} e^{j\beta z}, \end{aligned} \tag{5.4}$$

where V_0 and I_0 are the signal amplitudes, the superscript "+" means the incident direction, "-" means the reflecting direction, and Z_0 is the transmission line characteristic impedance. The load impedance is

$$Z_L = \frac{V(0)}{I(0)} = \frac{V_0^+ + V_0^-}{V_0^+ - V_0^-} Z_0, \tag{5.5}$$

which can be reorganized to give

$$\frac{V_0^-}{V_0^+} = \frac{Z_L - Z_0}{Z_L + Z_0}. \tag{5.6}$$

The input impedance of the transmission line at z is

$$\begin{aligned} Z_{in}(z) &= \frac{V(z)}{I(z)} \\ &= \frac{V_0^+ e^{-j\beta z} + V_0^- e^{j\beta z}}{V_0^+ e^{-j\beta z} - V_0^- e^{j\beta z}} Z_0 \\ &= \frac{(Z_L + Z_0)e^{-j\beta z} + (Z_L - Z_0)e^{j\beta z}}{(Z_L + Z_0)e^{-j\beta z} - (Z_L - Z_0)e^{j\beta z}} Z_0 \\ &= \frac{Z_L \cos(\beta z) - jZ_0 \sin(\beta z)}{Z_0 \cos(\beta z) - jZ_L \sin(\beta z)} Z_0 \\ &= \frac{Z_L - jZ_0 \tan(\beta z)}{Z_0 - jZ_L \tan(\beta z)} Z_0. \end{aligned} \tag{5.7}$$

At $z = -l$, the input impedance is

$$Z_{in} = \frac{Z_L + jZ_0 \tan(\frac{\omega l}{\nu_p})}{Z_0 + jZ_L \tan(\frac{\omega l}{\nu_p})} Z_0. \tag{5.8}$$

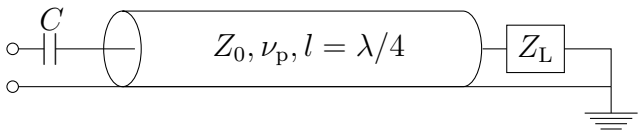

Figure 5.3. A quarter-wave resonator that has intrinsic impedance Z_0, load impedance Z_L and is coupled through a capacitance C to the microwave feedline.

The resonant frequency of the quarter-wave resonator is influenced by the input and output impedance. Figure 5.3 shows a resonator capacitively coupled to the feedline with a load impedance. In our device, the load impedance is an inductor screened by an RF SQUID, of which the effective impedance is L. So the input impedance of the device is

$$Z_{in} = \frac{j\omega L + jZ_0 \tan(\frac{\omega l}{\nu_p})}{Z_0 - \omega L \tan(\frac{\omega l}{\nu_p})} Z_0. \tag{5.9}$$

The capacitor is in series with the transmission line, so the total impedance is

$$Z_{total} = \frac{1}{j\omega C} + \frac{j\omega L + jZ_0 \tan(\frac{\omega l}{\nu_p})}{Z_0 - \omega L \tan(\frac{\omega l}{\nu_p})} Z_0. \tag{5.10}$$

At the resonant frequency, the effective total impedance of the transmission system is zero, so we have

$$0 = \frac{1}{j\omega_0 C} + \frac{j\omega_0 L + jZ_0 \tan(\frac{\omega_0 l}{\nu_p})}{Z_0 - \omega_0 L \tan(\frac{\omega_0 l}{\nu_p})} Z_0, \tag{5.11}$$

which leads to

$$0 = (\omega_0 C Z_0)[\omega_0 L \cot(\frac{\omega_0 l}{\nu_p}) + Z_0] - Z_0 \cot(\frac{\omega_0 l}{\nu_p}) + \omega_0 L. \tag{5.12}$$

For small deviations $\delta\omega_1 = \omega_0 - \omega_1$ ($\omega_1 = 2\pi f_1$), expanding the cotangent term around $\pi/2$ gives

$$\begin{aligned}
\cot(\frac{\omega_0 l}{\nu_p}) &= \cot(\frac{\pi}{2}\frac{\omega_0}{\omega_1}) \\
&= \cot(\frac{\pi}{2} + \frac{\pi}{2\omega_1}\delta\omega_1) \\
&= 0 - \frac{\pi}{2\omega_1}\delta\omega_1 + O(\delta\omega_1^2) \\
&\simeq -\frac{\pi}{2\omega_1}\delta\omega_1
\end{aligned} \tag{5.13}$$

and

$$\begin{aligned}
\omega_0^2 \cot(\frac{\omega_0 l}{\nu_p}) &\simeq (\omega_1 + \delta\omega_1)^2 \frac{\pi}{2\omega_1}\delta\omega_1 \\
&= \frac{\pi}{2}\omega_1\delta\omega_1 + O(\delta\omega_1^2) \\
&\simeq -\frac{\pi}{2}\omega_1\delta\omega_1.
\end{aligned} \tag{5.14}$$

Therefore, Equation (5.12) approximates to

$$0 = CLZ_0\frac{\pi}{2}\omega_1^2(1 - \frac{\omega_0}{\omega_1}) + \omega_0 C Z_0^2 - Z_0\frac{\pi}{2}(1 - \frac{\omega_0}{\omega_1}) + \omega_0 L. \tag{5.15}$$

which leads to

$$\frac{\omega_0}{\omega_1} = \frac{1 - \omega_1^2 LC}{1 + 2\omega_1 C Z_0/\pi + 2\omega_1 L/\pi Z_0}. \tag{5.16}$$

The coupling capacitor and load inductor are designed to satisfy $\frac{1}{\omega_1 C} \gg Z_0$ and $\omega_1 L \ll Z_0$, so $\omega_1^2 LC \ll 1$. The resonant frequency then is:

$$f_0 = \frac{f_1}{1 + 4f_1 C Z_0 + 4f_1 L/Z_0}. \tag{5.17}$$

Since L is a function of the SQUID phase ϕ, the resonant frequency of the system is also a function of ϕ.

5.2.2. Signal transmission

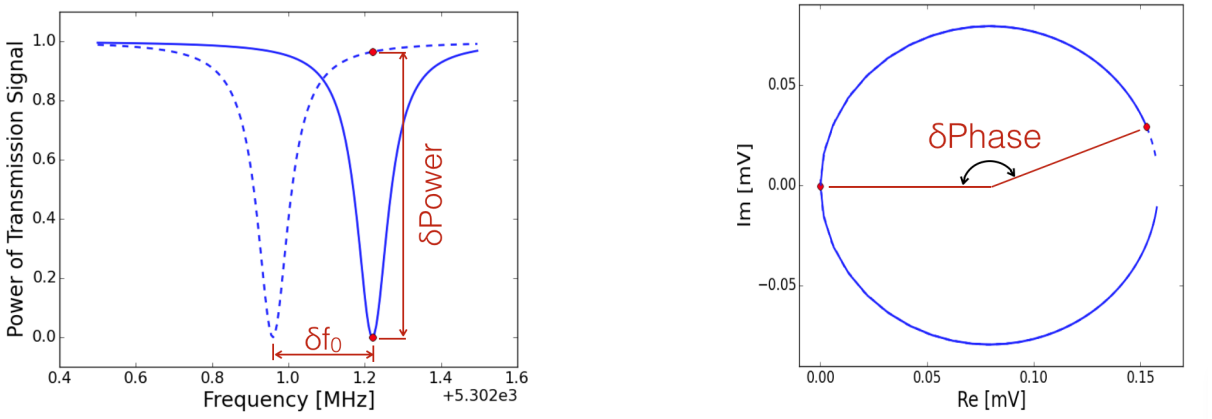

(a) (b)

Figure 5.4. Simulated S_{21} signal of a resonator channel with frequency scan. (a)The transmission signal magnitude. The solid line shows the resonance in the steady state, and the dotted line shows the resonance shifting. (b)The output signal shown in complex plane. During operation, a microwave signal at the resonant frequency is sent into the microwave feed line, and the TES signal change is measured at that frequency.

The measuring system can be seen as a two-port network. An RF signal goes into the system at port 1 and is read out at port 2. We measure the signal transmission as the

ratio of the output signal to the input signal. It can be described by [**80**]

$$S_{21} = 1 - \frac{\frac{Q_0}{Q_c} - 2iQ_0\frac{\Delta_f}{f_0}}{1 + 2iQ_0\frac{f-f_0}{f_0}}. \tag{5.18}$$

Figure 5.4 shows the simulated transmission signal through a quarter-wave resonator. In Figure 5.4a, at the resonant frequency f_0, the transmission signal shows a dip, since the power is absorbed by the resonator. When f_0 changes, the resonant dip also shifts. Figure 5.4b shows the same signal, but represented in the complex plane. The frequency scan traces out an incomplete circle. At a constant frequency, a change in f_0 will cause the resonant point to move along the circle, giving a phase change. Since f_0 is tuned by L as in Equation (5.17) and L changes with TES signal, the S_{21} change can be used to measure photon energy.

5.3. RF SQUID

An RF SQUID [**81**][**82**] is a superconducting loop interrupted by a weak link, which is called a *Josephson junction*. It can be used to measure very small current changes. As shown in Figure 5.1, it is placed between the resonator and the TES, and is modulated sinusoidally.

5.3.1. Josephson junction

The Josephson effect is the tunneling of Cooper pairs between two superconductors through a weak link. The weak link can be formed using insulators, normal metals, semiconductors, and narrow superconductors [**83**]. When two superconductors are well separated, their states are independent. When strongly linked (for example, connected

by a wide superconducting bridge), the state change of one superconductor will affect the other one. If weakly linked, Cooper pairs can tunnel through the barrier, but the wave functions of the two superconductors will not be perturbed.

By definition, a weak link preserves the periodicity of the wave functions of the two superconductors. If the phase in one of the superconductors is changed by 2π, the wave function and thus the supercurrent in the link does not change, leading to the first current-phase-relation (CPR) property of the link:

$$I_J(\phi) = I_J(\phi + 2\pi), \tag{5.19}$$

where I_J is the tunneling supercurrent, and ϕ is the phase difference accross the weak link. Under the time-reversal symmetry condition, changing the sign of the phase difference leads to the sign inverse of the tunneling current, which is the second property of the CPR relation:

$$I_J(\phi) = -I_J(-\phi). \tag{5.20}$$

With Equation (5.19) and (5.20), it is straightforward to derive

$$I_J(n\pi) = 0, n = 0, \pm 1, \pm 2, ... \tag{5.21}$$

Based on Equation (5.19) – (5.21), the tunneling supercurrent $I_J(\phi)$ can be written as a Fourier series [**84**]:

$$I_J(n\pi) = \sum_{n \geqslant 1} I_n \sin(n\phi) \tag{5.22}$$

where I_n is the amplitude of each of the sinusoidal components. In some materials, higher harmonic components ($n > 1$) can be dominant [**85, 86**]. Here we only discuss the $n = 1$

situation that

$$I_J(\phi) = I_c \sin\phi, \tag{5.23}$$

where I_c is the critical current.

The AC Josephson effect can be achieved by applying an external current larger than the critical current through the junction, or applying an AC current. With a fixed voltage V across the Josephson junction, the phase vary linearly with time:

$$\frac{d\phi}{dt} = \frac{2eV}{\hbar}, \tag{5.24}$$

where e is the elementary charge, and $\hbar$ is the Dirac constant.

A superconducting loop containing two Josephson junctions on each side of the external current supply line is a DC SQUID (Figure 5.5a); that with only one junction and no direct bias connection is a radio-frequency (RF) SQUID (Figure 5.5b).

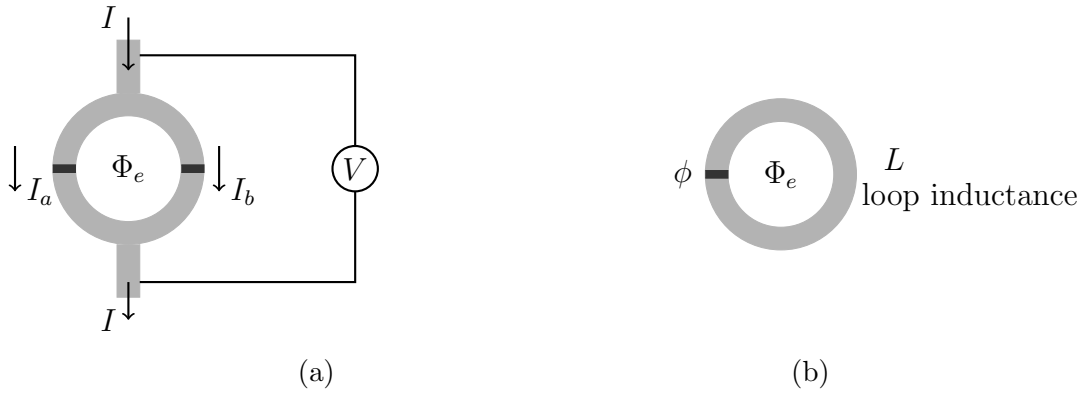

Figure 5.5. (a) DC SQUID and (b) RF SQUIDs. The gray loop represents the superconducting material. The black block is a weak link that connects the two sides of the superconductor, and can be made of insulators, normal metals, semiconductors, or narrow superconductors [**83**]. The phase difference ϕ across the Josephson junction evolves with the junction voltage, and is further related to the magnetic flux Φ through the circuit by Faraday's law, given by Equation (5.27).

With Faraday's law of induction, it is easy to deduce from Figure 5.5b that the voltage across the Josephson junction is:

$$V = -\frac{d\Phi}{dt}, \tag{5.25}$$

where Φ is the magnetic flux through the loop. Combined with Equation (5.24), the phase-flux relation can be obtained as:

$$\frac{d\phi}{dt} = \frac{2e}{\hbar}\frac{d\Phi}{dt}. \tag{5.26}$$

The sign of ϕ is reversed for a simpler expression, since which side of the junction is in a larger phase is not important. Finally the phase difference yields

$$\phi = \frac{2e}{\hbar}\Phi = 2\pi\frac{\Phi}{\Phi_0}, \tag{5.27}$$

where the initial value $\phi = 0$ at zero magnetic flux is ensured by the phase continuous condition. In this expression, $\Phi_0 = h/2e \sim 2 \times 10^{-15}$ Wb is the magnetic flux quantum. In a complete superconducting loop, the magnetic flux is quantized, being an integer multiple of Φ_0.

5.3.2. Josephson junction inductance

With the two Josephson relations, Equations (5.23) and (5.24), the change of current through the junction can be derived

$$\frac{dI}{dt} = I_c \cos(\phi)\frac{d\phi}{dt} \tag{5.28}$$

$$= I_c \cos(\phi)\frac{2eV}{\hbar}, \tag{5.29}$$

which is equivalent to

$$V = \frac{\hbar}{2eI_c}\sec(\phi)\frac{dI}{dt}, \tag{5.30}$$

from which the *Josephson inductance* is defined as

$$L_J(\phi) = L_J \sec(\phi), \tag{5.31}$$

where

$$L_J \equiv \frac{\hbar}{2eI_c} = \frac{\Phi_0}{2\pi I_c}. \tag{5.32}$$

The RF SQUID is a non-linear device, the inductance of which can be tuned by applying a magnetic flux. Our measurements of the current signal from a TES – which turns into a magnetic flux signal through inductance coupling – are based on this property.

5.3.3. Impedance measurement of RF SQUIDs

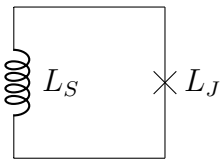

Figure 5.6. A RF SQUID with loop inductance L_S. The cross denotes the Josephson junction in the superconducting loop.

The SQUID's loop structure introduces a self inductance L_S (Figure 5.6), which makes the magnetic flux through the loop different from the external applied flux Φ_e:

$$\Phi_e = \Phi - I_c L_S \sin(2\pi\frac{\Phi}{\Phi_0}). \tag{5.33}$$

If one takes the derivative

$$\frac{d\Phi_e}{d\Phi} = 1 - \lambda \cos(2\pi \frac{\Phi}{\Phi_0}), \quad \lambda \equiv \frac{L_S}{L_J} \tag{5.34}$$

the single value property of Φ being a function of external magnetic flux Φ_e holds only when this derivative does not change sign, which requires that $\lambda < 1$.

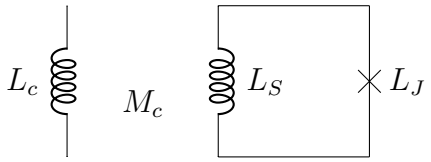

Figure 5.7. A RF SQUID coupled to an inductor L_c with mutual inductance M_c.

As introduced in Section 5.3.2, the RF SQUID can be used as a variable inductor. In our experiments, its inductance is measured by coupling it to the inductor of microwave resonators (Figure 5.7). The screening of the SQUID turns the resonator's inductor into a variable inductor, of which the actual inductance becomes

$$\begin{aligned} L(\Phi) &= L_c - \frac{M_c^2}{L_S + L_J \sec(2\pi\Phi/\Phi_0)} \\ &= L_c - \frac{M_c^2}{L_S} \frac{\lambda \cos(2\pi\Phi/\Phi_0)}{1 + \lambda \cos(2\pi\Phi/\Phi_0)}. \end{aligned} \tag{5.35}$$

5.3.4. SQUID modulation

Equation (5.35) indicates that the response of the SQUID is a periodic non-linear function. Bias is needed in order to keep the SQUID working in a responsive state. Taking the second derivative of Equation (5.35), the inductance change with respect to flux is

$$\frac{d^2 L(\phi)}{d\phi^2} = \frac{M_c^2}{L_S} \frac{2\lambda^2 + \lambda \cos(\phi) - \lambda^2 \cos(\phi)^2}{[1 + \lambda \cos(\phi)]^3}. \tag{5.36}$$

Setting this derivative to zero, one obtains

$$\cos(\phi) = \frac{1 - \sqrt{1 + 8\lambda^2}}{2\lambda}. \tag{5.37}$$

This value of flux is where the maximum change of the SQUID inductance happens.

However, biasing each SQUID separately requires lots of wires connecting to the mK detector chamber, which increases the wiring complexity, and makes it hard to maintain the detector's low temperature. Therefore, instead of biasing each SQUID with separate feedback loops, we use a single bias line to modulate all the SQUIDs, by turning the signal response to phase shifts [**87**].

A current scan can trace out the periodic response of the signal. When there is an additional signal, which means a current change added to the scanning current, the periodic response will have a phase shift. This current modulation method is called flux-ramp, and is shown in Figure 5.8. Compared with biasing the SQUID at the most sensitive point, counting all the data points in a period increases the SQUID noise by $\sqrt{2}$. Since the SQUID noise is kept far below the TES noise, this noise increase does not notably degrade the detector's final energy resolution.

The signal within a ramp cycle is windowed and a discrete Fourier transform is applied to give one phase data point, so the effective readout frequency of the device is the flux-ramp frequency f_{ramp}. Given the the number of periods in one ramp to be N, the carrier frequency f_{c} is $f_{\mathrm{c}} = N \times f_{\mathrm{ramp}}$. Due to the fact that the resonator has a finite response time, f_{c} is restricted. Therefore f_{ramp} and thus the readout speed are limited by the resonator response time.

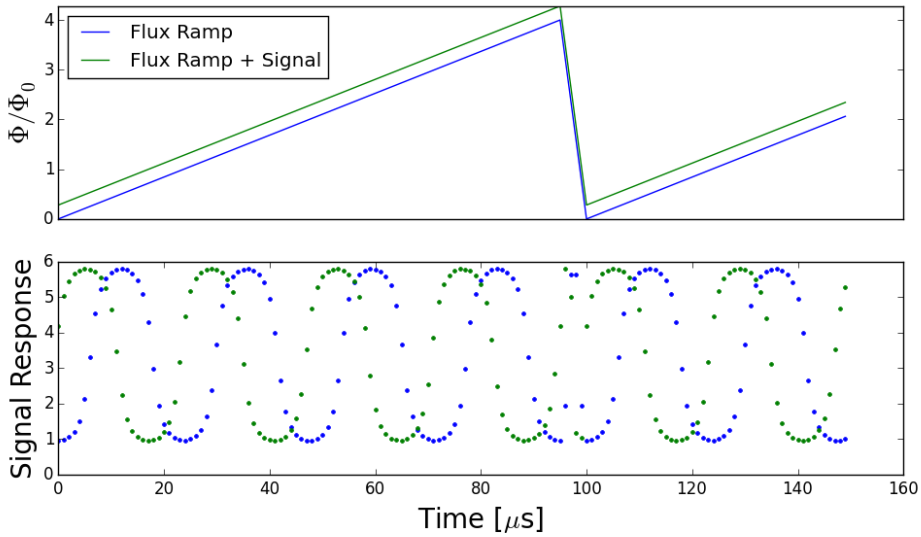

Figure 5.8. RF-SQUID modulation. The blue line in the upper panel shows a 10 kHz sawtooth ramp signal of 4 flux periods per cycle. This causes a 40 kHz periodic response of the system as the blue dots show in the lower window. When a current signal is applied in addition to the ramp signal as the green line shows, the whole SQUID oscillation exhibits a phase shift which can be calculated with discrete Fourier transform.

CHAPTER 6

Experimental setup

6.1. Cryostat

The TES usually operates at $\sim$ 100 mK, which is far beyond the cooling ability of liquid nigtrogen or helium. We use a two-stage cooling system with a pulse tube cryocooler and an adiabatic demagnetization refrigerator (ADR) which are commercially available from High Precision Devices, Inc.

In operation, the ADR is maintained at less than 10^{-5} torr vacuum using a turbo pump, so as to reduce heat transfer via air molecules. Inside the vacuum chamber, the cryo-stage was shielded in a decreasing temperature manner via metalic radiation-shields. The first layer is at room temperature; the second and third layers are cooled by the pulse tube cryocooler and are at 60 K and 4 K, respectively. On the 4 K stage sits the 4 T magnet which magnetizes and demagnetizes the ADR salt pills. Inside the 4 K layer are the two cold-fingers sticking from the ADR paramagnetic salt pills. One cold-finger is cooled to the TES operation temperature (50 $\sim$ 100 mK), and has the sample box attached to it; the other cold-finger is cooled to 1 K and has a copper screwing board attached, which is to pre-cool the biasing wires and cables coming from the 4 K stage before they reach the 50 mK sample stage. The sample box is magnetically shielded by a mu-metal cover.

When measuring X-rays, there has to be windows in the cryostat layers to let in photon flux. The outmost window is covered by beryllium to provide support for the vacuum. The windows of the inside thermal layers are covered with aluminum mylar foils to provide heat shielding. Figure 6.1 shows the side section view of the ADR [**88**].

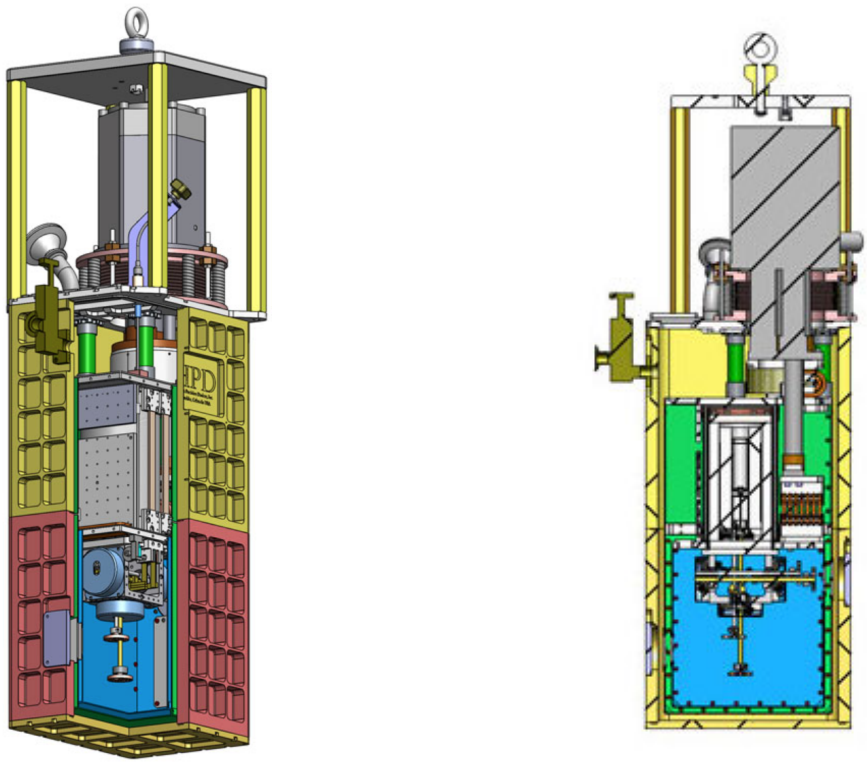

(a) (b)

Figure 6.1. ADR stage for TES measurement. (a) Corner view and (b) side section view of the ADR stage for TES measurements. In order to cool the system from room temperature to below 100 mK, several stages are used. The yellow layer provides vacuum. It consists of a thick stainless steel jacket, and a rigid beryllium window to let in X-rays in to the inside detector. The green layer is the 60 K stage, and the blue layer is the 4 K stage. The X-ray windows on these two layers use aluminum-coated mylar to screen thermal radiation from the warmer stage. Inside the 4 K stage are the 1 K and 50 mK cold fingers which are extended from the magnetic salt pills of the ADR. The detector is connected with the 50 mK cold finger. The microwave coaxial cables and bias lines run from the 50 mK detector stage to the 1 K cold finger, and through the consecutive stages to the room temperature electronics.

6.2. Electronics

As introduced in Section 5.2, we adopt the frequency-division multiplexing scheme. The detector is wired with the RF SQUID modulation lines, the TES DC bias lines, and the microwave coaxial cables. Device characterizations have been done with an IQ (in-phase and quadrature-phase) mixer, as well as a ROACH (Reconfigurable Open Architecture Computing Hardware) system.

6.2.1. IQ mixer

The IQ mixer is used to read the single frequency microwave signal. It multiplies the local oscillator (LO) signal with the radio frequency (RF) signal to be measured, and outputs the in-phase (I) and quadrature-phase (Q) component. Suppose the LO and RF signal are

$$S_{\mathrm{LO}} = V_{\mathrm{LO}} \sin(\omega_{\mathrm{LO}} t + \theta_{\mathrm{LO}}), \tag{6.1}$$

$$S_{\mathrm{RF}} = V_{\mathrm{RF}} \sin(\omega_{\mathrm{RF}} t + \theta_{\mathrm{RF}}), \tag{6.2}$$

respectively, where V is the amplitude, ω is the frequency, t is time, and θ is the phase. Their product gives

$$\begin{aligned} S_{out} &= V_{\mathrm{LO}} V_{\mathrm{RF}} \sin(\omega_{\mathrm{LO}} t + \theta_{\mathrm{LO}}) \sin(\omega_{\mathrm{RF}} t + \theta_{\mathrm{RF}}) \\ &= \frac{V_{\mathrm{LO}} V_{\mathrm{RF}}}{2} \{\cos[(\omega_{\mathrm{LO}} - \omega_{\mathrm{RF}})t + (\theta_{\mathrm{LO}} - \theta_{\mathrm{RF}})] - \cos[(\omega_{\mathrm{LO}} + \omega_{\mathrm{RF}})t + (\theta_{\mathrm{LO}} + \theta_{\mathrm{RF}})]\}. \end{aligned} \tag{6.3}$$

If the LO frequency is the same as the RF frequency, S_{out} will have a dc and a high frequency component. Applying a low pass filter, only the dc component is measured and

is called the in-phase (I) signal:

$$S_I = \frac{V_{\mathrm{LO}} V_{\mathrm{RF}}}{2} \cos(\theta_{\mathrm{LO}} - \theta_{\mathrm{RF}}). \tag{6.4}$$

Shifting the LO signal by 90°, a second output is generated and is called the quatrature-phase (Q) signal:

$$S_Q = \frac{V_{\mathrm{LO}} V_{\mathrm{RF}}}{2} \sin(\theta_{\mathrm{LO}} - \theta_{\mathrm{RF}}). \tag{6.5}$$

S_I and S_Q together give the amplitude and phase information of the RF signal.

Figure 6.2 shows the electrical configuration with the IQ mixer readout. A commercial signal generator is used to generate a microwave signal, which is split into two parts, each having half of the source power. One part goes into the detector's microwave resonator through a coaxial cable, picks up the response of a TES channel, and returns to the IQ mixer as the RF signal. The other part, as the LO signal, goes directly into the IQ mixer. The I/Q outputs go through low-pass filters and are sampled by a digitizer and saved in the computer.

6.2.2. ROACH

In this study, we used a *Reconfigurable Open Architecture Computing Hardware (ROACH)* board to process multi-frequency microwave signals [**89**]. The ROACH system is based on IQ-modulation, which is introduced in Section 6.2.1. It generates several frequency tones, sends them to the microwave multiplexer, and reads out the output microwave signal. The goal of the ROACH system is to read out all microwave-multiplexed TESs simutaneously while not degrading the energy resolution of individual TES pixels.

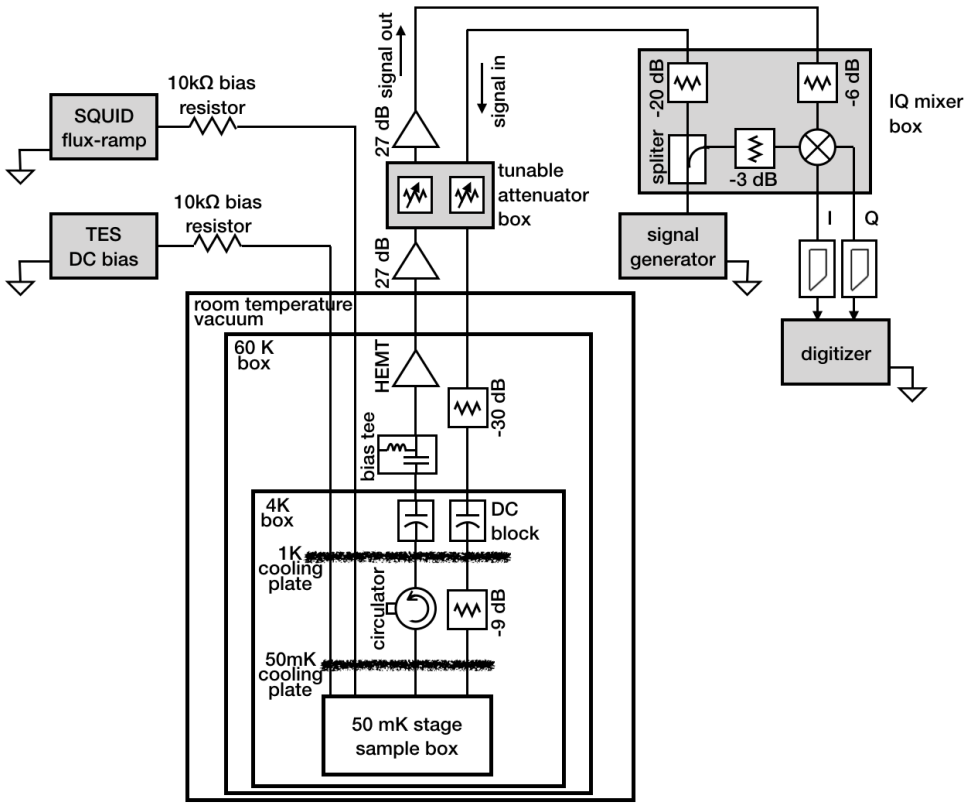

Figure 6.2. TES electronics set-up with IQ mixer readout. The sample box is placed at the 50 mK cold stage. Two coaxials cables are used to send in and out the microwave signal through the microwave multiplexer. Attenuators and amplifiers, including a high electron-mobility transistor (HEMT), are used to tune the signal power. DC blocks are used to filter low frequency noise. A circulator is used to remove the signal reflection. A bias tee is used to better cool down the coaxial cable. Although appearing here in the 60 K layer, the bias tee and HEMT are clamped onto the cooling plate that is connected to the 4 K environment; therefore they are also at 4K. A sawtooth signal generator in combination with a 10 kΩ resistor supplies the flux-ramp signal for the RF SQUIDs. A DC voltage source in combination with a 10 kΩ resistor supplies the bias signal for the TESs.

6.2.3. Attenuation and amplification

As will be introduced in Section 7.3, the optimal operation power of the microwave resonator is ~ -73 dBm at the cryogenic stage. In order to stand out from the thermal noise,

the room temperature source signal power is much larger than that. To reach -73 dBm at the microwave resonator at 50 mK, along the input coaxial cable, several attenuators are used.

The output signal has to be amplified to reach the operation power of the IQ mixer. Therefore, on the output side of the coaxial cable several amplifiers are used. The cold stage amplificaion is done with a high electron-mobility transistor (HEMT) at the 4 K stage. The HEMT is an active device and generates heat. To provide extra cooling a bias tee is used between the HEMT and the 4 K stage.

DC blocks are used to break the ground loop, so that the signal loop does not pick up low-frequency noise. A circulator is used after the sample box to avoid microwave signal reflection. The configuration is shown in Figure 6.2.

6.3. Detector assembly

As mentioned in Chapter 3, the entire detector consists of microwave resonators, RF SQUIDs, and TESs. The resonators and the SQUIDs are on one chip, and the TESs are on a separate chip. The parallel shunt resistors and series inductors are on a third chip (bias transition board). The resonator & SQUID chip, and the bias transition board are glued to the sample box using rubber cement. The TES chip needs to have good thermal contact with the cold stage; therefore it is tightly clamped to the sample box using screws and tiny copper fingers. We also use ultrasonic wirebonding to connect gold wires from the TES and collimator wafers to the sample box to improve the thermal contact. The three chips need to be connected with aluminum wirebonds (aluminum is superconducting under 1.2

K), as shown in Figure 6.3. For better grounding, the resonator chip is wire-bonded to the sample box along the edges.

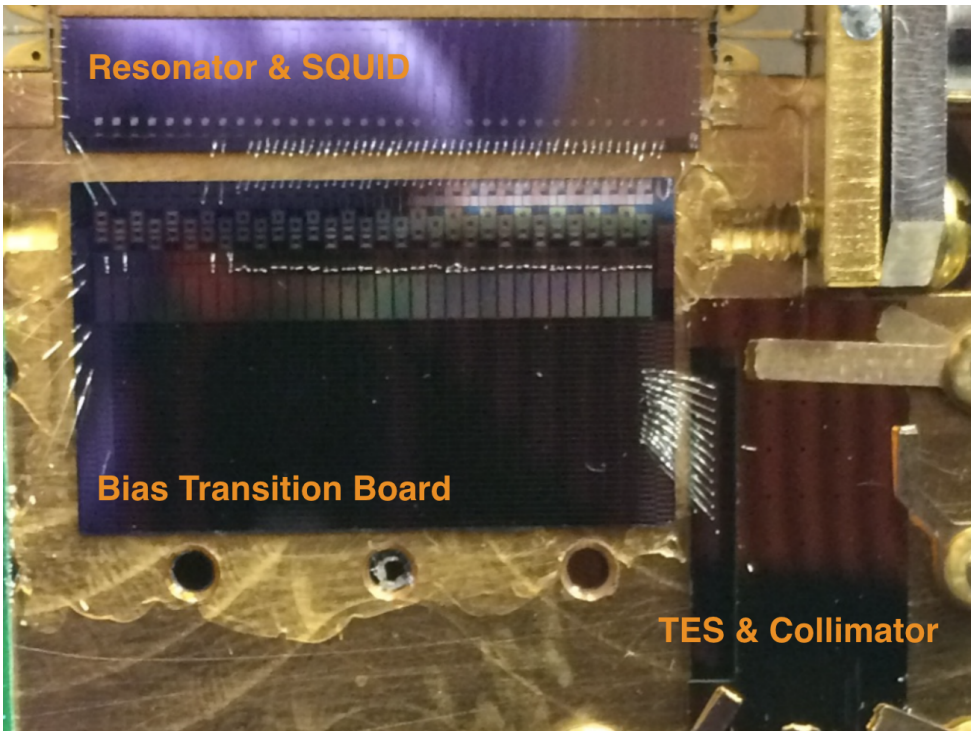

Figure 6.3. Picture of the assembled TES. The TES chip is covered by a collimator wafer to let the X ray hit the TES sensor only.

6.4. SQUID measurement

In order to set the SQUID modulation signal, one has to know its current-phase coupling factor. Since the SQUID phase cannot be directly measured, one can look at the resonant frequency f_0 to find the relative phase change. Figure 6.4 shows one resonator channel's f_0 as a function of DC bias current I change through the flux-ramp modulation

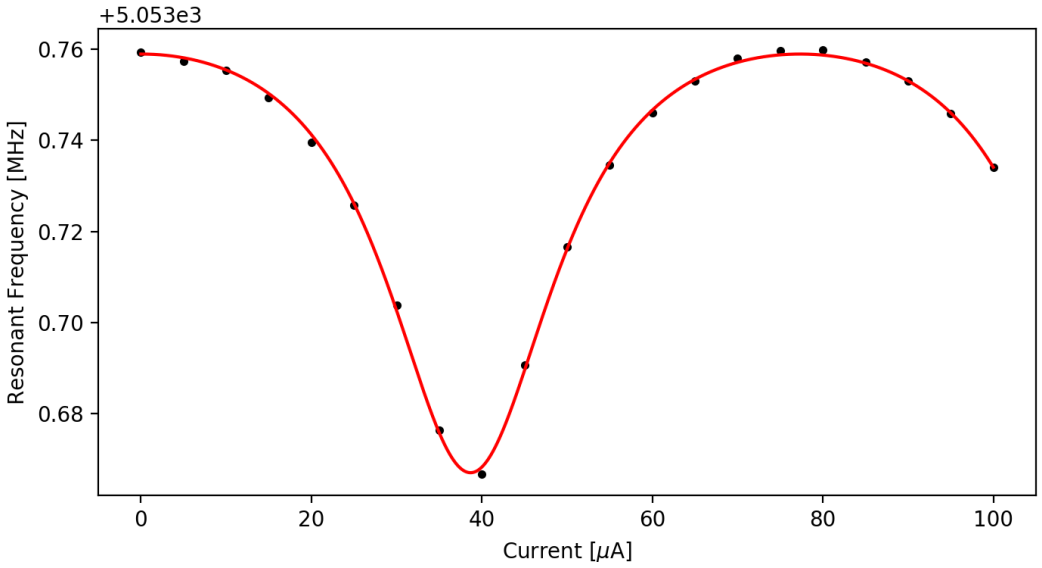

Figure 6.4. Measurement of the SQUID modulation current period. The fitted I_{period} is 77.3 µA.

line. Combining Equation (5.17) and (5.35), the $f_0 - I$ relation can be fitted by

$$\frac{1}{f_0} = a - b\frac{\cos(2\pi I/I_{\text{period}} + \theta_0)}{1 + \lambda\cos(2\pi I/I_{\text{period}} + \theta_0)}, \tag{6.6}$$

where the simplified parameters are

$$a = \frac{1}{f_1} + 4CZ_0 + \frac{4L_c}{Z_0}, \quad b = \frac{4M_c^2\lambda}{L_s Z_0}, \tag{6.7}$$

and θ_0 is the initial phase of the SQUID which comes from the residual magnetic flux in the SQUID loop. I_{period} is the parameter we need to find, which is the amount of current that causes 1 Φ_0 change in the SQUID. When modulating the SQUID, the amplitude of the flux-ramp current signal should be an integer multiple of I_{period}.

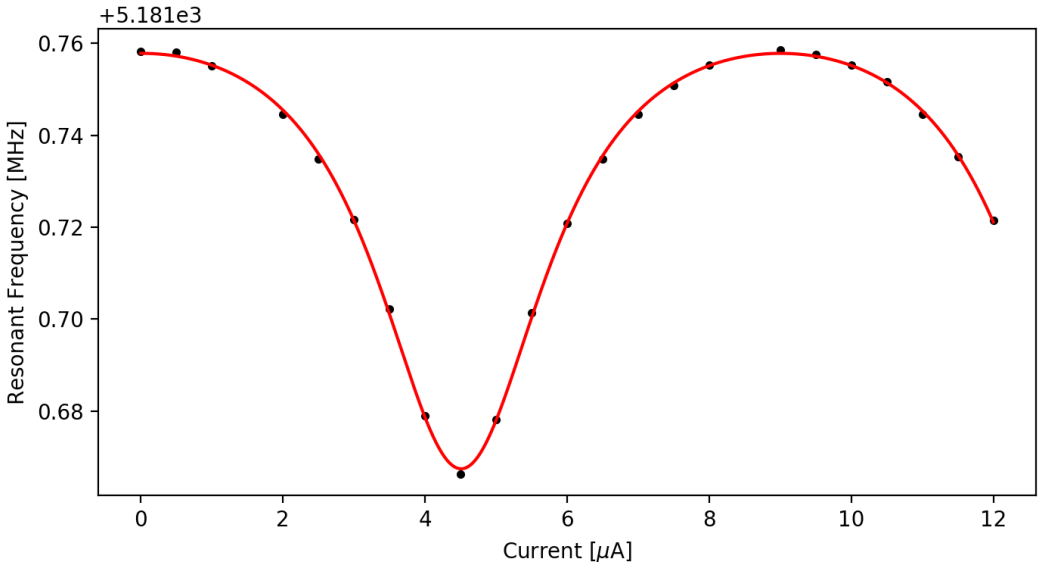

Figure 6.5. The resonant frequency modulated by the current via the TES-SQUID coupling. $I_{\text{period}} = 9.0$ µA

6.5. TES-SQUID coupling measurement

The TES signal measured through the flux-ramp modulated SQUID is in the unit of Φ_0. In order to know the exact current value, one needs to know the magnetic coupling factor between the TES and the SQUID. Alternatively, one can measure the experimental value I_{period} of the TES to SQUID coupling to scale the magnetic flux unit into current unit. This is done by connecting a DC bias source to the TES load circuit, and measuring the resonator's f_0 change while changing the DC current in the same way as in Section 6.4. The measured data and their fit are shown in Figure 6.5.

CHAPTER 7

Detector characterization

7.1. I-V measurement

The TES current-voltage (I-V) curve can reveal several thermal and electrical parameters. As described in Section 2.1, an operating TES is both thermally and electrically biased. In the equilibrium state, the Joule heating power produced by the TES and the heat bath cooling power are equal:

$$P_J = P_{\text{bath}}, \tag{7.1}$$

which after combining with Equations (2.14), (2.15) becomes

$$V \cdot I = \frac{G}{nT^{n-1}}(T^n - T_b^n) \tag{7.2}$$

where T is the TES temperature, and G is the thermal conductance between the TES and the heat bath at this temperature. When changing the bias voltage, the TES current will behave as in Figure 7.1, which can be analyzed in three parts.

When the TES is in the superconducting state, it has zero resistance and voltage. The $I - V$ curve will be a vertical line that extends from the origin to I_c. The Joule heating power P_J is zero. From equation (7.2) we can see that the TES temperature equals T_b. The $I - V$ curve in this region gives the I_c value.

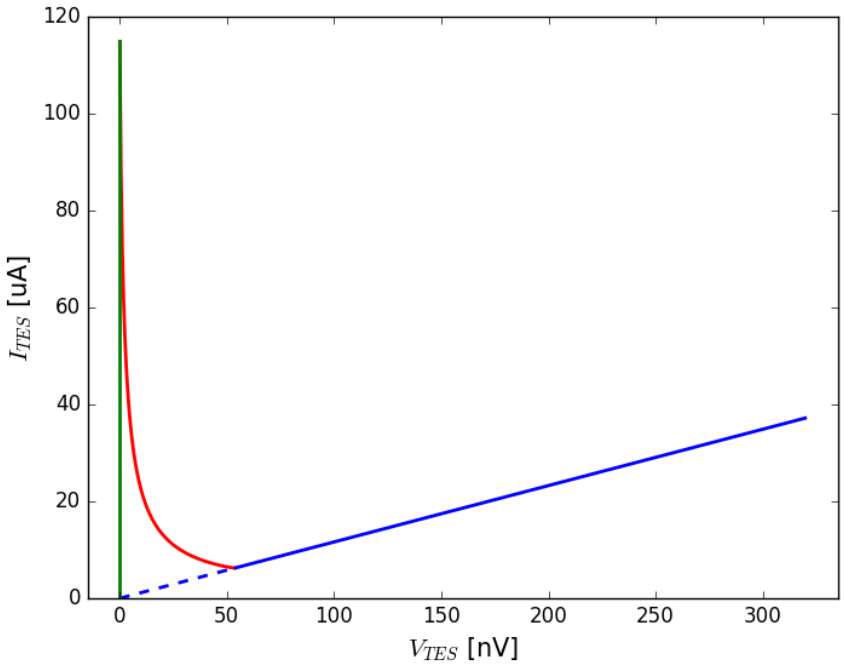

Figure 7.1. Simulated $I-V$ curve of a TES. The green vertical line shows the superconducting region. The blue straight line shows when the TES is normal. It extends to origin, and the inverse of its slope is R_n. The red line shows the transition region, in which the TES is biased for operation.

In the normal state, the TES becomes a pure resistor with value R_n. The $I-V$ curve will be a straight line with a slope of $1/R_n$ which extends through the origin. The TES temperature is beyond its critical temperature T_c. The $I-V$ curve in this region gives the R_n value.

Between the superconducting and normal state, the TES is in the transition state. Its temperature is around T_c, so the power flowing to the heat bath is almost constant, as is the Joule power. Therefore the $I-V$ curve in this region is nearly a reciprocal function. Equation (7.2) becomes

$$V \cdot I = \frac{G}{nT_c^{n-1}}(T_c^n - T_b^n). \tag{7.3}$$

Measuring the $I-V$ curve at different bath temperatures, with equation (7.2) we can fit for $G(T_c)$, T_c and n. T_c can also be measured directly from the $I-V$ curve. It is the temperature where the superconducting branch disappears.

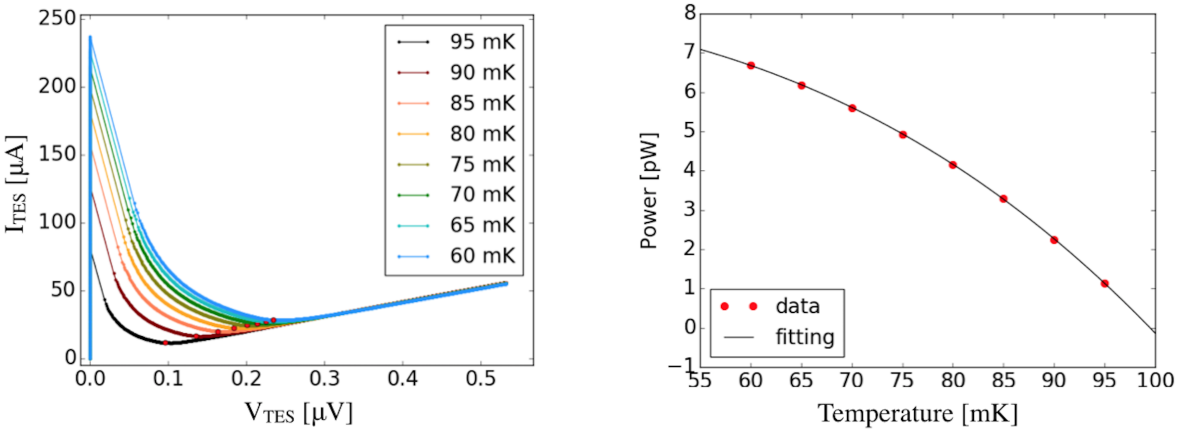

(a) (b)

Figure 7.2. TES $I-V$ characterization. (a) $I-V$ curve of a TES measured from 60 mK to 95 mK. The different bath temperatures are represented by different colors. The red dots are data at 80% R_n. They are used to calculate the Joule heating power. (b) Joule power of the TES at different bath temperatures calculated from (a). The red dots are the measured data, and the black line is the fitting with Equation (7.3). This measurement gives $R_n = 9.6$ mΩ, $G_c = 265$ pW/K, $n = 3.14$, and $T_c = 99.5$ mK.

Figure 7.2a shows the $I-V$ data of our TES. It is measured for different bath temperatures. The I and V data at the 80% transition point (the black dots) were used to calculate the Joule power and fit G_c, T_c and n (Figure 7.2b).

As shown in Figure 7.2a, between the transition and the superconducting region, there is a discontinuous region. This problem is essentially due to the TES's electrical circuit configuration. Recalling Figure 2.3a, the TES current I is measured from the SQUID readout channel. The TES voltage V, however, cannot be directly measured, and what

is measured is the external bias voltage V_{bias}. These two values are related by

$$V_{\text{bias}} = (V/R_{sh} + I) \cdot R_{\text{bias}}. \tag{7.4}$$

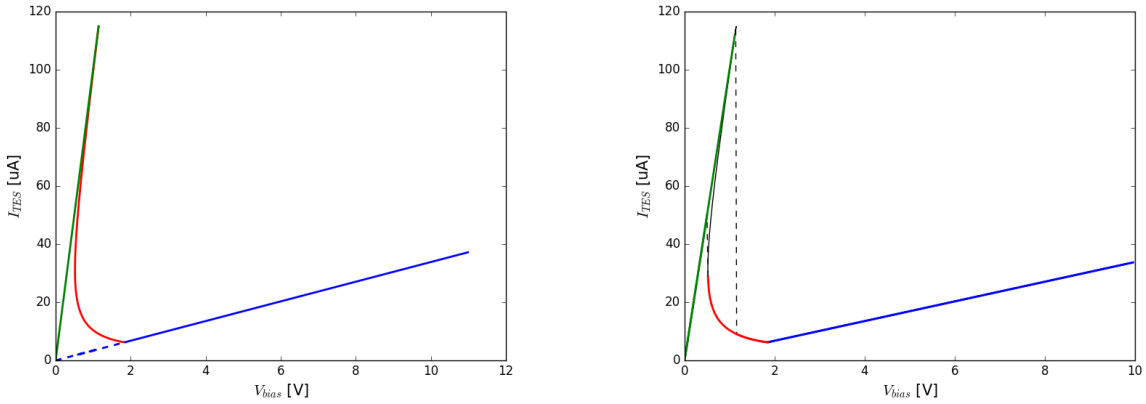

(a) (b)

Figure 7.3. Simulations of the $I - V_{\text{bias}}$ curve. (a) During experiments, V_{bias} is measured instead of V. Compared with the $I - V$ curve, the $I - V_{\text{bias}}$ curve slants to the right, which leads to hysteresis when ramping up and down V_{bias}. (b) The dashed lines show the two phase jump edges. The solid black line cannot be traced out due to the slant, and is what is missing in the converted $I - V$ curve.

As a result, compared with the $I - V$ curve shown in Figure 7.1, the directly measured $I - V_{\text{bias}}$ curve slants towards the right, as shown in Figure 7.3a. In the experiment, we change V_{bias} and measure I. This leads to the jump in the traced out $I - V_{\text{bias}}$ curve as shown in Figure 7.3b. Decreasing the bias voltage, the TES data will move along the normal line and continue into the transition region till its leftmost point. As the voltage continues to decrease, the TES will jump to the superconducting region and move on. Inversely, if one ramps up the bias voltage from zero, the TES will move along the superconducting line to its rightmost point I_c, and then jump down to the transition

or the normal branch. After converting the plot into the $I-V$ plot, discontinuity will appear in the jump region, and the $I-V$ curve will show hysterisis. Due to this hysteresis effect, if one needs more of the transition region data, the measurement should be taken by ramping down the bias voltage; if one wants to know the critical current I_c, the bias voltage should be ramped up.

In summary, the TES $I-V$ measurement gives several parameters: the critical temperature T_c, the critial current I_c, the normal resistance R_n, the thermal conductance between the TES and the heat sink G, and the thermal conducting index n. The optimal bias condition of a TES is determined based on these parameters.

7.2. Pulse decay measurement

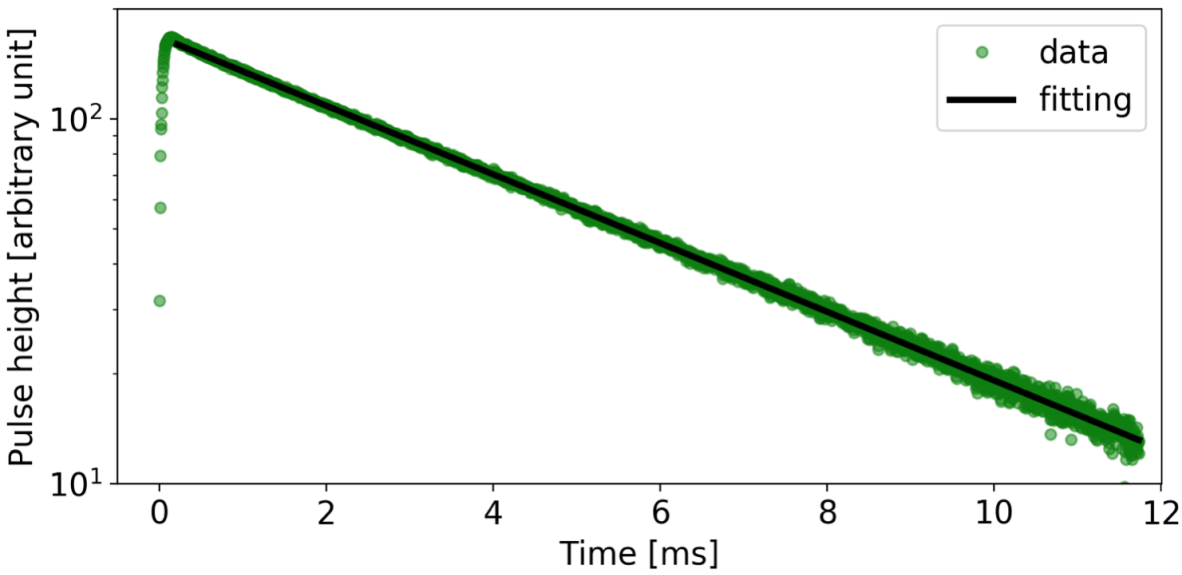

Figure 7.4. Pulse measured at $T_b \approx T_c$ (green dots). The decay time is fitted by an exponential function (black line).

When the TES is biased at a bath tempearture $T_b \approx T_c$, the TES resistance dependences on temperature and current (α_I and β) are small. Under this condition, recalling Equations (2.21), (2.22), (2.24), and (2.30), the pulse decay time can be approximated by $\tau = C/G$. Given G calculated from the $I - V$ measurement as introduced in Section 7.1, and τ fitted from the pulse exponential decay, the TES heat capacity C can be calculated. Figure 7.4 shows the average pulse measured at a high bias temperature. The decay time is fitted by an exponential function to be 4.61 ms. With G measured to be 265 pW/K, the TES heat capacity is calculated to be 1.22 pJ/K.

7.3. Noise measurement

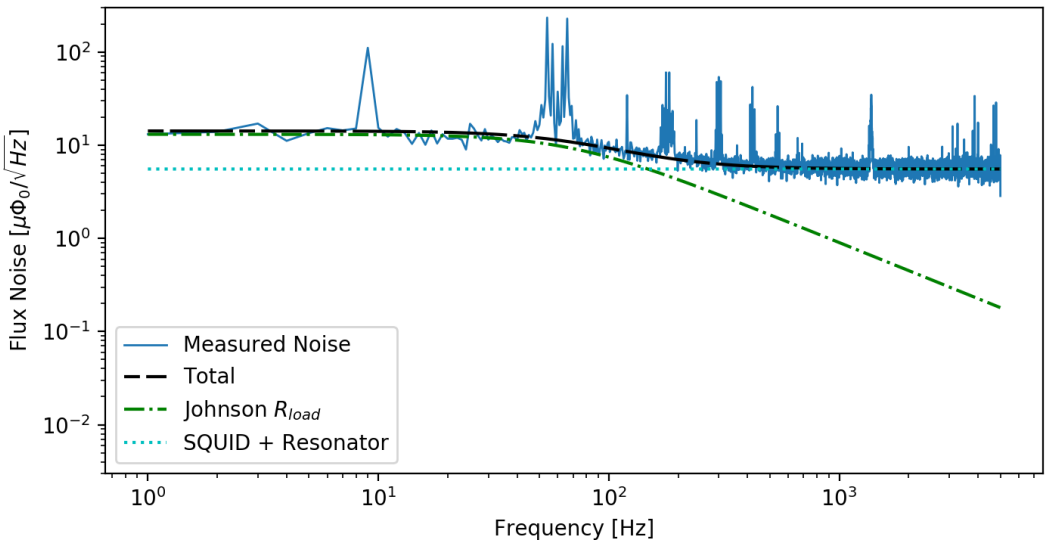

Figure 7.5. Noise spectrum of the detector at zero bias. The blue spectrum is the measured data, and the dashed lines are theoretical noise. The main noise sources are the load resistor's Johnson noise (green line), and the SQUID noise (light blue line).

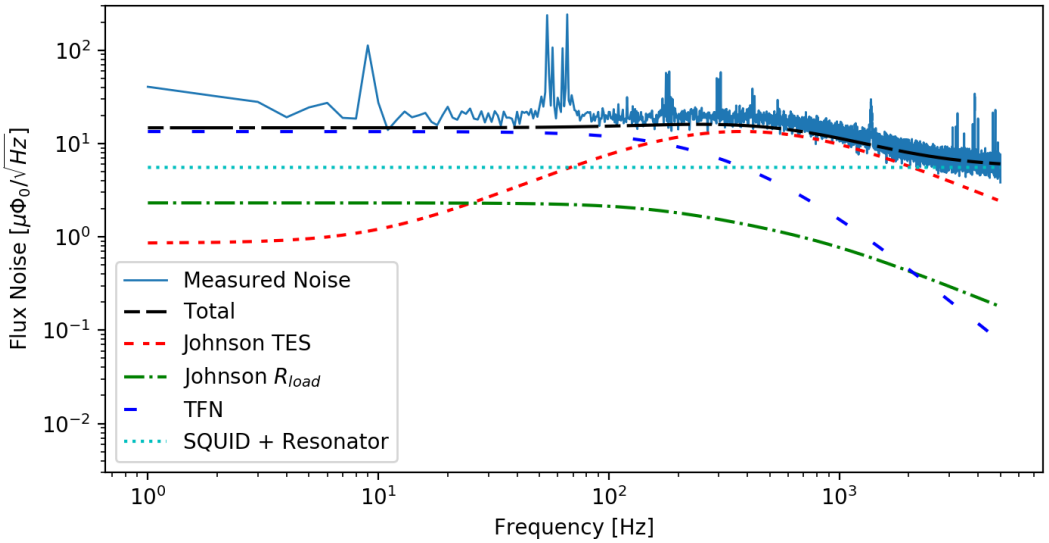

Figure 7.6. Noise spectrum of the detector at 20% bias and the theoretical calculation. When the SQUID and resonator noise is low enough, in the low frequency regime, the noise is mainly determined by the TES Johnson noise (red line) and thermal fluctuation noise (dark blue line). A simulated noise spectrum of TES that has a long absorber is given by Figure 3.4.

The noise is measured in various configurations in order to find the optimal operation condition. The main noise sources considered in our TES microcalorimeter are the Johnson noise of the load resistors, the Johnson noise of the TES, thermal noise due to the photon number fluctuation via the thermal link between the TES and the heat bath, SQUID noise, and the noise in the microwave resonators. The SQUID noise and resonator noise are not distinguishable in our measurement system, and therefore are treated together. Figures 7.5 and 7.6 show the noise spectra of the TES under zero bias and 20% normal resistance bias, respectively.

The noise level decides the detector energy resolution by

$$\Delta E = \int_{-\infty}^{\infty} \frac{df}{\mathrm{NEP}(f)}, \tag{7.5}$$

where $\mathrm{NEP}(f)$ is the noise equivalent power, defined as the ratio of the noise $n(f)$ and signal $s(f)$ in the frequency domain:

$$\mathrm{NEP}(f) = n(f)/s(f). \tag{7.6}$$

Equation (7.5) differs from the commonly used expression

$$\Delta E = \int_{0}^{\infty} \frac{4df}{\mathrm{NEP}(f)}, \tag{7.7}$$

as could be seen in Ref. [**90**][**43**]. In our case, we use the integration range of $-\infty$ to $+\infty$ instead of 0 to $+\infty$, giving a factor of 2. In addition, the noise $n(f)$ is two-sided noise intead of one-sided noise while using the Fourier transform to convert the time stream noise into the frequency domain, which gives another factor of 2. It is important to keep the definition and calculation consistent, especially because the Fourier transform is used extensively in this study.

7.3.1. Signal power

As shown in Figure 7.7, the SQUID flux-ramp response increases at smaller microwave signal power, which means better amplification, and therefore larger signal-to-noise ratio. However, under smaller signal power, the resonator noise increases as well [**91**]. To find the operation power that causes the smallest system noise, one needs to measure the noise

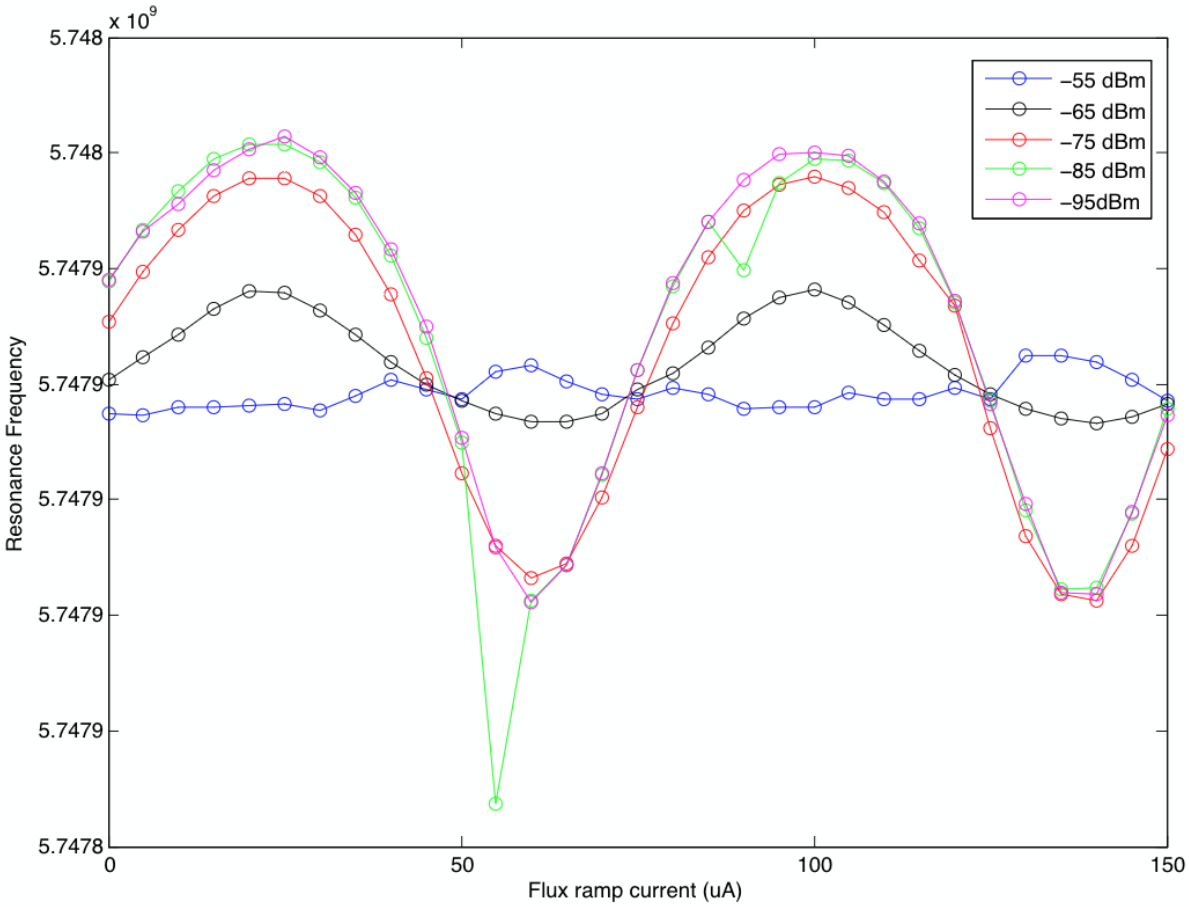

Figure 7.7. The SQUID response with current modulation for different values of signal power.

at different power inputs. As shown in Figure 7.8, the detector should operate at $\sim$ -73 dB.

7.3.2. Flux-ramp rate

As explained in Section 5.3, the SQUID flux-ramp rate f_{ramp} is the effective sampling rate of the detector. From this point of view, it is desired to use a larger f_{ramp}, and therefore larger carrier frequency f_c. However, this rate is restricted by the bandwidth of

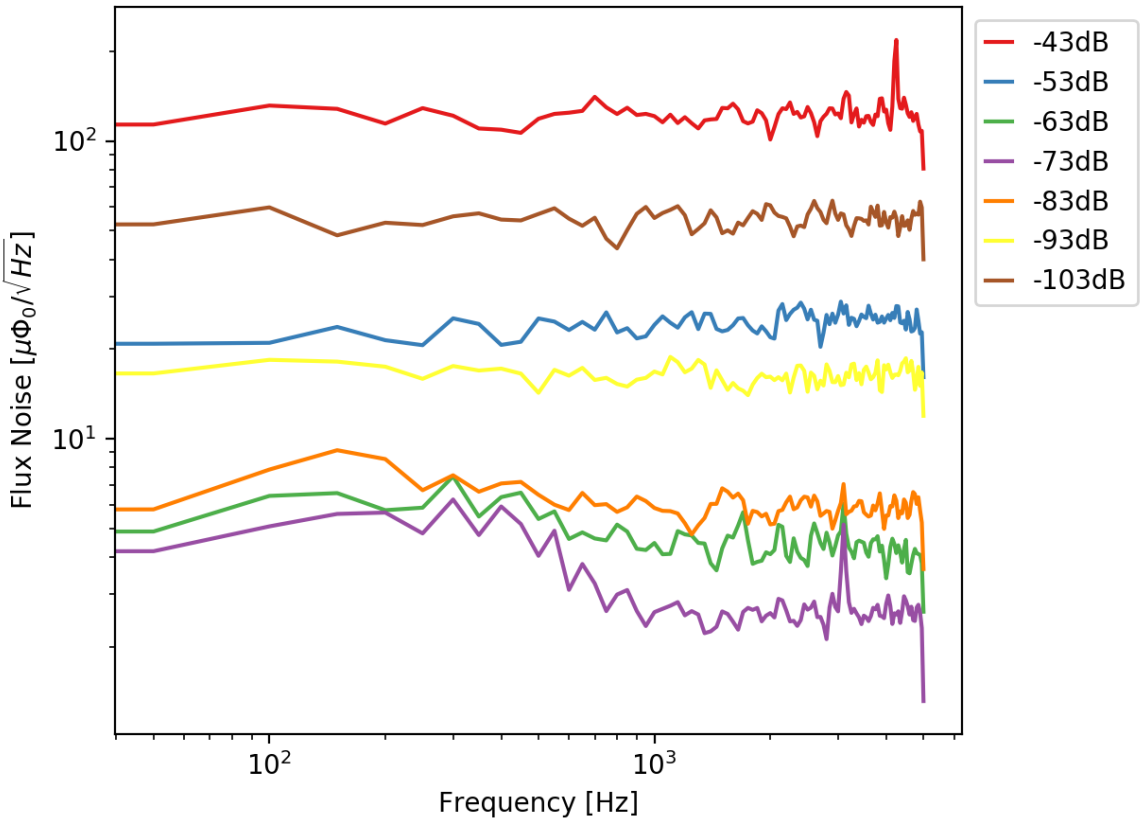

Figure 7.8. System noise at different microwave power inputs. The labeled values are the power arriving at the microwave resonator.

the microwave resonator. If f_c is too large, the resonator cannot catch up and the signal cannot be correctly measured. For our current detector, the resonators' bandwidths are $\sim$ 400 kHz, and experimentally the SQUID modulation signal can go up to 100 kHz before the signal starts to distort.

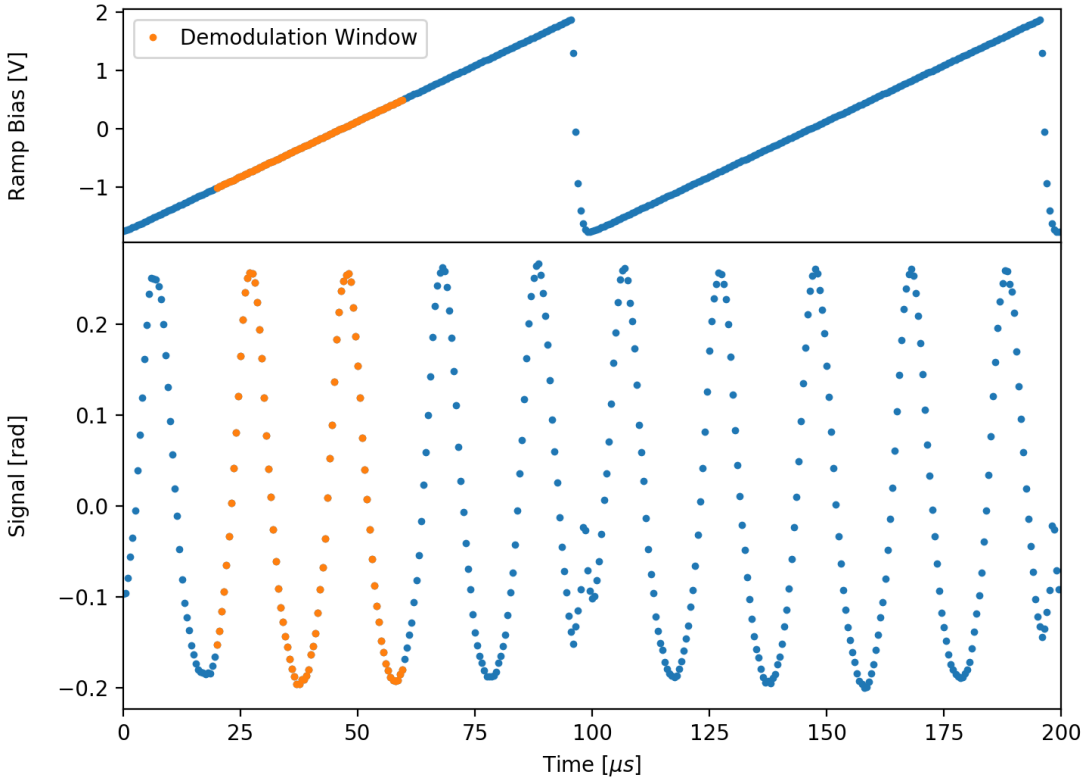

Figure 7.9. Signal modulation in real time. The upper panel is the sawtooth flux-ramp signal that modulates the SQUID. The voltage amplitude is set to cause 5 quantum flux changes in the SQUID as shown by the periodic signal in the lower plot. The y axis of the lower plot is the phase of the signal in the IQ circle (as in Figure 5.4b). When the TES current changes, this periodic response will have a proportional phase change. The region marked in orange illustrates a demodulation window selecting 2 ocsillation periods and has an offset of 40 points counting from the beginning of the flux-ramp.

7.4. Demodulation

As introduced in Section 5.3.4, the TES signal is measured as the relative phase change under SQUID flux-ramp modulation. The TES signal can be calculated by

$$\theta = \arctan\left[\frac{\sum s_t \sin(2\pi f_c t)}{\sum s_t \cos(2\pi f_c t)}\right], \tag{7.8}$$

where θ is the phase shift of the modulated SQUID signal that is caused by the TES current input, and s_t is the TES current signal at time point t. We usually express the demodulated signal in units of Φ/Φ_0 such that

$$\frac{\Phi}{\Phi_0} = \frac{\theta}{2\pi}. \tag{7.9}$$

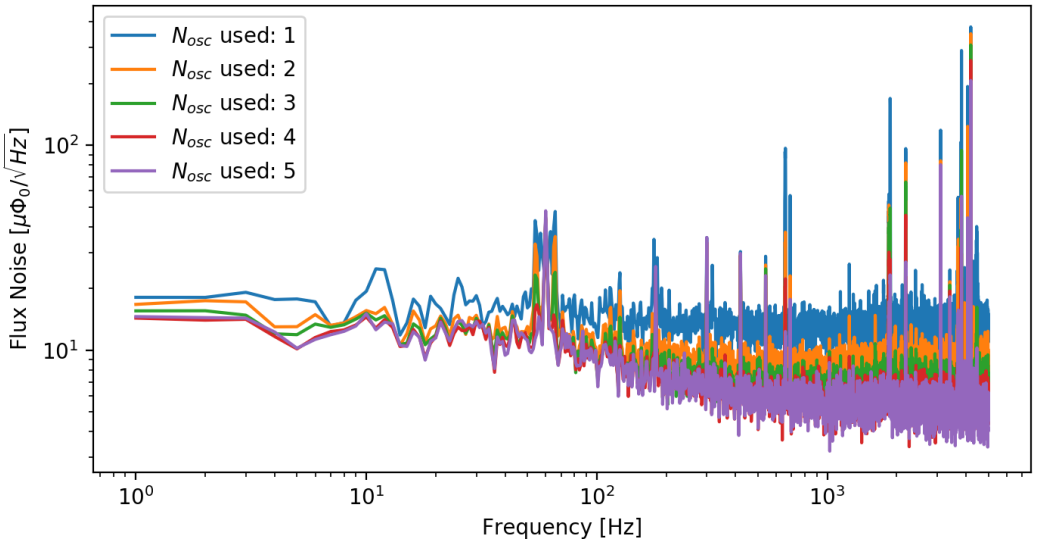

Figure 7.10. The noise PSD calculated using different numbers of oscillation periods within one flux-ramp cycle.

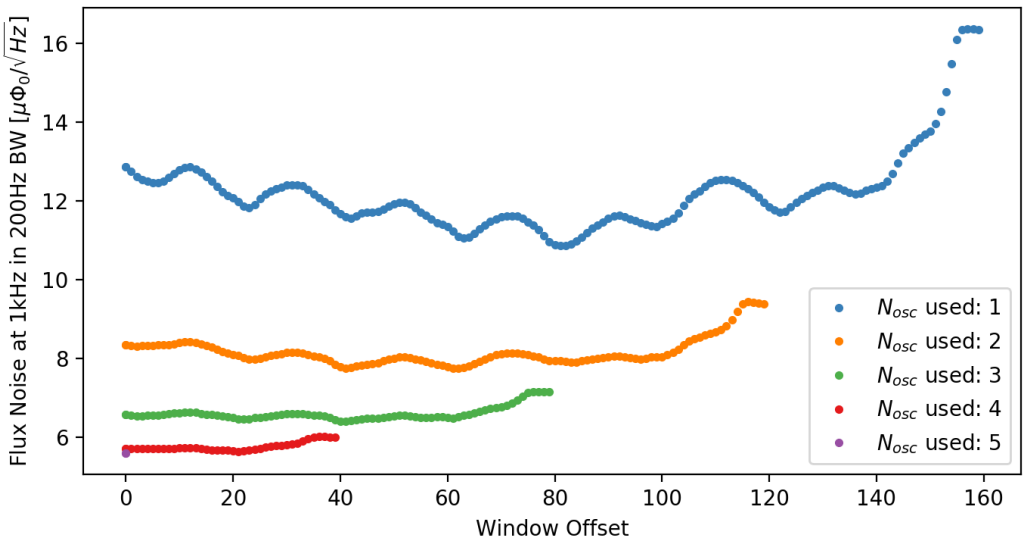

Figure 7.11. Noise PSD at 1 kHz calculated from different windows.

Figure 7.9 shows the sawtooth flux-ramp bias and modulated SQUID signal from experimental measurements. The sampling frequency is $f_s = 2$ MHz, and the flux-ramp frequency is $f_{\text{ramp}} = 10$ kHz, so that one flux-ramp cycle contains 200 data points. In this measurement, the number of oscillations within one ramp is set to be $N = 5$. Around the sawtooth bias resetting region ($\sim$ 100 µs), the SQUID periodic response distorts, which can potentially degrade the demodulated data. Meanwhile, the five oscillations within one flux-ramp cycle shown in Figure 7.9 show unexpected amplitude differences. Therefore, we consider using only part of the flux-ramp data for demodulation, which means that the summations in Equation (7.8) only include points within a selected "window." The region marked in orange is a window containing $N_{\text{osc}} = 2$ oscillations, and has an offset from the beginning of the ramp of 40 data points. We measure the noise level and linearity of the

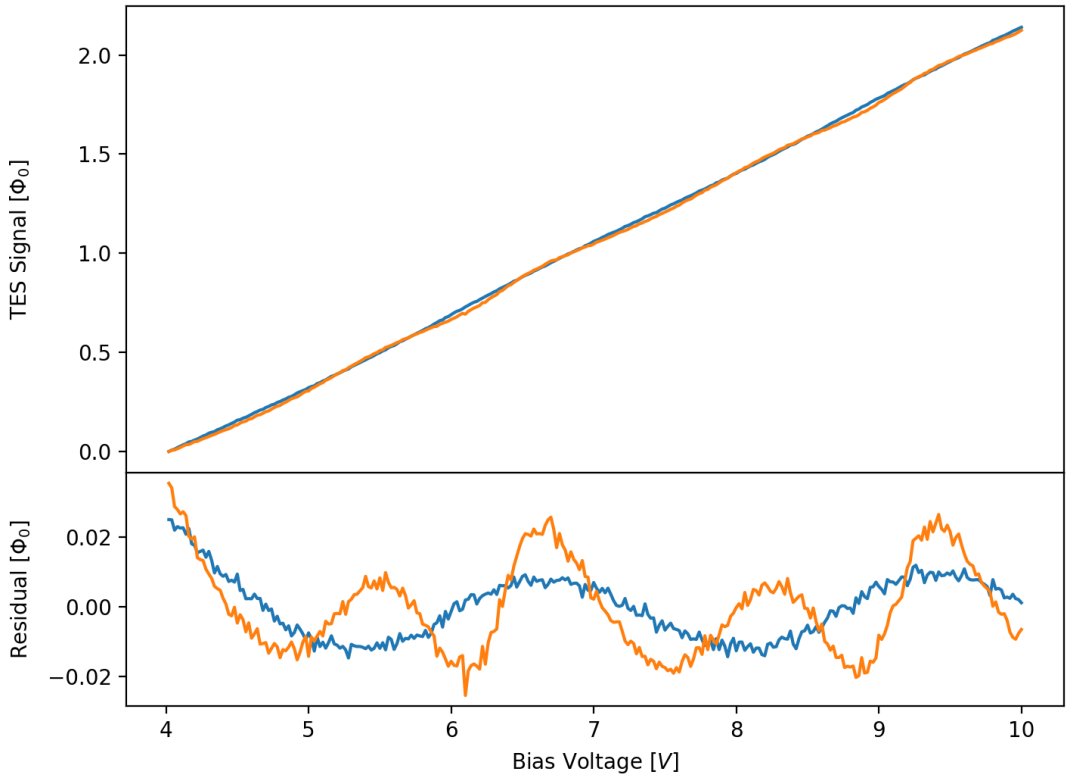

Figure 7.12. Nonlinearity of TES $I - V$ curve normal branch. Both the blue curve and the orange curve are obtained by using $N_{\text{osc}} = 1$, while their window offset are different. The window of the blue curve has an offset of 0, and that of the orange curve is 159.

demodulated signal using windows of different N_{osc}, and different positions (offset from the beginning fo the ramp).

Figure 7.10 shows the noise spectra of the same set of data using different values of N_{osc}. The windows all start from the begining of the flux-ramp (offset = 0). Spectra using longer windows show lower noise. To make a more convenient comparison, we quantify the noise level with the spectrum density at 1 kHz averaged over 200 Hz bandwidth.

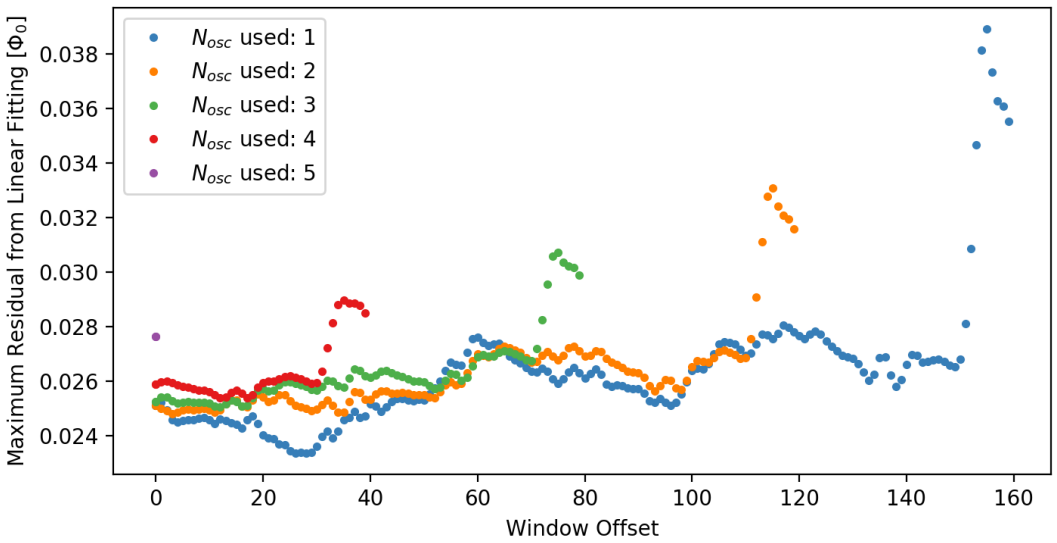

Figure 7.13. Linearity of the demodulated data using different windows.

Figure 7.11 shows this quantity for different values of N_{osc} and for different offsets. The noise appears lower for longer windows. For windows that are shorter than the full ramp cycle, the noise is larger when the window is moved to a position that contains the ramp resetting distorted region. When $N_{\text{osc}} = 5$, although the distorted region is also included, the noise is not significantly lower than the cases when N_{osc} is of other values.

When measuring the $I - V$ characteristics, the demodulated data is found to be nonlinear as shown by the demodulated normal branch line in Figure 7.12. Similar to the noise analysis, the linearity is compared for different values of N_{osc} and window offset. The normal branch $I - V$ data is subtracted from its linear fitting, and the peak-to-peak maximum of the residual is plotted in Figure 7.13. It is found that best linearity is obtained by using windows that do not contain the ramp distorted region.

Combining the noise and linearity analysis, the optimal demodualtion setting is using $N_{\mathrm{osc}} = 4$ and rejecting the ramp distorted region.

7.5. Pulse measurement

The superconducting-to-normal transition edge of the TES has a finite width, therefore high energy photons can drive the TES into normal state and saturate the device. In order to have large dynamic range, the TES is usually biased low in the transition. Figure 7.14 shows the TES pulse response to photons with the same energy at different bias states. The pulse is larger at lower bias state. We usually choose to bias the TES at the 20% normal resistance point to measure pulses.

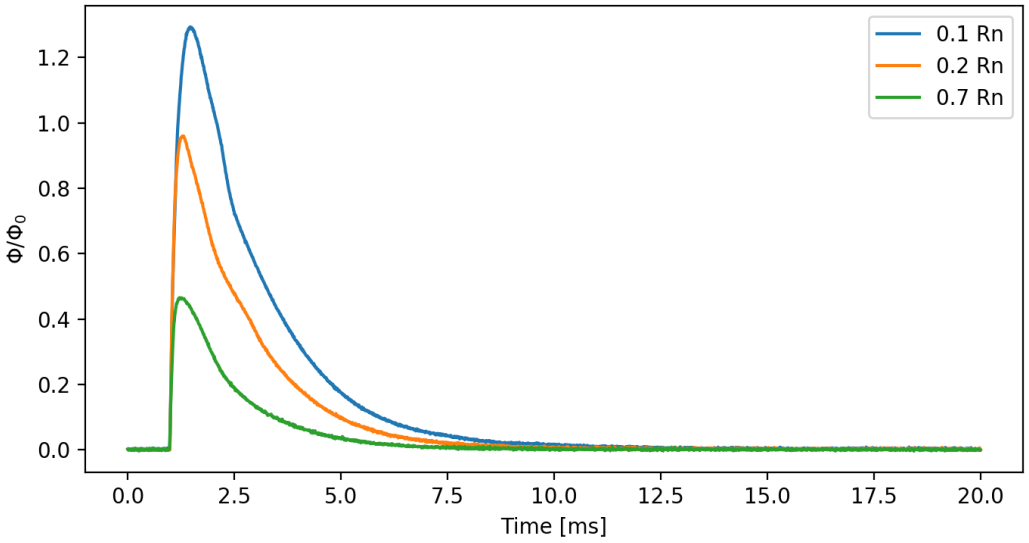

Figure 7.14. TES pulse response at different bias. When the TES is biased lower in the transition, the responsivity is larger.

Since the TES pulse signal is calculated as the phase of the modulated periodic response of the SQUID, it falls in the $(-\Phi_0/2, \Phi_0/2)$ range. If the actual pulse amplitude

Φ is smaller or larger, it will show a periodic jump and is calculated as $\Phi + \Phi_0$ or $\Phi - \Phi_0$, respectively. This periodic jump should be removed before calculating the pulse energy. Figure 7.15 shows a TES pulse before and after the periodic jump has been removed.

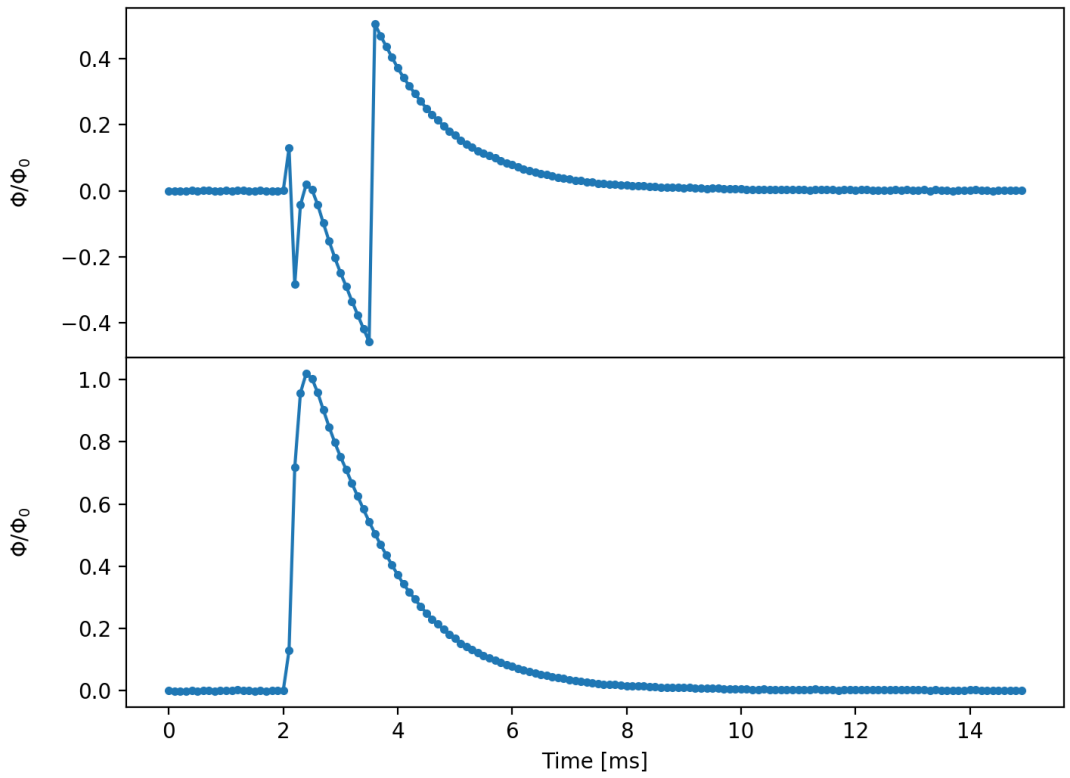

Figure 7.15. TES pulse with Φ_0 jump (upper panel) and after the jump has been removed (lower panel).

7.6. X-ray fluorescence spectra

After measuring the X-ray pulses and calculating their energies, the spectrum of the X-ray can be obtained. The energy calculation method will be introduced in Section 8.1. Figure 7.16 shows part of the fluorescence spectra of a Cu/Ni/Co film that are measured

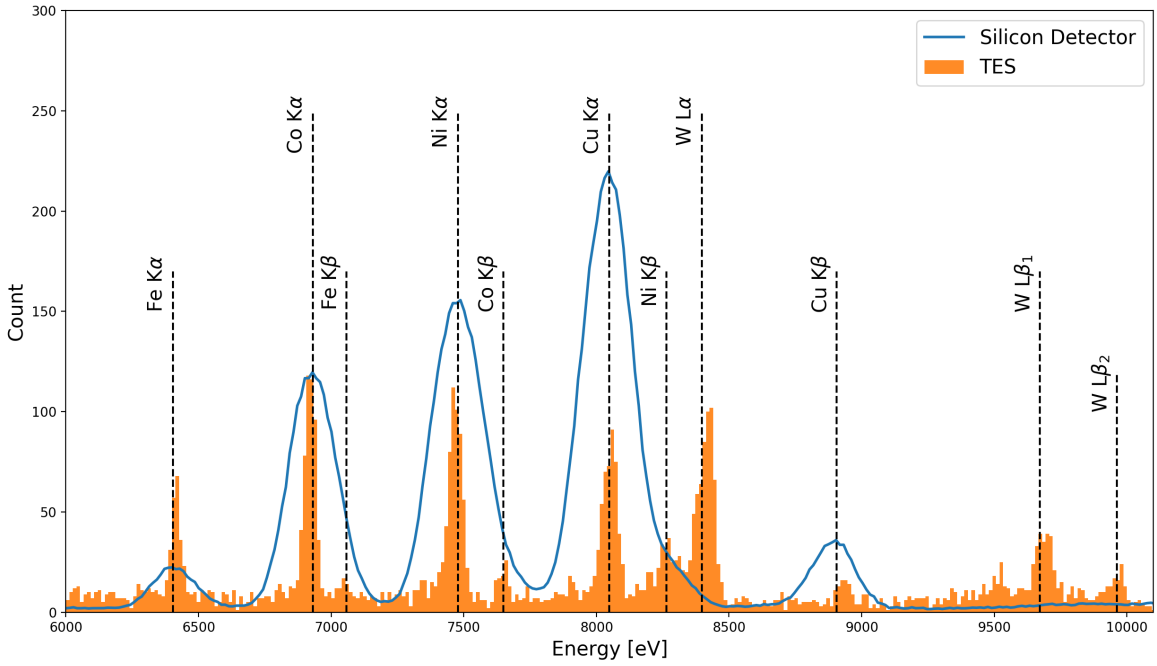

Figure 7.16. The X-ray fluorescence spectra of a film that contains Cu, Ni, and Co.

with a silicon drift detector (Vortex-ME4) and the first TES fabricated in our lab at the Advanced Photon Source. The TES obviously shows a better energy resolution than the silicon detector. Small energy peaks, such as Co $K\beta$ and Ni $K\beta$ can be resolved by the TES but not the silicon detector. The overlaped energy peaks shown in Figure 1.2, which are not resolved by the germanium detector, can be distinguished by our TES.

The misalignment of the emission peaks is due to the nonlinearity of the TES sensor, which needs to be improved in future work. The extra W fluorescence lines shown in the TES spectra could be from the X-ray tube source that was used in the TES experiment. The Fe peaks are from the stainless steel sample chamber.

CHAPTER 8

Pulse processing

Aside from the device design and signal collection, the data processing is also a very important part. The common method used to calculate the pulse energy is "optimal filtering" [**18**][**92**], as is introduced in Section 8.1. The name "optimal" comes from the fact that it maximizes the signal-to-noise ratio when the pulse shape does not change and noise is stationary but not white.

In real detectors, the above described conditions are not always satisfied for a variety of reasons. Section 8.2 describes the use of principal component analysis (PCA) [**93**] as a non-parametric analysis method that requires no prior knowledge of the dataset for the pulse processing of low temperature detectors [**94**]. This method is applied to a dataset from an X-ray thermal kinetic inductance detector, and can be generalized to pulse processing of other types of microcalorimeters including TES. The text and figures in this section draw heavily from my paper [**12**].

8.1. Optimal Filter

8.1.1. Filter derivation

The pulse energy is usually calculated by applying "filters." In our study, the pulses are processed with the "optimal filter." It is called "optimal" because it takes the noise spectra into account, and maximizes the signal's energy resolution when the noise is not white.

Define a pulse signal with the form

$$s(t) = E_0 a(t), \tag{8.1}$$

where E_0 is the energy unit, and $a(t)$ is the shape of the pulse in the time domain. Taking the discrete Fourier transform, the signal becomes a series of components s_i in the frequency bins numbered by i. Similarly, the root-mean-square (rms) value of the noise in a frequency bin is n_i. Choosing a filter consisting of frequency components w_i, the expected value of the signal is

$$E = \sum_{i=1}^{\infty} w_i s_i, \tag{8.2}$$

and the root-mean-square (rms) noise fluctuation is

$$\Delta E_{\rm rms} = \Big(\sum_{i=1}^{\infty} (w_i n_i)^2 \Big)^{1/2}. \tag{8.3}$$

To choose the w_i series that maximizes $E/\Delta E_{\rm rms}$, we take the derivative of this quantity with respect to an individual component w_k as

$$\begin{aligned} \frac{d}{dw_k}\Big(\frac{E}{\Delta E_{\rm rms}}\Big) &= \frac{d}{dw_k}\Big[\Big(\sum_{i=1}^{\infty} w_i s_i\Big)\Big(\sum_{i=1}^{\infty}(w_i n_i)^2\Big)^{-1/2}\Big] \\ &= s_k\Big[\sum_{i=1}^{\infty}(w_i n_i)^2\Big]^{-1/2} - n_k^2 w_k\Big(\sum_{i=1}^{\infty} w_i s_i\Big)\Big[\sum_{i=1}^{\infty}(w_i n_i)^2\Big]^{-3/2}. \end{aligned} \tag{8.4}$$

Setting it to zero, we get

$$w_k = \frac{s_k}{n_k^2}\Big[\sum_{i=1}^{\infty}(w_i n_i)^2 \Big/ \sum_{i=1}^{\infty} w_i s_i\Big]. \tag{8.5}$$

The term in the bracket is a common factor for all frequency components of the filter, and can be dropped. Therefore the filter can be set to

$$w_k = \frac{s_k^*}{|n_k|^2}. \tag{8.6}$$

Considering that s_i are usually complex, the numerator in the filter is set to be the complex conjugate, so that E is real.

8.1.2. Pulse filtering

In an experiment, the noise and a set of pulses are measured. The pulse template used to construct the optimal filter is usually obtained by averaging a number of real pulses. Suppose that the pulse and noise sampling time is T, and the sampling number is N (N is an even number). Taking the discrete Fourier transform (DFT), the signal is transformed into the frequency domain of $[-\frac{N}{2T}, \frac{N}{2T} - 1]$ with the frequency bin size of $\delta f = \frac{1}{T}$. The energy of a pulse $p(t)$ therefore can be calculated by

$$E = E_0 \sum_{i=-\frac{N}{2}}^{\frac{N}{2}-1} \frac{s_i^* \cdot p_i}{|n_i|^2} \Big/ \sum_{i=-\frac{N}{2}}^{\frac{N}{2}-1} \frac{s_i^* \cdot s_i}{|n_i|^2}. \tag{8.7}$$

According to the convolution theorem, alternatively this calculation can be done in the time domain with signal convolution. Transforming the filter into time domain gives

$$w(t) = \mathcal{F}^{-1}\Big[\vec{w}_k\Big]. \tag{8.8}$$

The energy can be calculated by

$$E = E_0 \frac{w(t) * p(t)}{w(t) * s(t)}. \tag{8.9}$$

8.1.3. Energy resolution

Using the optimal filter, the signal fluctuation can be calculated by integrating the noise power after filtering:

$$\begin{aligned} \langle \Delta p^2 \rangle &= \sum_{i=-\frac{N}{2}}^{\frac{N}{2}-1} \Big(\frac{s_i^* n_i}{|n_i|^2} \Big)^2 \delta f \\ &= \sum_{i=-\frac{N}{2}}^{\frac{N}{2}-1} \frac{|s_i|^2}{|n_i|^2} \delta f. \end{aligned} \tag{8.10}$$

Scaling $\langle \Delta p \rangle$ to the energy unit (similar to Equation (8.7)), the energy resolution can be calculated by

$$\begin{aligned} \Delta E &= E_0 \Big(\sum_{i=-\frac{N}{2}}^{\frac{N}{2}-1} \frac{|s_i|^2}{|n_i|^2} \delta f \Big)^{1/2} \Big/ \sum_{i=-\frac{N}{2}}^{\frac{N}{2}-1} \frac{|s_i|^2}{|n_i|^2} \delta f \\ &= E_0 \Big(\sum_{i=-\frac{N}{2}}^{\frac{N}{2}-1} \frac{|s_i|^2}{|n_i|^2} \delta f \Big)^{-1/2}. \end{aligned} \tag{8.11}$$

8.2. Principal component analysis

8.2.1. Math

When X-rays are absorbed in superconducting microcalorimeter detectors, a pulse is generated over some finite time before equilibrium is restored. Consider a set of individually triggered detector pulses ($n = 1, \ldots N$) which are each sampled in time ($t = 1, \ldots T$),

yielding a data matrix $D_{T\times N}$. Our goal is to represent these data using a basis set $C_{T\times S}$ with S characteristic pulse shape factors, with each individual pulse being represented by a weighting $R_{S\times N}$ of members of this basis set, or

$$D_{T\times N} = C_{T\times S} \cdot R_{S\times N}. \tag{8.12}$$

If we can find a reduced subset with $S' < T$ pulse shape factors that the data tell us must be present, we can represent each pulse not with all T time points but in terms of its S' weighting factors. This gives a more compact representation of a pulse over fewer variables, and once the matrix $C_{T\times S'}$ has been determined and its matrix inverted, we can find each pulse's weighting factors $R_{S'\times N}$ by a simple and rapidly-calculated matrix multiplication

$$R_{S'\times N} = C^{-1}_{T\times S'} \cdot D_{T\times N}. \tag{8.13}$$

This analysis is made simpler if the matrix $C_{T\times S}$ is constructed to have orthogonal vectors (to enable matrix inversion using simple transposition) sorted in order of decreasing statistical significance (thus allowing the reduced basis set $C_{T\times S'}$ to be easily separated from the full basis set $C_{T\times S}$). This is precisely what is accomplished by PCA [**93**]. To calculate $C_{T\times S}$, we first calculate the time covariance about the origin of

$$Z_{T\times T} = D_{T\times N} \cdot D^{T}_{N\times T} \tag{8.14}$$

(the relationship between PCA, SVD, and covariance matrices is discussed in textbooks on the topic [**93**]] as well as in Appendix B of [**95**]). Because this time covariance is symmetric, we can represent it in terms of a set of eigenvectors $C_{T\times S}$ and eigenvalue

weightings $\Lambda_{S\times S}$, or

$$Z_{T\times T}\cdot C_{T\times S} = C_{T\times S}\cdot \Lambda_{S\times S}, \tag{8.15}$$

where $S = T$ at the outset of our analysis. Most numerical eigenvalue-solving routines sort their output in terms of decreasing eigenvalue weightings. As a result, the first eigenvector (or the *eigenpulse*) is essentially an average of the pulses. The second eigenvector gives the first correction to that average, the third eigenvector gives the next correction to the first two, and so on. Poorly correlated noise is exiled to higher order eigenvectors. In this way, one can arrive at a reduced set $C_{T\times S'}$ of eigenvectors which describe all of the significant characteristic pulse shape components, and because this is an orthonormal matrix its inverse is given by the transpose so that Equation 8.13 can be calculated from the reduced set of eigenvectors as

$$R_{S'\times N} = C^{-1}_{T\times S'}\cdot D_{T\times N} = C^{T}_{S'\times T}\cdot D_{T\times N} \tag{8.16}$$

With the reduced set of S' eigenvectors, one can also generate a compressed and noise-filtered version of the original data as

$$D'_{T\times N} = C_{T\times S'}\cdot R_{S'\times N}. \tag{8.17}$$

In order to gain intuition on how PCA treats pulse data, we have simulated a dataset which contains exponential pulses with two decay times, two pulse heights and white noise as shown in Figure 8.1a. As shown in Figure 8.1b, when decomposed this dataset contains two primary eigenvectors. The third (and higher) eigenvector contains no shape information and corresponds to noise in the dataset. Thus, we can rebuild the dataset as

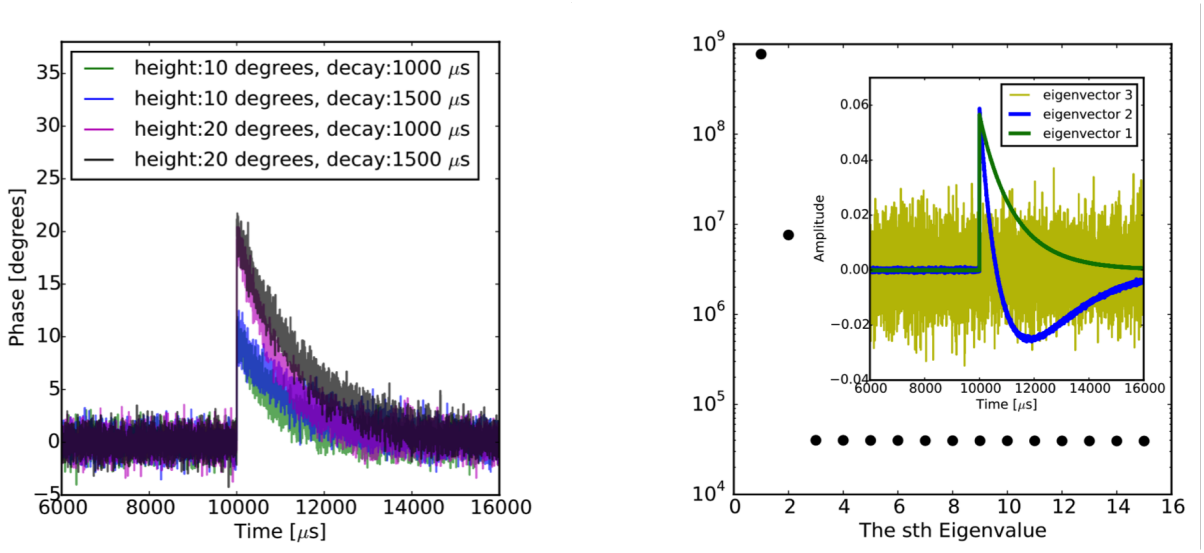

(a) (b)

Figure 8.1. Illustration of eigenvector representation of some simulated pulses. (a) Individual pulses from the simulated dataset. They have a combination of two different heights and shapes, so there are four groups of them. (b) The eigenvalues (which are from $\Lambda_{S\times S}$), and the insert shows the first three eigenvectors.

$D'_{T\times N} = C_{T\times S'=2} \cdot R_{S'=2\times N}$. As shown in Figure 8.2a, noise is greatly filtered yet the pulse shape and height features remain. Figure 8.2b shows the distribution of elements from the weighting matrix $R_{S'=2\times N}$, where components 1 and 2 respectively are the weighting factors of the 1$^{\text{st}}$ and 2$^{\text{nd}}$ eigenvectors.

For pulses with the same shape and height, their weighting factors are the same, so a plot of individual pulses as dots at their particular eigenvector weightings shows four clusters in Figure 8.2b. For pulses with same shape and different height, they have the same ratio of component 1 to component 2. For pulses with different shape but the same height, the linear combination of their weightings is the height, so their data points are on the same line with lines that correspond to different heights parallel to each other.

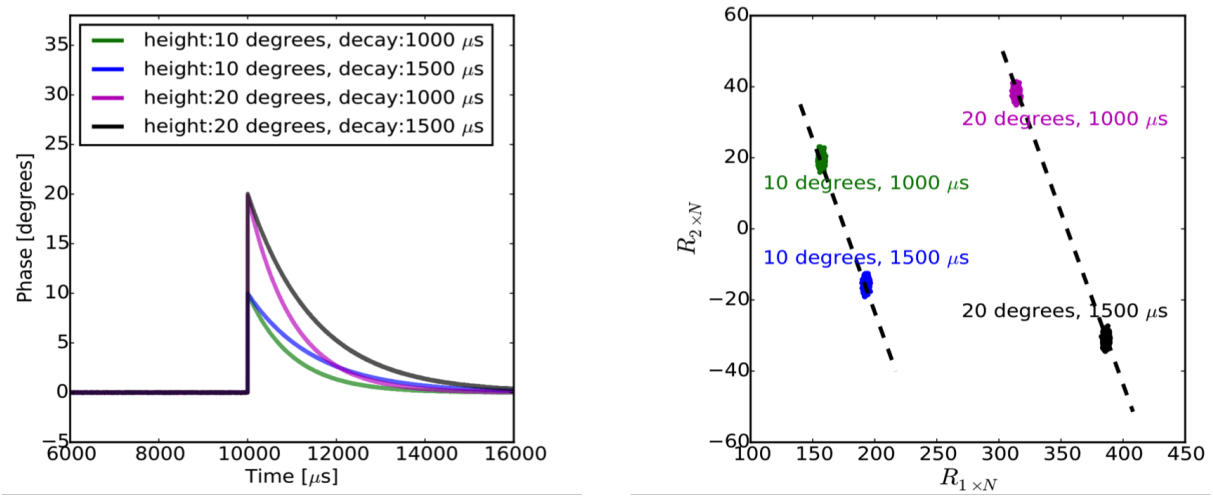

(a) (b)

Figure 8.2. (a) Four PCA reconstructed pulses (Equation 8.17) for $S' = 2$. (b) The distribution of the elements from the weighting matrix $R_{S'\times N}$ for $S' = 2$ from the PCA analysis of the simulated data.

8.2.2. Analysis of TKID Data Using PCA

We now apply the PCA method to a real dataset from an x-ray thermal kinetic inductance detector (TKID). While other groups have reported TKIDs with 75 eV resolution at 6 keV [**96**], we worked here with a TKID [**97, 98**] from which pulse shapes were strongly dependent on the location on the sensor at which an X-ray was absorbed (see Figure 8.3a. About 30 μs after the start of a pulse, the pulse shape does not vary and the amplitude is proportional to the energy, so that the Mn $K\alpha$ and Mn $K\beta$ lines of the Fe-55 source become apparent. In such a dataset, a traditional matched or optimal filter gives no energy information, since the pulse shapes are so different that energy could not be simply extracted from pulse height or area. This has motivated us to consider a PCA analysis which makes no assumptions of the dataset.

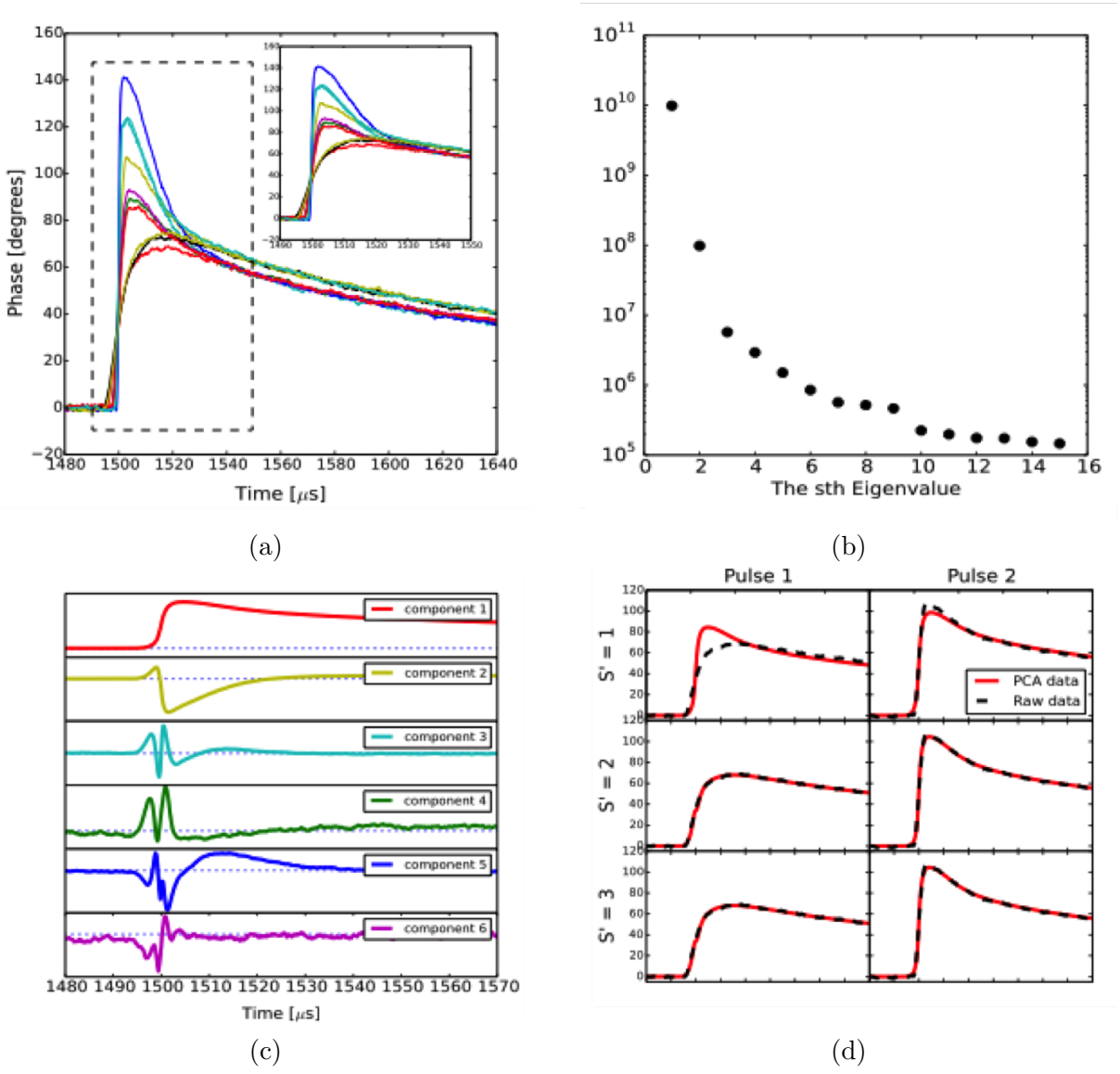

Figure 8.3. (a) The individual pulses from the TKID device. A clear shape difference could be seen at the beginning. After some equilibrium time the pulses go to two branches; the lower one is Mn $K\alpha$, and the upper one is Mn $K\beta$. (b) The first fifteen eigenvalues. (c) The first six eigenvectors. (d) Two raw pulses (black) in comparison with PCA reconstructed pulses (Equation 8.17) for $S' = 1, 2, 3$ (red).

Following the PCA analysis presented in Section 8.2.1, the eigenvalues and eigenvectors are calculated and shown in Figure 8.3. The first two eigenvalues are most significant, but eigenvalues 3–9 encode some subtle variations in the data. In particular, the fluctuations near a time of 1500 µs are related to the jitter in the rise time; these components are likely highly correlated with arrival time. A variant of PCA analysis (using singular value decomposition) recently has been studied for the detection of nearly-coincident pulses [**99**]. While the components beyond the first two may show some correlation with photon energy, we restrict the analysis in this paper to the first two components for simplicity. We can see from Figure 8.3d that there is qualitatively no large difference between $S' = 2$ and $S' = 3$, though rigorous and robust selection metrics for S' need to be developed in the future.

In order to extract energy information, we examined the weighting matrix $R_{S' \times N}$ with $S' = 2$ which is a 2D scatter plot shown in Figure 8.4a. We see two clusters which we associate with the Mn $K\alpha$ (black) and Mn $K\beta$ (blue) lines; black points are pulses in the lower $K\alpha$ branch as in Figure 8.3a, and blue ones (those which are not outliers) are in the higher $K\beta$ branch. These clusters can be automatically detected and separated [**93**], and we have already used these automated approaches in other contexts [**95, 100**]. By fitting a line (red) to the Mn $K\alpha$ cluster, we can generate an axis which was used to rotate the 2D scatter plot of the weighting matrix so that the clusters are vertical. The projection onto the x-axis is used to generate the energy histogram in Figure 8.4b. Thus, the energy can be correlated to a linear combination of the first two PCA components.

We should note that this dataset includes pileup (i.e., more than one pulse in a single time record T) and low energy events. These events, shown in the insertion of Figure 8.4a,

result in PCA weights that are vastly different, or points isolated from the main clusters. By using $S' > 2$ components, pileups can be further distinguished from low energy events. This suggests that PCA can be effective for pileup rejection.

One disadvantage of PCA is its time-consuming eigenvector calculation. A solution is to use a smaller set of pulses as a training set. As an example, we used the first 200 pulses to perform the PCA decomposition and obtain an eigenvector set $C_{T\times S'}^{\text{training}}$. Selecting $S' = 2$, and using Equation 8.13, we obtained the weighting matrix for the remaining $N = 3088$ pulses, which is shown in Figure 8.5a. Compared to Figure 8.4a, despite an inverse of the first component the training data agrees well with what we obtain from direct PCA composition of the entire dataset. The energy histogram also shows very little change. With the trained set of eigenvectors, the PCA reconstruction of the data simplified to a matrix multiplication. This method could enable fast, real-time pulse processing. More work is needed to determine a sufficient number of pulses for the training set.

8.2.3. Summary

This section introduces a non-parametric method for TKID pulse processing based on PCA, and has shown that it is beneficial for datasets with pulse shape variation. It is shown that PCA reduces data noise by the selection of a few number of components, and provides energy information by converting the data into a lower dimension basis system. Moreover, it also provides a new method to identify pileup events and for fast, real-time pulse processing.

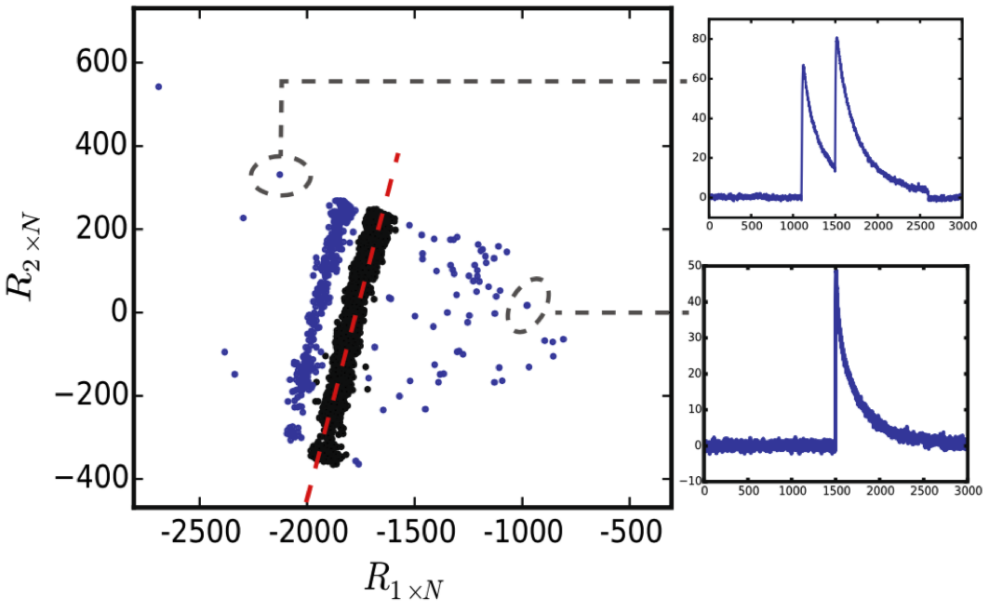

(a)

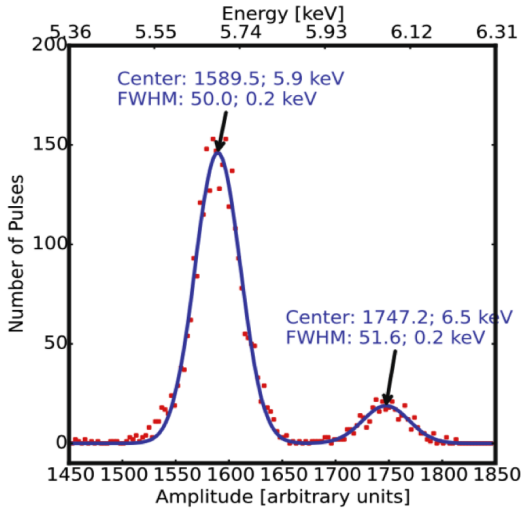

(b)

Figure 8.4. (a) The distribution of elements in the weighting matrix $R_{S'=2\times N}$ from the PCA analysis of the TKID data. The upper insert shows a pileup event and the lower insert shows a low energy event, both with a position separate from the main cluster. (b) The histogram of the pulse set.

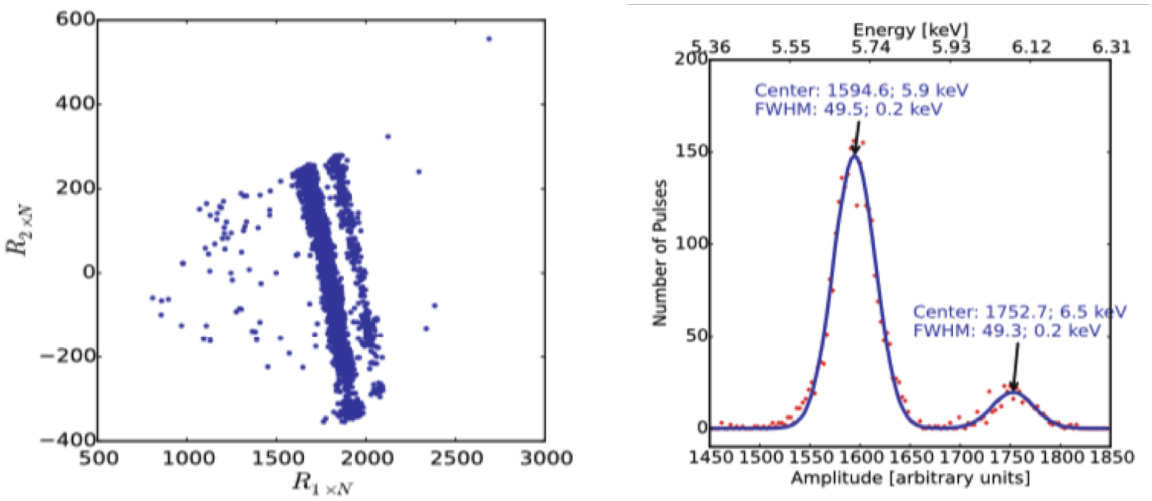

(a) (b)

Figure 8.5. (a) The entire dataset's weighting matrix data distribution, which is calculated with a training eigenvector set from 200 pulses. (b) The energy histogram generated after rotating this weighting matrix.

CHAPTER 9

Conclusion and Outlook

We studied various aspects of TESs for X-ray science applications, including device design, modelling, X-ray absorber material optimization, frequency-division multiplexing readout and pulse processing techniques.

A TES detector for Compton profile measurement and EDXRD experiment has been designed. This detector has segmented pixels, and provides one-dimensional position information. In order to have a large total collection area, it uses long absorbers. Based on the dimension and energy resolution requirement of the applications, the absorber material is selected to be Au. The energy resolution broadening caused by the absorber shape is evaluated. Overall, the detector can achieve an energy resolution of 36.5 eV at 80 keV, which satifies the experimental requirements.

In order to better understand the nonlinear transition shape of the TES, a two-dimensional network model is developed. It consists of four-terminal resistor units, and depending on whether it is a normal metal or a superconducting unit, the resistance is a fixed value or a two-fluid model function of temperature and current. TESs with different normal metal layouts are simulated. It is found that at the low resistive state, since the resistances of the superconducting region units are much lower than that of the normal metal units, the current will meander along the superconducting region. Therefore, the TES with a larger bar spacing can sustain a larger critical current, and the resistance transition is sharper. On the contrary, when the TES is biased at the high resistive state,

current tends to flow uniformly across the TES film, and the layout of the normal metal features does not make a difference in the TES transition slope. This result qualitatively agrees with experimental observations. By considering the localized heating and lateral proximity effect, the model may better describe the TES transition shape.

Bismuth absorbers fabricated with electroplated and evaporated method have been studied. The SEM images have shown distinct grain sizes for these two absorbers. To know the structure under the absorber surfaces, and to make a quantitative comparison, we have measured the absorbers with FF-HEDM and WAXS. It is found that the Evap-Bi has an average grain size of $\sim$ 30 nm, and the Elp-Bi average grain size is $\sim$ 1.4 µm. With the small grain size, Evap-Bi absorbers are likely to scatter or trap heat carriers, generating a low-energy tail in the X-ray spectrum. The Elp-Bi, however, does not have this problem, and therefore makes a good material for X-ray absorbers.

The frequency-division multiplexing technique is described. The RF SQUIDs needs to be modulated with sawtooth signals. The resonant frequencies are measured under different DC biasing of the SQUIDs, and the periodic change of the frequencies is fitted. The sawtooth signal amplitude should be integral multiples of the current period. Similar measurements are conducted on the TES to determine the phase-to-current converting factor. By measuring the noise level and linearity response, the RF SQUID modulation and demodulation conditions are optimized.

The current-voltage feature of the TES has been measured to get the critical temperature T_c, the critial current I_c, the normal resistance R_n, the thermal conductance between the TES and the heat sink G, and the thermal conducting index n. The optimal bias condition of a TES is decided based on these parameters. X-ray emission signals have

been measured by TESs connected in the multiplexing system. The TES has demonstrated a better energy resolution than silicon detectors for enhanced X-ray fluorescence measurements.

Two pulse processing methods – optimal filtering and principal component analysis – are described. For X-ray signals that have severe shape differences, the principal component analysis is especially useful.

We have now assembled a detector that has 4 microwave multiplexer chips, each having 24 TES channels. Good energy resolution have been achieved in the single channel readout mode, and there is still room to engineer the system to improve the resolution to a few eV in the hard X-ray regime. Meanwhile, we are working on reading out $\sim$ 100 channels simultaneously to boost the photon collecting efficiency. The multichannel operation is likely to raise new issues such as cross-talk, which can degrade the energy resolution, and a large data handling problem, which limits the ability for real-time pulse processing. As these new issues are addressed, one might imagine increasing the number of channels per device beyond 100 to a few thousands, provided that the total bandwidth can be several GHz, which is restricted by the bandwidth of the coaxial cable and HEMT amplifiers, and that the frequency spacing between resonator channels is $\sim$ 5 MHz due to the need for inter-channel spacing and large flux-ramp frequency. With the good energy resolution and the prospect of having large arrays, the TES detector will be useful in many scientific areas, such as X-ray emission spectroscopy, X-ray absorption spectroscopy, Compton profile measurement, and energy-dispersive X-ray diffraction, as introduced in the first Chapter.

References

[1] R Alonso Mori, E Paris, G Giuli, S G Eeckhout, M Kavčič, M Žitnik, K Bučar, L G M Pettersson, and P Glatzel. Electronic Structure of Sulfur Studied by X-ray Absorption and Emission Spectroscopy. *Analytical Chemistry*, 81(15):6516–6525, August 2009.

[2] Petr Ilinski, Barry Lai, Zhonghou Cai, Wenbing Yun, Daniel Legnini, Teresa Talarico, Marian Cholewa, Lorraine K Webster, Glen B Deacon, Silvina Rainone, Don R Phillips, and Anton P J Stampfl. The Direct Mapping of the Uptake of Platinum Anticancer Agents in Individual Human Ovarian Adenocarcinoma Cells Using a Hard X-ray Microprobe. *Cancer Research*, 63:1776–1779, April 2003.

[3] N Hiraoka, M Itou, T Ohata, M Mizumaki, Y Sakurai, N Sakai, and IUCr. A new X-ray spectrometer for high-resolution Compton profile measurements at SPring-8. *Journal of Synchrotron Radiation*, 8(1):26–32, January 2001.

[4] P Glatzel, F M F de Groot, O Manoilova, D Grandjean, B M Weckhuysen, Uwe Bergmann, and R Barrea. Range-extended EXAFS at the Ledge of rare earths using high-energy-resolution fluorescence detection: A study of La in LaOCl. *Physical Review B*, 72(014117), July 2005.

[5] Hiroyuki Asakura, Naomi Kawamura, Masaichiro Mizumaki, Kiyofumi Nitta, Kenji Ishii, Saburo Hosokawa, Kentaro Teramura, and Tsunehiro Tanaka. A feasibility study of "range-extended" EXAFS measurement at the Pt L 3-edge of Pt/Al 2O 3in the presence of Au 2O 3. *Journal of Analytical Atomic Spectrometry*, 33(1):84–89, 2018.

[6] J Szlachetko, M Cotte, J Morse, M Salome, P Jagodzinski, J C Dousse, J Hoszowska, Y Kayser, and J Susini. Wavelength-dispersive spectrometer for X-ray microfluorescence analysis at the X-ray microscopy beamline ID21 (ESRF). *Journal of Synchrotron Radiation*, 17:400–408, April 2010.

[7] G Lutz. Silicon drift and pixel devices for X-ray imaging and spectroscopy. *Journal of Synchrotron Radiation*, 13(2):99–109, February 2006.

[8] U Fano. Ionization Yield of Radiations. II. The Fluctuations of the Number of Ions. *Physical Review*, 72(1):26–29, July 1947.

[9] B G Lowe. Measurements of Fano factors in silicon and germanium in the low-energy X-ray region. *Nuclear Instruments and Methods in Physics Research*, 399(2-3):354–364, 1997.

[10] J L Campbell, G Cauchon, M C Lepy, L McDonald, J Plagnard, P Stemmler, W J Teesdale, and G White. A quantitative explanation of low-energy tailing features of Si(Li) and Ge X-ray detectors, using synchrotron radiation. *Nuclear Inst. and Methods in Physics Research, A*, 418(2-3):394–404, December 1998.

[11] B Beckhoff, R Fliegauf, and G Ulm. Investigation of high-resolution superconducting tunnel junction detectors for low-energy X-ray fluorescence analysis. *Spectrochimica Acta Part B*, 58:615–626, 2003.

[12] Daikang Yan, Thomas W Cecil, L Gades, C Jacobsen, T Madden, and A Miceli. Processing of X-ray Microcalorimeter Data with Pulse Shape Variation using Principal Component Analysis. *Journal of Low Temperature Physics*, 184(1-2):1–8, January 2016.

[13] S Kempf, A Fleischmann, L Gastaldo, and C Enss. Physics and Applications of Metallic Magnetic Calorimeters. *Journal of Low Temperature Physics*, 193(3):365–379, March 2018.

[14] Sebastian Kempf, Mathias Wegner, Andreas Fleischmann, Loredana Gastaldo, Felix Herrmann, Maximilian Papst, Daniel Richter, and Christian Enss. Demonstration of a scalable frequency-domain readout of metallic magnetic calorimeters by means of a microwave SQUID multiplexer. *AIP Advances*, 7(1):015007, January 2017.

[15] Simon R Bandler, Joseph S Adams, Catherine N Bailey, Sarah E Busch, James A Chervenak, Megan E Eckart, Audrey E Ewin, Fred M Finkbeiner, Richard L Kelley, Daniel P Kelly, Caroline A Kilbourne, Jan-Patrick Porst, Frederick S Porter, John E Sadleir, Stephen J Smith, and Edward J Wassell. Advances in Small Pixel TES-Based X-Ray Microcalorimeter Arrays for Solar Physics and Astrophysics. *IEEE Transactions on Applied Superconductivity*, 23(1):2100705, June 2013.

[16] Stephen J Smith, J S Adams, C N Bailey, Simon R Bandler, J A Chervenak, M E Eckart, F M Finkbeiner, Richard L Kelley, C A Kilbourne, F S Porter, and J E Sadleir. Small Pitch Transition-Edge Sensors with Broadband High Spectral Resolution for Solar Physics. *Journal of Low Temperature Physics*, 167(3-4):168–175, February 2012.

[17] M K Bacrania, A S Hoover, P J Karpius, M W Rabin, C R Rudy, D T Vo, J A Beall, Douglas Alan Bennett, W B Doriese, G C Hilton, R Horansky, Kent D Irwin, N Jethava, E Sassi, Joel N Ullom, and L R Vale. Large-area microcalorimeter detectors for ultra-high-resolution x-ray and gamma-ray spectroscopy. *IEEE Transactions on Nuclear Science*, 56(4):2299–2302, August 2009.

[18] Daniel McCammon. Thermal Equilibrium Calorimeters – An Introduction. In Christian Enss, editor, *Cryogenic Particle Detection*, pages 1–34. Springer Berlin Heidelberg, 2005.

[19] K D Irwin and G C Hilton. Transition-Edge Sensors. In Christian Enss, editor, *Cryogenic Particle Detection*, pages 63–150. Springer Berlin Heidelberg, 2005.

[20] Kent D Irwin, S W Nam, B Cabrera, B Chugg, and B A Young. A quasiparticle-trap-assisted transition-edge sensor for phonon-mediated particle detection. *Review of Scientific Instruments*, 66(11):5322–5326, 1995.

[21] H. K. Collan, M. Krusius, and G. R. Pickett. Specific heat of antimony and bismuth between 0.03 and 0.8 k. *Physical Review B*, 1:2888–2895, Apr 1970.

[22] W B Doriese, P Abbamonte, B K Alpert, D A Bennett, E V Denison, Y Fang, D A Fischer, C P Fitzgerald, J W Fowler, J D Gard, J P Hays-Wehle, G C Hilton, C Jaye, J L McChesney, L Miaja-Avila, K M Morgan, Y I Joe, G C O'Neil, C D Reintsema, F Rodolakis, D R Schmidt, H Tatsuno, J Uhlig, L R Vale, J N Ullom, and D S Swetz. A practical superconducting-microcalorimeter X-ray spectrometer for beamline and laboratory science. *Review of Scientific Instruments*, 88(5):053108, May 2017.

[23] S R Bandler, R P Brekosky, A D Brown, J A Chervenak, E Figueroa-Feliciano, F M Finkbeiner, N Iyomoto, R L Kelley, C A Kilbourne, F S Porter, J Sadleir, and S J Smith. Performance of TES X-ray Microcalorimeters with a Novel Absorber Design. *Journal of Low Temperature Physics*, 151(1-2):400–405, January 2008.

[24] C. K. Stahle, R. L. Kelley, S. H. Moseley, A. E. Szymkowiak, M. Juda, D. McCammon, and J. Zhang. Thermalization of x-rays in evaporated tin and bismuth films used as the absorbing materials in x-ray calorimeters. *Journal of Low Temperature Physics*, 93(3):257–262, Nov 1993.

[25] Daikang Yan, Lisa M Gades, Tejas Guruswamy, Umeshkumar M Patel, Orlando Quaranta, and Antonino Miceli. Modelling a Transition-Edge Sensor X-Ray Microcalorimeter Linear Array for Compton Profile Measurements and Energy Dispersive Diffraction. *IEEE Transactions on Applied Superconductivity*, 29(5):2100804, April 2019.

[26] Daikang Yan, Lisa M Gades, Tejas Guruswamy, Antonino Miceli, Umeshkumar M Patel, and Orlando Quaranta. A Two-Dimensional Resistor Network Model for Transition-Edge Sensors with Normal Metal Features. *arXiv*, page 1903.06271v1.

[27] Yejun Feng, M S Somayazulu, R Jaramillo, T F Rosenbaum, E D Isaacs, Jingzhu Hu, and Ho-kwang Mao. Energy dispersive x-ray diffraction of charge density waves via chemical filtering. *Review of Scientific Instruments*, 76(6):063913, June 2005.

[28] S R Stock, J S Okasinski, R Woods, J Baldwin, T Madden, Orlando Quaranta, A Rumaiz, T Kuczewski, J Mead, T Krings, P Siddons, A Miceli, and J D Almer. Tomography with energy dispersive diffraction. *Developments in X-Ray Tomography XI*, page 103910A, September 2017.

[29] Abdul K Rumaiz, T Krings, D P Siddons, A J Kuczewski, D Protic, C Ross, G De Geronimo, and Z Zhong. A Monolithic Segmented Germanium Detector with Highly Integrated Readout. *IEEE Transactions on Nuclear Science*, 61(6):3721–3726, December 2014.

[30] Abdul K Rumaiz, A J Kuczewski, J Mead, E Vernon, D Pinelli, E Dooryhee, S Ghose, T Caswell, D P Siddons, A Miceli, J Baldwin, J Almer, J Okasinski, Orlando Quaranta, R Woods, T Krings, and S Stock. Multi-element germanium detectors for synchrotron applications. *Journal of Instrumentation*, 13(04):C04030, April 2018.

[31] Jorge Fernandez-de-Cossio Dorta-Duque Ariadna Mendoza Cuevas. Performance of hybrid angle-energy dispersive X-ray diffraction and fluorescence portable system

for non-invasive surface-mineral identification in Archaeometry. *arXiv*, 1610.06295, 2016.

[32] Naoko Iyomoto, John E. Sadleir, Enectali Figueroa-Feliciano, Tarek Saab, Simon R Bandler, Caroline A Kilbourne, James A Chervenak, Dorothy Talley, Fred M Finkbeiner, Regis P Brekosky, Mark A Lindeman, Richard L Kelley, Frederick S Porter, and Kevin R Boyce. Optimization of x-ray absorbers for TES microcalorimeters. In *Proc. SPIE, High-Energy Detectors in Astronomy*, volume 5501, pages 145–154. SPIE, September 2004.

[33] Tomoya Irimatsugawa, S Hatakeyama, M Ohno, H Takahashi, C Otani, and T Maekawa. High Energy Gamma-Ray Spectroscopy Using Transition-Edge Sensor With a Superconducting Bulk Tantalum Absorber. *IEEE Transactions on Applied Superconductivity*, 25(3):1–3, February 2015.

[34] Kimmo Kinnunen. *Studies of transition-edge sensor physics : thermal models and noise*. University of Jyväskylä, 2011.

[35] A D Brown, S R Bandler, R Brekosky, J A Chervenak, E Figueroa-Feliciano, F Finkbeiner, N Iyomoto, R L Kelley, C A Kilbourne, F S Porter, S Smith, T Saab, and J Sadleir. Absorber Materials for Transition-Edge Sensor X-ray Microcalorimeters. *Journal of Low Temperature Physics*, 151(1-2):413–417, January 2008.

[36] Daikang Yan, Ralu Divan, Lisa M Gades, Peter Kenesei, Timothy J Madden, Antonino Miceli, Jun-Sang Park, Umeshkumar M Patel, Orlando Quaranta, Hemant Sharma, Douglas A Bennett, William B Doriese, Joseph W Fowler, Johnathon D

Gard, James P Hays-Wehle, Kelsey M Morgan, Daniel R Schmidt, Daniel S Swetz, and Joel N Ullom. Eliminating the non-Gaussian spectral response of X-ray absorbers for transition-edge sensors. *Applied Physics Letters*, 111(19):192602, November 2017.

[37] R W Powell, C Y Ho, and P E Liley. Thermal Conductivity of Selected Materials, NSRDS-NBS 8 (1966).

[38] T P Bernat, N B Alexander, and J L Kaae. Thermal and electrical conductivities of electroplated gold. *Fusion Science and Technology*, 51(4):782–785.

[39] O. Quaranta, D. Yan, T. Madden, L. Gades, U. Patel, D. Becker, D. Bennett, J. Hays-Wehle, G. Hilton, J. Gard, A. Miceli, B. Mates, C. Reintsema, D. Schmidt, D. Swetz, J. Ullom, and L. Vale. Performance characterization of microwave-multiplexed transition edge sensors for x-ray synchrotron applications. *2017 16th International Superconductive Electronics Conference (ISEC)*, pages 1–3, June 2017.

[40] Enectali Figueroa-Feliciano. Complex microcalorimeter models and their application to position-sensitive detectors. *Journal of Applied Physics*, 99(11):114513, 2006.

[41] I J Maasilta. Complex impedance, responsivity and noise of transition-edge sensors: Analytical solutions for two- and three-block thermal models. *AIP Advances*, 2:042110, December 2012.

[42] Tarek Saab, Enectali Figueroa-Feliciano, Naoko Iyomoto, Simon R Bandler, J A Chervenak, Richard L Kelley, C A Kilbourne, F S Porter, and J E Sadleir. Determining the thermal diffusivity in microcalorimeter absorbers and its effect on detector response. *Journal of Applied Physics*, 102(10):104502, November 2007.

[43] Stephen J Smith, Chris H Whitford, and George W Fraser. Optimised filtering for improved energy and position resolution in position-sensitive TES based X-ray detectors. *Nuclear Instruments and Methods A*, 556(1):237–245, January 2006.

[44] R A Stern, A Rausch, S Deiker, D Martínez-Galarce, L Shing, Kent D Irwin, Joel N Ullom, G O'Neil, G Hilton, and L Vale. X-ray Microcalorimeter Research for Solar Physics at LMSAL and NIST: An Update. *Journal of Low Temperature Physics*, 151(3-4):721–726, February 2008.

[45] Gensheng Wang, C L Chang, V Yefremenko, V Novosad, J Pearson, R Divan, and J E Carlstrom. Mo/Au Bilayer TES Resistive Transition Engineering. *IEEE Transactions on Applied Superconductivity*, 25(3):1–5, February 2015.

[46] Joel N Ullom and Douglas A Bennett. Review of superconducting transition-edge sensors for x-ray and gamma-ray spectroscopy*. *Superconductor Science and Technology*, 28(8):1–36, August 2015.

[47] Douglas A Bennett, Daniel S Swetz, Daniel R Schmidt, and Joel N Ullom. Resistance in transition-edge sensors: A comparison of the resistively shunted junction and two-fluid models. *Physical Review B*, 87(2):020508, January 2013.

[48] A Kozorezov, A A Golubov, D D E Martin, P A J de Korte, Mark A Lindeman, R A Hijmering, J van der Kuur, H F C Hoevers, L Gottardi, M Yu Kupriyanov, and J K Wigmore. Modelling the resistive state in a transition edge sensor. *Applied Physics Letters*, 99(6):063503, August 2011.

[49] Kent D Irwin, G C Hilton, D A Wollman, and John M Martinis. Thermal-response time of superconducting transition-edge microcalorimeters. *Journal of Applied Physics*, 83(8):3978–3985, 1998.

[50] Douglas A Bennett, Daniel S Swetz, R D Horansky, D R Schmidt, and Joel N Ullom. A Two-Fluid Model for the Transition Shape in Transition-Edge Sensors. *Journal of Low Temperature Physics*, 167(3-4):102–107, November 2011.

[51] Rebecca C Harwin, D C Goldfinger, and S Withington. Modelling proximity effects in transition edge sensors to investigate the influence of lateral metal structures. *Superconductor Science and Technology*, 30(084001), June 2017.

[52] Daniel S Swetz, Douglas A Bennett, Kent D Irwin, D R Schmidt, and Joel N Ullom. Current distribution and transition width in superconducting transition-edge sensors. *Applied Physics Letters*, 101(24):242603, December 2012.

[53] Kelsey M Morgan, C G Pappas, Douglas A Bennett, J D Gard, J P Hays-Wehle, G C Hilton, C D Reintsema, D R Schmidt, Joel N Ullom, and Daniel S Swetz. Dependence of transition width on current and critical current in transition-edge sensors. *Applied Physics Letters*, 110(21):212602, May 2017.

[54] Douglas Alan Bennett, D R Schmidt, and Daniel S Swetz. Phase-slip lines as a resistance mechanism in transition-edge sensors. *Applied Physics Letters*, 104:04602, January 2014.

[55] H Tatsuno, W B Doriese, D A Bennett, C Curceanu, J W Fowler, J Gard, F P Gustafsson, T Hashimoto, R S Hayano, J P Hays-Wehle, G C Hilton, M Iliescu, S Ishimoto, K Itahashi, M Iwasaki, K Kuwabara, Y Ma, J Marton, H Noda, G C O'Neil, S Okada, H Outa, C D Reintsema, M Sato, D R Schmidt, H Shi, K Suzuki, T Suzuki, J Uhlig, J N Ullom, E Widmann, S Yamada, J Zmeskal, and D S Swetz. Absolute Energy Calibration of X-ray TESs with 0.04 eV Uncertainty at 6.4 keV in a Hadron-Beam Environment. *Journal of Low Temperature Physics*, 184(3):930–937, January 2016.

[56] Daikang Yan, Ralu Divan, Lisa M Gades, Peter Kenesei, Timothy J Madden, Antonino Miceli, Jun-Sang Park, Umeshkumar M Patel, Orlando Quaranta, Hemant Sharma, Douglas A Bennett, William B Doriese, Joseph W Fowler, Johnathon D Gard, James P Hays-Wehle, Kelsey M Morgan, Daniel R Schmidt, Daniel S Swetz, and Joel N Ullom. Microstructure Analysis of Bismuth Absorbers for Transition-Edge Sensor X-ray Microcalorimeters. *Journal of Low Temperature Physics*, pages 1–6, March 2018.

[57] J N Ullom, J A Beall, W B Doriese, W D Duncan, L Ferreira, G C Hilton, K D Irwin, C D Reintsema, and L R Vale. Optimized transition-edge x-ray microcalorimeter with 2.4eV energy resolution at 5.9keV. *Applied Physics Letters*, 87(19):194103, 2005.

[58] Lisa M Gades, Thomas W Cecil, Ralu Divan, Dan R Schmidt, Joel N Ullom, Timothy J Madden, Daikang Yan, and Antonino Miceli. Development of Thick Electroplated Bismuth Absorbers for Large Collection Area Hard X-ray Transition Edge Sensors. *IEEE Transactions on Applied Superconductivity*, 27(4):1–5, February 2017.

[59] A.H. Said and S.D. Shastri. Silicon saw-tooth refractive lens for high-energy x-rays made using a diamond saw. *Journal of Synchrotron Radiation*, 17:425–427, 2010.

[60] J H Lee, C C Aydiner, J Almer, J Bernier, K W Chapman, P J Chupas, D Haeffner, K Kump, P L Lee, U Lienert, A Miceli, and G Vera. Synchrotron applications of an amorphous silicon flat-panel detector. *Journal of Synchrotron Radiation*, 15:477–488, July 2008.

[61] Yu Shu, Wentao Hu, Zhongyuan Liu, Guoyin Shen, Bo Xu, Zhisheng Zhao, Julong He, Yanbin Wang, Yongjun Tian, and Dongli Yu. Coexistence of multiple metastable polytypes in rhombohedral bismuth. *Scientific Reports*, 6(20337), January 2016.

[62] Midas, microstructural imaging using diffraction analysis software, Accessed: 2017-10-20. https://www1.aps.anl.gov/science/scientific-software/midas.

[63] J W Fowler, B K Alpert, W B Doriese, Y I Joe, G C O'Neil, J N Ullom, and D S Swetz. The Practice of Pulse Processing. *Journal of Low Temperature Physics*, 184(1):374–381, December 2015.

[64] G Holzer, M Fritsch, M Deutsch, J Härtwig, and E Förster. Kα1,2and Kβ1,3x-ray emission lines of the 3dtransition metals. *Physical Review A*, 56(6):4554–4568, December 1997.

[65] J W Fowler, B K Alpert, D A Bennett, W B Doriese, J D Gard, G C Hilton, L T Hudson, Y I Joe, K M Morgan, G C O'Neil, C D Reintsema, D R Schmidt, D S Swetz, C I Szabo, and J N Ullom. A reassessment of absolute energies of the x-ray L lines of lanthanide metals. *Metrologia*, 54(4):494–511, June 2017.

[66] A Kozorezov. Energy Down-Conversion and Thermalization in Metal Absorbers. *Journal of Low Temperature Physics*, 167(3-4):473–484, November 2011.

[67] C. A. Kilbourne, S. R. Bandler, A. D. Brown, J. A. Chervenak, E. Figueroa-Feliciano, F. M. Finkbeiner, N. Iyomoto, R. L. Kelley, F. S. Porter, T. Saab, J. Sadleir, and J. White. High-density arrays of x-ray microcalorimeters for Constellation-X. In *Society of Photo-Optical Instrumentation Engineers (SPIE) Conference Series*, volume 6266, page 626621, June 2006.

[68] Ctirad Uher, J Heremans, J-P Issi, AM de Goer, and M Locatelli. Thermal conductivity of tin-doped bismuth between 50 mk and 7k. *Journal of Physics C: Solid State Physics*, 18(15):3001, 1985.

[69] F. Y. Yang, Kai Liu, Kimin Hong, D. H. Reich, P. C. Searson, and C. L. Chien. Large magnetoresistance of electrodeposited single-crystal bismuth thin films. *Science*, 284(5418):1335–1337, 1999.

[70] C. A. Hoffman, J. R. Meyer, F. J. Bartoli, A. Di Venere, X. J. Yi, C. L. Hou, H. C. Wang, J. B. Ketterson, and G. K. Wong. Semimetal-to-semiconductor transition in bismuth thin films. *Physical Review B*, 48:11431–11434, Oct 1993.

[71] Yu-Ming Lin, Xiangzhong Sun, and M S Dresselhaus. Theoretical investigation of thermoelectric transport properties of cylindrical Bi nanowires. *Physical Review B*, 62(7):4610–4623, August 2000.

[72] G. Dresselhaus, M. S. Dresselhaus, Z. Zhang, X. Sun, J. Ying, and G. Chen. Modeling thermoelectric behavior in bi nano-wires. In *Seventeenth International Conference on Thermoelectrics. Proceedings ICT98 (Cat. No.98TH8365)*, pages 43–46, May 1998.

[73] Yu-Ming Lin, Stephen B Cronin, Jackie Y Ying, M S Dresselhaus, and Joseph P Heremans. Transport properties of Bi nanowire arrays. *Applied Physics Letters*, 76(26):3944–3946, June 2000.

[74] T Tabata, P Andreo, and K Shinoda. An analytic formula for the extrapolated range of electrons in condensed materials. *Nuclear Instruments and Methods in Physics Research B*, 119:463, 1996.

[75] S M Seltzer and M J Berger. Improved procedure for calculating the collision stopping power of elements and compounds for electrons and positrons. *The International Journal of Applied Radiation and Isotopes*, 35:665, 1984.

[76] Alexei N Grum-Grzhimailo, Tatiana Pikuz, Anatoly Faenov, Takeshi Matsuoka, Norimasa Ozaki, Bruno Albertazzi, Sergei Pikuz, Yuichi Inubushi, Makina Yabashi, Kensuke Tono, Hirokatsu Yumoto, Haruhiko Ohashi, Tetsuya Ishikawa, and Ryosuke Kodama. On the size of the secondary electron cloud in crystals irradiated by hard X-ray photons. *The European Physical Journal D*, 71(3):309, March 2017.

[77] Dale Li, Bradley K Alpert, Daniel Thomas Becker, Douglas A Bennett, G A Carini, H M Cho, W B Doriese, J E Dusatko, Joseph W Fowler, J C Frisch, J D Gard, S Guillet, G C Hilton, M R Holmes, Kent D Irwin, V Kotsubo, S J Lee, John A B Mates, Kelsey M Morgan, K Nakahara, C G Pappas, C D Reintsema, D R Schmidt, S R Smith, Daniel S Swetz, J B Thayer, Charles J Titus, Joel N Ullom, L R Vale, D D Van Winkle, A Wessels, and L Zhang. TES X-ray Spectrometer at SLAC LCLS-II. *Journal of Low Temperature Physics*, 134(14):1–11, September 2018.

[78] Omid Noroozian, John A B Mates, Douglas A Bennett, Justus A Brevik, Joseph W Fowler, Jiansong Gao, Gene C Hilton, Robert D Horansky, Kent D Irwin, Zhao Kang, Daniel R Schmidt, Leila R Vale, and Joel N Ullom. High-resolution gamma-ray spectroscopy with a microwave-multiplexed transition-edge sensor array. *Applied Physics Letters*, 103(20):202602, 2013.

[79] David M Pozar. *Microwave Engineering, 4th Edition*. Wiley Global Education, November 2011.

[80] K Geerlings, S Shankar, E Edwards, L Frunzio, R J Schoelkopf, and M H Devoret. Improving the quality factor of microwave compact resonators by optimizing their geometrical parameters. *Applied Physics Letters*, 100(19):192601, 2012.

[81] Robert Rifkin. rf SQUID's in the nonhysteretic mode: Detailed comparison of theory and experiment. *Journal of Applied Physics*, 47(6):2645–2650, 1976.

[82] J Clarke and A I Braginski. The SQUID Handbook: Fundamentals and Technology of SQUIDs and SQUID Systems. Vol. 1, 2006.

[83] J R Waldram. The Josephson effects in weakly coupled superconductors. *Reports on Progress in Physics*, 39(8):751–827, August 1976.

[84] Yukio Tanaka and Satoshi Kashiwaya. Theory of Josephson effects in anisotropic superconductors. *Physical Review B*, 56(2):892–912, July 1997.

[85] Z H Barber, J W A Robinson, M G Blamire, and Avradeep Pal. Pure second harmonic current-phase relation in spin-filter Josephson junctions. *Nature Communications*, 5:3340, February 2014.

[86] M J A Stoutimore, A N Rossolenko, V V Bol'ginov, V A Oboznov, A Y Rusanov, D S Baranov, N Pugach, S M Frolov, V V Ryazanov, and D J Van Harlingen. Second-Harmonic Current-Phase Relation in Josephson Junctions with Ferromagnetic Barriers. *Physical Review Letters*, 121(17):177702, October 2018.

[87] John A B Mates, K D Irwin, L R Vale, G C Hilton, J Gao, and K W Lehnert. Flux-Ramp Modulation for SQUID Multiplexing. *Journal of Low Temperature Physics*, 167(5-6):707–712, February 2012.

[88] Inc. HPD. Cryostat Model 102 Denali, 2018.

[89] Timothy J Madden, Thomas W Cecil, Lisa M Gades, Orlando Quaranta, Daikang Yan, Antonino Miceli, Daniel Thomas Becker, Douglas Alan Bennett, James P Hays-Wehle, Gene C Hilton, Johnathon D Gard, John A B Mates, Carl D Reintsema, Dan R Schmidt, Daniel S Swetz, Leila R Vale, and Joel N Ullom. Development of ROACH Firmware for Microwave Multiplexed X-Ray TES Microcalorimeters. *IEEE Transactions on Applied Superconductivity*, 27(4):1–4, 2017.

[90] S H Moseley, John C Mather, and Daniel McCammon. Thermal detectors as x-ray spectrometers. *Journal of Applied Physics*, 56(5):1257–1262, 1984.

[91] Jiansong Gao. *The Physics of Superconducting Microwave Resonators*. California Institute of Technology. Division of Engineering and Applied Science, 2008.

[92] A E Szymkowiak, R L Kelley, S H Moseley, and C K Stahle. Signal processing for microcalorimeters. *Journal of Low Temperature Physics*, 93(3):281–285, 1993.

[93] E. R. Malinowski. *Factor analysis in chemistry*. John H. Wiley & Sons, New York, 3^{nd} edition, 2002.

[94] S E Busch, J S Adams, S R Bandler, J A Chervenak, M E Eckart, F M Finkbeiner, D J Fixsen, R L Kelley, C A Kilbourne, J P Porst, F S Porter, J E Sadleir, and

S J Smith. Progress Toward Improving Analysis of TES X-ray Data Using Principal Component Analysis. *Journal of Low Temperature Physics*, 184(1):382–388, Jul 2016.

[95] M Lerotic, C Jacobsen, T Schäfer, and S Vogt. Cluster analysis of soft X-ray spectromicroscopy data. *Ultramicroscopy*, 100(1-2):35–57, July 2004.

[96] Gerhard Ulbricht, Benjamin A Mazin, Paul Szypryt, Alex B Walter, Clint Bockstiegel, and Bruce Bumble. Highly multiplexible thermal kinetic inductance detectors for x-ray imaging spectroscopy. *Applied Physics Letters*, 106(25):251103, June 2015.

[97] O Quaranta, T W Cecil, L Gades, B Mazin, and A Miceli. X-ray photon detection using superconducting resonators in thermal quasi-equilibrium. *Superconductor Science and Technology*, 26(10):105021, September 2013.

[98] A Miceli, T W Cecil, L Gades, and O Quaranta. Towards X-ray Thermal Kinetic Inductance Detectors. *Journal of Low Temperature Physics*, 176(3-4):497–503, August 2014.

[99] Bradley K Alpert, E Ferri, Douglas Alan Bennett, M Faverzani, Joseph W Fowler, A Giachero, J Hays-Wehle, M Maino, A Nucciotti, A Puiu, Daniel S Swetz, and Joel N Ullom. Algorithms for Identification of Nearly-Coincident Events in Calorimetric Sensors. *Journal of Low Temperature Physics*, 184:263–273, December 2015.

[100] M Lerotic, R Mak, S Wirick, F Meirer, and C Jacobsen. MANTiS: a program for the analysis of X-ray spectromicroscopy data. *Journal of Synchrotron Radiation*, 21:1206–1212, July 2014.

[101] Douglas A Bennett, R D Horansky, A S Hoover, N J Hoteling, M W Rabin, D R Schmidt, Daniel S Swetz, L R Vale, and Joel N Ullom. An analytical model for pulse shape and electrothermal stability in two-body transition-edge sensor microcalorimeters. *Applied Physics Letters*, 97(10):102504, September 2010.

APPENDIX A

Analytical solution of sets of differential equations

This chapter illustrates how to get the analytical solution of TES pulse response by solving the electrothermal feedback matrix.

A.1. Solve by matrix

The first-order (as to the time differential) homogeneous matrix ordinary differential equation takes the form:

$$\dot{\vec{X}}(t) = \vec{A}\vec{X}(t). \tag{A.1}$$

Its general solution has the form of:

$$\vec{X}(t) = \mu_1 e^{\lambda_1 t}\vec{v_1} + \mu_2 e^{\lambda_2 t}\vec{v_2} + ... + \mu_n e^{\lambda_n t}\vec{v_n}, \tag{A.2}$$

where λ_1, λ_2, ..., λ_n are the eigenvalues of $\vec{A}$; $\vec{v_1}$, $\vec{v_2}$, ..., $\vec{v_n}$, are the correponding eigenvectors; and μ_1, μ_2, ..., μ_n are constants.

The solution can be obtained following three steps:

(1): Find the eigenvalues λ;

(2): Find the eigenvectors $\vec{v}$;

(3): Calculate the constants μ from the initial condition $\vec{X}(0)$.

This section will show how to solve a general 2-order matrix, and apply the result to the simple TES model discussed in Sec. 2.1.

A.1.1. Find the eigenvalues

Denote the matrix with symbolic numbers:

$$\vec{A} = \begin{bmatrix} a & b \\ c & d \end{bmatrix}. \tag{A.3}$$

Its eigenvalues satisfy

$$\begin{vmatrix} a-\lambda & b \\ c & d-\lambda \end{vmatrix} = 0, \tag{A.4}$$

which is

$$(a-\lambda)(d-\lambda) - bc = 0. \tag{A.5}$$

Solve the quadratic equation, we get the two eigenvalues:

$$\lambda_{1,2} = \frac{(a+d) \pm \sqrt{(a-d)^2 + 4bc}}{2} \tag{A.6}$$

A.1.2. Find the eigenvectors

Write the eigenvector as

$$\vec{v} = \begin{bmatrix} \alpha \\ \beta \end{bmatrix}. \tag{A.7}$$

It satisfies

$$\begin{bmatrix} a-\lambda & b \\ c & d-\lambda \end{bmatrix} \begin{bmatrix} \alpha \\ \beta \end{bmatrix} = \vec{0}, \tag{A.8}$$

from which we have

$$c\alpha + (d - \lambda)\beta = 0. \tag{A.9}$$

Let $\beta = 1$, we have

$$\vec{v_{1,2}} = \begin{bmatrix} \dfrac{\lambda_{1,2} - d}{c} \\ \\ 1 \end{bmatrix}, \tag{A.10}$$

A.1.3. Calculate the constants μ from the initial condition $\vec{X}(0)$

With initial condiciton:

$$\vec{X}(0) = \mu_1 \vec{v_1} + \mu_2 \vec{v_2}, \tag{A.11}$$

or

$$\begin{bmatrix} x_0 \\ \\ y_0 \end{bmatrix} = \begin{bmatrix} \alpha_1 & \alpha_2 \\ \\ \beta_1 & \beta_2 \end{bmatrix} \begin{bmatrix} \mu_1 \\ \\ \mu_2 \end{bmatrix} \tag{A.12}$$

we have

$$\begin{aligned} \begin{bmatrix} \mu_1 \\ \\ \mu_2 \end{bmatrix} &= \begin{bmatrix} \alpha_1 & \alpha_2 \\ \\ \beta_1 & \beta_2 \end{bmatrix}^{-1} \begin{bmatrix} x_0 \\ \\ y_0 \end{bmatrix} \\ &= \begin{vmatrix} \alpha_1 & \alpha_2 \\ \\ \beta_1 & \beta_2 \end{vmatrix}^{-1} \begin{bmatrix} \beta_2 & -\alpha_2 \\ \\ -\beta_1 & \alpha_1 \end{bmatrix} \begin{bmatrix} x_0 \\ \\ y_0 \end{bmatrix} \\ &= \frac{\begin{bmatrix} \beta_2 x_0 - \alpha_2 y_0 \\ \\ -\beta_1 x_0 + \alpha_1 y_0 \end{bmatrix}}{(\alpha_1 \beta_2 - \alpha_2 \beta_1)}. \end{aligned} \tag{A.13}$$

When calculating the inverse matrix we used

$$\vec{A}^{-1} = \frac{1}{|\vec{A}|}\vec{A}^{*}, \tag{A.14}$$

where $\vec{A}^{*}$ is the adjugate matrix of $\vec{A}$.

Now we have the general solution. Given the specific matrix (2.26) and initial condition (2.27) of the simple TES model, we have:

$$\lambda_{1,2} = -\frac{1}{2}(\frac{1}{\tau_{el}} + \frac{1}{\tau_I}) \pm \frac{1}{2}\sqrt{(\frac{1}{\tau_{el}} - \frac{1}{\tau_I})^2 - 4\frac{R_0\mathcal{L}_I}{\tau L}(2+\beta_I)} \tag{A.15}$$

$$\vec{v_{1,2}} = \begin{bmatrix} \dfrac{(\lambda_{1,2} + 1/\tau_I)C}{I_0 R_0(2+\beta_I)} \\ \\ 1 \end{bmatrix}. \tag{A.16}$$

$$\begin{bmatrix} \mu_1 \\ \\ \mu_2 \end{bmatrix} = \begin{bmatrix} \dfrac{-\Delta T_0(\lambda_2 + 1/\tau_I)}{(\lambda_1 - \lambda_2)} \\ \dfrac{\Delta T_0(\lambda_1 + 1/\tau_I)}{(\lambda_1 - \lambda_2)} \end{bmatrix}. \tag{A.17}$$

Put into the solution's general form (A.2), the time response of the TES current and temperature are derived as:

$$\delta I = \frac{\Delta T_0 C(\tau_I\lambda_1 + 1)(\tau_I\lambda_2 + 1)}{\tau_I^2(\lambda_1 - \lambda_2)I_0R_0(2+\beta_I)}(e^{\lambda_2 t} - e^{\lambda_1 t}) \tag{A.18}$$

$$\delta T = \frac{\Delta T_0}{\tau_I(\lambda_1 - \lambda_2)}[(\tau_I\lambda_1 + 1)e^{\lambda_2 t} - (\tau_I\lambda_2 + 1)e^{\lambda_1 t}]. \tag{A.19}$$

A.2. 2-body model

A.2.1. General form

If we want to work with a more complex model (for example, a TES with a separate absorber), we only need to add a term to the differential equation set, and the matrix becomes a third order one. The solving procedure still follows the same three steps as introduced in the previous section.

Again, let's start with a general form of the matrix. Denoting

$$\vec{A} = \begin{bmatrix} a & b & c \\ d & e & f \\ g & h & i \end{bmatrix}, \tag{A.20}$$

we have

$$\begin{aligned} |\vec{A} - \vec{\Lambda}| = &- \lambda^3 + (a + e + i)\lambda^2 + (hf + bd + cg - ae - ai - ei)\lambda \\ &+ (aei + bgf + cdh - ahf - bdi - ceg). \end{aligned} \tag{A.21}$$

The root of this third order equation has a more complex form than the second order one. Let's first write the equation in a simpler form:

$$\lambda^3 + k_2\lambda^2 + k_1\lambda + k_0 = 0. \tag{A.22}$$

Note that we have removed the negtive sign in front of λ_3. The three roots can be solved as

$$\lambda_1 = -\frac{k_2}{3} + \sqrt[3]{\frac{k_2k_1}{6} - \frac{k_2^3}{27} - \frac{k_0}{2} + \sqrt{(\frac{k_2k_1}{6} - \frac{k_2^3}{27} - \frac{k_0}{2})^2 + (\frac{k_1}{3} - \frac{k_2^2}{9})^3}} + \sqrt[3]{\frac{k_2k_1}{6} - \frac{k_2^3}{27} - \frac{k_0}{2} - \sqrt{(\frac{k_2k_1}{6} - \frac{k_2^3}{27} - \frac{k_0}{2})^2 + (\frac{k_1}{3} - \frac{k_2^2}{9})^3}}$$

$$\lambda_2 = -\frac{k_2}{3} + \frac{-1+\sqrt{3}i}{2}\sqrt[3]{\frac{k_2k_1}{6} - \frac{k_2^3}{27} - \frac{k_0}{2} + \sqrt{(\frac{k_2k_1}{6} - \frac{k_2^3}{27} - \frac{k_0}{2})^2 + (\frac{k_1}{3} - \frac{k_2^2}{9})^3}} + \frac{-1-\sqrt{3}i}{2}\sqrt[3]{\frac{k_2k_1}{6} - \frac{k_2^3}{27} - \frac{k_0}{2} - \sqrt{(\frac{k_2k_1}{6} - \frac{k_2^3}{27} - \frac{k_0}{2})^2 + (\frac{k_1}{3} - \frac{k_2^2}{9})^3}}$$

$$\lambda_3 = -\frac{k_2}{3} + \frac{-1-\sqrt{3}i}{2}\sqrt[3]{\frac{k_2k_1}{6} - \frac{k_2^3}{27} - \frac{k_0}{2} + \sqrt{(\frac{k_2k_1}{6} - \frac{k_2^3}{27} - \frac{k_0}{2})^2 + (\frac{k_1}{3} - \frac{k_2^2}{9})^3}} + \frac{-1+\sqrt{3}i}{2}\sqrt[3]{\frac{k_2k_1}{6} - \frac{k_2^3}{27} - \frac{k_0}{2} - \sqrt{(\frac{k_2k_1}{6} - \frac{k_2^3}{27} - \frac{k_0}{2})^2 + (\frac{k_1}{3} - \frac{k_2^2}{9})^3}} \tag{A.23}$$

To make it look simplier, denote:

$$\Delta = (\frac{k_2k_1}{6} - \frac{k_2^3}{27} - \frac{k_0}{2})^2 + (\frac{k_1}{3} - \frac{k_2^2}{9})^3$$

$$= r^2 + q^3, \tag{A.24}$$

so

$$\lambda_1 = -\frac{k_2}{3} + \sqrt[3]{r+\sqrt{\Delta}} + \sqrt[3]{r-\sqrt{\Delta}} \tag{A.25}$$

$$\lambda_2 = -\frac{k_2}{3} + \frac{-1+\sqrt{3}i}{2}\sqrt[3]{r+\sqrt{\Delta}} + \frac{-1-\sqrt{3}i}{2}\sqrt[3]{r-\sqrt{\Delta}} \tag{A.26}$$

$$\lambda_3 = -\frac{k_2}{3} + \frac{-1-\sqrt{3}i}{2}\sqrt[3]{r+\sqrt{\Delta}} + \frac{-1+\sqrt{3}i}{2}\sqrt[3]{r-\sqrt{\Delta}} \tag{A.27}$$

The eigenvector

$$\vec{v} = \begin{bmatrix} \alpha \\ \beta \\ \gamma \end{bmatrix} \tag{A.28}$$

santisfies

$$\begin{bmatrix} a-\lambda & b & c \\ d & e-\lambda & f \\ g & h & i-\lambda \end{bmatrix} \begin{bmatrix} \alpha \\ \beta \\ \gamma \end{bmatrix} = \vec{0} \tag{A.29}$$

$$\vec{v} = \begin{bmatrix} \alpha \\ \beta \\ \gamma \end{bmatrix} = \begin{bmatrix} c(\lambda-e)+bf \\ f(\lambda-a)+cd \\ (\lambda-a)(\lambda-e)-bd \end{bmatrix} = \begin{bmatrix} c(\lambda-e)+bf \\ f(\lambda-a)+cd \\ \dfrac{g\alpha+h\beta}{(\lambda-i)} \end{bmatrix}. \tag{A.30}$$

Now with the initial condition:

$$\vec{X}(0) = \begin{bmatrix} x_0 \\ y_0 \\ z_0 \end{bmatrix}, \tag{A.31}$$

we have

$$\begin{bmatrix} \alpha_1 & \alpha_2 & \alpha_3 \\ \beta_1 & \beta_2 & \beta_3 \\ \gamma_1 & \gamma_2 & \gamma_3 \end{bmatrix} \begin{bmatrix} \mu_1 \\ \mu_2 \\ \mu_3 \end{bmatrix} = \begin{bmatrix} x_0 \\ y_0 \\ z_0 \end{bmatrix}. \tag{A.32}$$

The three constants can be solved by

$$\begin{bmatrix} \mu_1 \\ \mu_2 \\ \mu_3 \end{bmatrix} = \begin{bmatrix} \alpha_1 & \alpha_2 & \alpha_3 \\ \beta_1 & \beta_2 & \beta_3 \\ \gamma_1 & \gamma_2 & \gamma_3 \end{bmatrix}^{-1} \begin{bmatrix} x_0 \\ y_0 \\ z_0 \end{bmatrix}$$

$$= \begin{vmatrix} \alpha_1 & \alpha_2 & \alpha_3 \\ \beta_1 & \beta_2 & \beta_3 \\ \gamma_1 & \gamma_2 & \gamma_3 \end{vmatrix}^{-1} \begin{bmatrix} (\beta_2\gamma_3 - \beta_3\gamma_2) & -(\alpha_2\gamma_3 - \alpha_3\gamma_2) & (\alpha_2\beta_3 - \alpha_3\beta_2) \\ -(\beta_1\gamma_3 - \beta_3\gamma_1) & (\alpha_1\gamma_3 - \alpha_3\gamma_1) & -(\alpha_1\beta_3 - \alpha_3\beta_1) \\ (\beta_1\gamma_2 - \beta_2\gamma_1) & -(\alpha_1\gamma_2 - \alpha_2\gamma_1) & (\alpha_1\beta_2 - \alpha_2\beta_1) \end{bmatrix} \begin{bmatrix} x_0 \\ y_0 \\ z_0 \end{bmatrix}$$

$$= \frac{\begin{bmatrix} (\beta_2\gamma_3 - \beta_3\gamma_2) & -(\alpha_2\gamma_3 - \alpha_3\gamma_2) & (\alpha_2\beta_3 - \alpha_3\beta_2) \\ -(\beta_1\gamma_3 - \beta_3\gamma_1) & (\alpha_1\gamma_3 - \alpha_3\gamma_1) & -(\alpha_1\beta_3 - \alpha_3\beta_1) \\ (\beta_1\gamma_2 - \beta_2\gamma_1) & -(\alpha_1\gamma_2 - \alpha_2\gamma_1) & (\alpha_1\beta_2 - \alpha_2\beta_1) \end{bmatrix} \begin{bmatrix} x_0 \\ y_0 \\ z_0 \end{bmatrix}}{\gamma_1(\alpha_2\beta_3 - \alpha_3\beta_2) - \gamma_2(\alpha_1\beta_3 - \alpha_3\beta_1) + \gamma_3(\alpha_1\beta_2 - \alpha_2\beta_1)}. \tag{A.33}$$

A.2.2. Sidecar model

A.2.2.1. Differential equations. The electrical circuit of a sidecar model (Figure A.1) is in the same form as Fig. 2.3, and the electrical differential equation is the same as

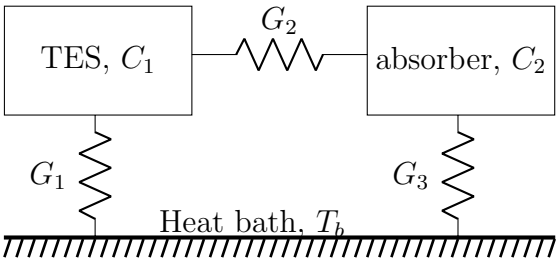

Figure A.1. The thermal circuit for sidecar model. G_1: thermal conductance between the TES and the heat bath; G_2: thermal conductance between the TES and the absorber; G_3: thermal conductance between the absorber and the heat bath; C_1: heat capacity of the TES; C_2: heat capacity of the absorber.

Eq. (2.12):

$$\frac{d\delta I}{dt} = -\frac{1}{\tau_{el}}\delta I - \frac{\mathcal{L}_I G}{I_0 L}\delta T_1 + \frac{1}{L}\delta V. \tag{A.34}$$

Here T_1 is the temperature of the TES, and

$$\mathcal{L}_I = \frac{P_{J_0}\alpha_I}{G_1 T_{1_0}}, \qquad \tau_{el} = \frac{L}{R_L + R_0(1+\beta_I)}. \tag{A.35}$$

The thermal feedback yields the equations for the TES and the absorber:

$$C_1\frac{dT_1}{dt} = P_J - P_{\text{tes-bath}} + P_{\text{abs-tes}}. \tag{A.36}$$

$$C_2\frac{dT_2}{dt} = P - P_{abs-bath} - P_{\text{abs-tes}}. \tag{A.37}$$

T_1, C_1 and T_2, C_2 are the temperature and heat capacity of the TES and absorber, respectively. $P_{\text{tes-bath}}$, $P_{\text{abs-tes}}$, and $P_{abs-bath}$ are the power of thermal flow from the TES

to the heat bath, from the absorber to the TES, and from the absorber to the heat bath, respectively. P is the power input onto the absorber.

Expanding the terms under small signal condition:

$$\delta T_1 \equiv T_1 - T_{1_0} \tag{A.38}$$

$$\delta T_2 \equiv T_2 - T_{2_0} \tag{A.39}$$

$$\begin{aligned} P_J &= I^2 R \\ &= (I_0 + \delta I)^2 (R_0 + \alpha_I \frac{R_0}{T_{1_0}} \delta T_1 + \beta_I \frac{R_0}{I_0} \delta I) \\ &= I_0 R_0 (2 + \beta_I)] \delta I + (\frac{\alpha I_0^2 R_0}{T_{1_0}}) \delta T_1 + \mathcal{O}(\delta T_1, \delta I), \end{aligned} \tag{A.40}$$

$$\begin{aligned} P_{\text{tes-bath}} &= K_1 (T_1^n - T_b^n) \\ &\approx P_{tes-bath_0} + \frac{dP_{\text{tes-bath}}}{dT_1} \delta T_1 \\ &= P_{tes-bath_0} + G_1 \delta T_1, \end{aligned} \tag{A.41}$$

$$\begin{aligned} P_{\text{abs-tes}} &= K_2 (T_2^n - T_1^n) \\ &\approx P_{\text{abs-tes}_0} + \frac{\partial P_{\text{abs-tes}}}{\partial T_2} \delta T_2 + \frac{\partial P_{\text{abs-tes}}}{\partial T_1} \delta T_1 \\ &= P_{\text{abs-tes}_0} + G_2^a \delta T_2 - G_2^t \delta T_1, \end{aligned} \tag{A.42}$$

$$
\begin{aligned}
P_{abs-bath} &= K_3(T_2^n - T_b^n) \\
&\approx P_{\mathrm{abs-bath}_0} + \frac{dP_{abs-bath}}{dT_2}\delta T_2 \\
&= P_{\mathrm{abs-bath}_0} + G_3\delta T_2, \qquad \text{(A.43)}
\end{aligned}
$$

$$
P = P_0 + \delta P, \qquad \text{(A.44)}
$$

we get

$$
\frac{d\delta T_1}{dt} = \frac{I_0 R_0}{C_1}(2+\beta_I)\delta I - [\frac{1}{\tau_I} + \frac{G_2^t}{C_1}]\delta T_1 + \frac{G_2^a}{C_1}\delta T_2, \qquad \text{(A.45)}
$$

$$
\frac{d\delta T_2}{dt} = \frac{G_2^t}{C_2}\delta T_1 - \frac{G_2^a + G_3}{C_2}\delta T_2 + \frac{1}{C_2}\delta P. \qquad \text{(A.46)}
$$

G_1 is the thermal conductance between the TES and the heat bath at the TES balance temperature T_{1_0}. G_2^t and G_2^a are the thermal conductance between the TES and the absorber at TES and absorber balance temperature T_{1_0} and T_{2_0}, respectively. G_3 is that between the absorber and the heat bath, at T_{2_0}.

Again, setting δV and δP to zero, the differential equation set becomes homogeneous, and can be solved using a matrix approach.

A.2.2.2. Solution. The matrix $\vec{A}$ of sidecar model has the same form as the mushroom model, except a few terms:

$$\vec{A} = \begin{bmatrix} -\frac{1}{\tau_{el}} & -\frac{\mathcal{L}_I G_1}{I_0 L} & 0 \\ \frac{I_0 R_0(2+\beta_I)}{C_1} & -[\frac{1}{\tau_I} + \frac{G_2^t}{C_1}] & \frac{G_2^a}{C_1} \\ 0 & \frac{G_2^t}{C_2} & -\frac{G_2^a + G_3}{C_2} \end{bmatrix}, \tag{A.47}$$

The initial condition is the same.

τ_1, τ_2, and τ_3, which are reciprocals of λ_1, λ_2, and λ_3, have the same form as in Ref. [**101**]. The analytic solution, which is the time response of the TES current, TES temperature, and absorber temperature, also have the same form, and are as follows:

$$\delta I(t) = -(\Delta T_0)\frac{\mathcal{L}_I G_1 G_2^a}{I_0 L C_1}(A_1 e^{t/\tau_1} + A_2 e^{t/\tau_2} + A_3 e^{t/\tau_3}), \tag{A.48}$$

$$\delta T_{tes}(t) = (\Delta T_0)\frac{G_2^a}{C_1}(A_{T_{tes}1} e^{t/\tau_1} + A_{T_{tes}2} e^{t/\tau_2} + A_{T_{tes}3} e^{t/\tau_3}), \tag{A.49}$$

$$\delta T_{abs}(t) = (\Delta T_0)\frac{G_2^a G_2^t}{C_1 C_2}(A_{T_{abs}1} e^{t/\tau_1} + A_{T_{abs}2} e^{t/\tau_2} + A_{T_{abs}3} e^{t/\tau_3}), \tag{A.50}$$

where

$$\begin{aligned} A_n &= (3\lambda_n^2 + 2k_2\lambda_n + k_1)^{-1} \\ A_{T_{tes}n} &= A_n(\lambda_n + 1/\tau_{el}) \\ A_{T_{abs}n} &= A_{T_{tes}n}(\lambda_n + (G_2^a + G_3)/C_2)^{-1} \end{aligned} \tag{A.51}$$

and

$$
\begin{aligned}
k_2 &= -(a+e+i) \\
&= \frac{1}{\tau_{el}} + \frac{1}{\tau_I} + \frac{G_2^t}{C_1} + \frac{G_2^a + G_3}{C_2}
\end{aligned}
$$

$$
\begin{aligned}
k_1 &= ae + ai + ei - (hf + bd + cg) \\
&= \frac{1}{\tau_{el}}(\frac{1}{\tau_I} + \frac{G_2^t}{C_1}) + \frac{G_2^a + G_3}{\tau_{el} C_2} + \frac{G_2^a + G_3}{C_2}(\frac{1}{\tau_I} + \frac{G_2^t}{C_1}) \\
&- \frac{G_2^t G_2^a}{C_1 C_2} + \frac{\mathcal{L}_I R_0}{\tau L}(2 + \beta_I) \\
&= \frac{G_2^t}{\tau_{el} C_1} + \frac{G_2^a + G_3}{\tau_{el} C_2} + \frac{G_2^a + G_3}{\tau_I C_2} + \frac{1}{\tau_{el}\tau_I} + \frac{\mathcal{L}_I R_0}{\tau L}(2 + \beta_I) + \frac{G_2^t G_3}{C_1 C_2}
\end{aligned}
$$

$$
\begin{aligned}
k_0 &= ahf + bdi + ceg - (aei + bgf + cdh) \\
&= -\frac{G_2^t G_2^a}{\tau_{el} C_1 C_2} + \frac{(G_2^a + G_3)\mathcal{L}_I R_0}{\tau L C_2}(2 + \beta_I) + \frac{G_2^a + G_3}{\tau_{el} C_2}(\frac{1}{\tau_I} + \frac{G_2^t}{C_1}) \\
&= \frac{G_2^a + G_3}{\tau_{el}\tau_I C_2} + \frac{(G_2^a + G_3)\mathcal{L}_I R_0}{\tau L C_2}(2 + \beta_I) + \frac{G_2^t G_3}{\tau_{el} C_1 C_2}.
\end{aligned} \tag{A.52}
$$

A.2.3. Mushroom model

Bennett *et al.* [**101**] gave the analytical solution for a 2-body TES with mushroom configuration (Figure A.2). We can try to deduce to his conclusion following the steps above. The differential matrix and initial condition are:

$$
\vec{A} = \begin{bmatrix} -\frac{1}{\tau_{el}} & -\frac{\mathcal{L}_I G_1}{I_0 L} & 0 \\ \frac{I_0 R_0 (2+\beta_I)}{C_1} & -(\frac{1}{\tau_I} + \frac{G_2}{C_1}) & \frac{G_2}{C_1} \\ 0 & \frac{G_2}{C_2} & -\frac{G_2}{C_2} \end{bmatrix}, \qquad \vec{X}(0) = \begin{bmatrix} 0 \\ 0 \\ \frac{E}{C_2} \end{bmatrix}. \tag{A.53}
$$

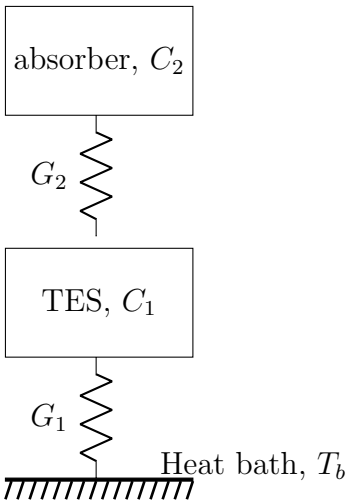

Figure A.2. The thermal circuit for mushroom model. G_1: thermal conductance between the TES and the heat bath; G_2: thermal conductance between the TES and the absorber; C_1: heat capacity of the TES; C_2: heat capacity of the absorber.

Here C_1 is the heat capacity of the TES, G_1 is the thermal conductance between the TES and the heat bath, C_2 is the heat capacity of the absorber, and G_2 is the thermal conductance between the TES and the absorber.

In matrix $\vec{A}$, c and g are zero. We have the eigenvector

$$\vec{v} = \begin{bmatrix} \alpha \\ \beta \\ \gamma \end{bmatrix} = \begin{bmatrix} bf \\ f(\lambda - a) \\ (\lambda - a)(\lambda - e) - bd \end{bmatrix} = \begin{bmatrix} bf \\ f(\lambda - a) \\ fh\dfrac{(\lambda - a)}{(\lambda - i)} \end{bmatrix}. \tag{A.54}$$

For the initial values, x_0 and y_0 are 0. We have the constants

$$\begin{bmatrix}\mu_1\\ \mu_2\\ \mu_3\end{bmatrix} = \frac{z_0 \begin{bmatrix}(\alpha_2\beta_3 - \alpha_3\beta_2)\\ -(\alpha_1\beta_3 - \alpha_3\beta_1)\\ (\alpha_1\beta_2 - \alpha_2\beta_1)\end{bmatrix}}{\gamma_1(\alpha_2\beta_3 - \alpha_3\beta_2) - \gamma_2(\alpha_1\beta_3 - \alpha_3\beta_1) + \gamma_3(\alpha_1\beta_2 - \alpha_2\beta_1)}$$

$$= \frac{-z_0}{(\lambda_3 - \lambda_2)(\lambda_1 - \lambda_3)(\lambda_2 - \lambda_1)} \begin{bmatrix}(\lambda_3 - \lambda_2)\\ (\lambda_1 - \lambda_3)\\ (\lambda_2 - \lambda_1)\end{bmatrix}$$

$$= z_0 \begin{bmatrix}(3\lambda_1^2 + 2k_2\lambda_1 + k_1)^{-1}\\ (3\lambda_2^2 + 2k_2\lambda_2 + k_1)^{-1}\\ (3\lambda_3^2 + 2k_2\lambda_3 + k_1)^{-1}\end{bmatrix}, \tag{A.55}$$

or in brief

$$\mu_n = z_0(3\lambda_n^2 + 2k_2\lambda_n + k_1)^{-1} \tag{A.56}$$

And then

$$\begin{aligned}
\mu_n\alpha &= z_0 bf(3\lambda_n^2 + 2k_2\lambda_n + k_1)^{-1}, \\
\mu_n\beta &= \mu_n\alpha\frac{(\lambda - a)}{b}, \\
\mu_n\gamma &= \mu_n\beta h(\lambda - i)^{-1}.
\end{aligned} \tag{A.57}$$

It is not hard to match this result with Bennett's conclusion. The detailed form of the eigenvalues are also not hard to derive.